NUREG/CR-4521
SAND86-0318
R5, R7
Printed June 1986

TURC2 and 3: Large Scale $UO_2/ZrO_2/Zr$ Melt-Concrete Interaction Experiments and Analysis

J. E. Gronager, A. J. Suo-Anttila, J. E. Brockmann

Prepared by
Sandia National Laboratories
Albuquerque, New Mexico 87185 and Livermore, California 94550
for the United States Department of Energy
under Contract DE-AC04-76DP00789

Prepared for
U. S. NUCLEAR REGULATORY COMMISSION

Available from

Superintendent of Documents
U.S. Government Printing Office
Post Office Box 37082
Washington, D.C. 20013-7982

and

National Technical Information Service
Springfield, VA 22161

NUREG/CR-4521
SAND86-0318
R5, R7

TURC2 AND 3: LARGE SCALE $UO_2/ZrO_2/Zr$ MELT-CONCRETE INTERACTION EXPERIMENTS AND ANALYSIS

J. E. Gronager
A. J. Suo-Anttila*
J. E. Brockmann

June 1986

Sandia National Laboratories
Albuquerque, NM 87185
Operated by
Sandia Corporation
for the
U.S. Department of Energy

Prepared for
Containment Systems Research Branch
Division of Accident Evaluation
Office of Nuclear Regulatory Research
U.S. Nuclear Regulatory Commission
Washington, DC 20555
Under Memorandum of Understanding DOE 40-550-75
NRC FIN No. A1218

*Science Applications International Corporation
Albuquerque, New Mexico 87102

ABSTRACT

Two large scale $UO_2/ZrO_2/Zr$ debris-concrete experiments TURC2 and TURC3 are reported here. The experiments consisted of pouring a large quantity of molten $UO_2/ZrO_2/Zr$ mixtures onto limestone-common sand concrete. The molten material was allowed to cool naturally--no internal heating was present. Data for concrete ablation, gas evolution including composition and flow rate, and aerosol generation are presented.

The experimental results indicate very rapid crusting with no detectable concrete ablation. Gas reduction of H_2O and CO_2 to H_2 and CO was found to occur even with a purely oxidic (UO_2/ZrO_2) melt. Aerosol concentrations varied from 62 g/m^3 to less than 1 g/m^3 in the experiments.

A thermal analysis of the experiments was performed. The analysis is consistent with the result that rapid crusting with minimal concrete ablation occurs in both experiments.

CONTENTS

CONTENTS (continued)

List of Figures

List of Figures (continued)

List of Figures (continued)

List of Figures (continued)

List of Figures (continued)

LIST OF TABLES

List of Tables (continued)

1. INTRODUCTION

The interaction of molten fuel, cladding, and core structures with a concrete basemat has been recognized since the Reactor Safety Study, WASH-1400, as important aspects of severe reactor accidents.[1] An assessment of the physical source term resulting from these interactions is desirable if a comprehensive evaluation of the risks posed to reactor containments and engineered safety systems are to be made. Consequently, if the pressure load applied by the molten core debris-concrete interactions (possibly coupled with other physical events) should fail containment, a source of radioactive release to the environment would be realized. Over the past several years, an intensive study of these core debris-concrete interactions has been sponsored at Sandia National Laboratories by the Severe Accident Assessment Branch of the NRC's Office of Nuclear Regulatory Research.[2,3,4,5]

A brief review of past experimental investigations[2,3,4,5,6,7,8] of molten debris-concrete interactions shows two major categories:

(1) those experiments[6,7,8] conducted with simulant material such as dry ice, plexiglass, water and,

(2) experiments[2,3,4,5,9] conducted principally with high-temperature <u>metallic</u> materials and concrete.

The advantage of the first group of experiments is the possibility of observing the interaction zone between the simulant concrete and molten debris. However, the fundamental physical processes of high-temperature heat transfer with an ill-defined ablating material, such as concrete, cannot be simulated because it is not possible to match the relevant thermophysical properties and the interactions they produce. On the other hand, experiments within the second category provides actual data of the physical mechanisms of heat transfer and the physical source terms, such as combustible gas generation, aerosol generation rates, and fission-product release from the molten debris.

Past high temperature experiments were used to investigate the effects of molten-debris concrete interactions. The principal thrust of the experiments was the quantification of the physical processes which may impact containment integrity. These initial experiments provided investigators with an understanding of the principal phenomena and led to the development of two important severe accident analysis codes:

(1) The CORCON[10,11] model of core debris-concrete interaction and

(2) the VANESA[12] model of radionuclide release and aerosol generation.

At the present stage of our investigations for core debris-concrete interactions, primarily steel melts and their global behavior had been studied. Since the expected core debris composition ejected from the reactor vessel will certainly contain UO_2, ZrO_2, and Zr metal (as well as steel), it is imperative to investigate the interaction of these prototypic materials with concrete.

The Transient Urania-Concrete Test (TURC) program had been initiated to provide a preliminary observations of large scale $UO_2/ZrO_2/Zr$ melt-concrete interactions. The TURC test matrix, shown in Table 1.1, consisted of four experiments: two metallic melt-concrete tests (TURC1T and TURC1SS), a molten UO_2/ZrO_2-concrete test (TURC2) and a $UO_2/ZrO_2/Zr$-concrete test (TURC3).

The results of the TURC1T and TURC1SS experiments were reported in reference #9. In this report the results of the last two experiments, TURC2 and TURC3 will be presented. Due to similarity of all the TURC experiments extensive reference to the TURC1 series of experiments is made.

Table 1.1

TURC Test Matrix

Experiment	Molten Debris	Debris Temperature °K	Debris Mass Kg	Concrete
TURC1T	$Fe-Al_2O_3$	~2700	200	LCS*
TURC1SS	S.S.304	2350	200	LCS
TURC2	UO_2/ZrO_2	2660	200	LCS
TURC3	$UO_2/ZrO_2/Zr$	2575	200	LCS

*Limestone-Common Sand

2. EXPERIMENT DESCRIPTION

2.1 Overview of Experimental Facilities

The experimental facility for conducting TURC2 and TURC3 is shown schematically in Figures 2.1 and 2.2. The facility consists of two major components: (1) the melt generator, in which the melts were produced; and (2) the interaction chamber where the molten debris-concrete interaction occurs.

The melt generators for the experiments differ significantly from the TURC1 experiments due to the different method of producing the molten debris. In TURC2 and 3 an induction ring embedded suspector technique (IRIS) was employed in the Sandia Large Melt Facility to generate 200 kg quantities of molten debris. The IRIS technique employs the method demonstrated by Copus[13] for melting oxide materials. The technique consists of inductively heating embedded refractory metal rings within a matrix of the core debris material (see Table 2.1). The rings, in turn, heat and melt the debris material. Once the matrix begins to melt, a pool forms and continues to grow until it reaches the cooler outer boundary, thus freezing and forming a crust. This self-sculling provides adequate protection of the outer structural alumina crucible.

Once the melt has been produced, the molten debris is teemed down into the experiment crucible, located within a 13 m^3 interaction chamber.

After the teeming process is completed, the top orifice of the crucible is sealed with a sliding portcullis. Reaction products generated during the interaction are vented through an exit port and piped out of the interaction chamber, into a gravel filter.

The crucible utilized in these experiments is the same design as those which were used in the TURC1 experiments.[9] The crucible consists of an instrumented concrete slug cast at the base of a MgO annulus. The crucible design permits only axial ablation of the concrete slug.

The instrumentation of the experiment consisted of embedded thermocouples within the interaction crucible, discrete sampling of evolved gases, and aerosol instrumentation.

In order to evaluate the transport of fission products during melt-concrete interaction, various chemical species, listed in Table 2.2, were added to the melts, either in the furnace or the crucible, and samples of aerosols evolving from the melt pool were taken. The instrumentation utilized during the experiments is described in further detail in Section 2.4.

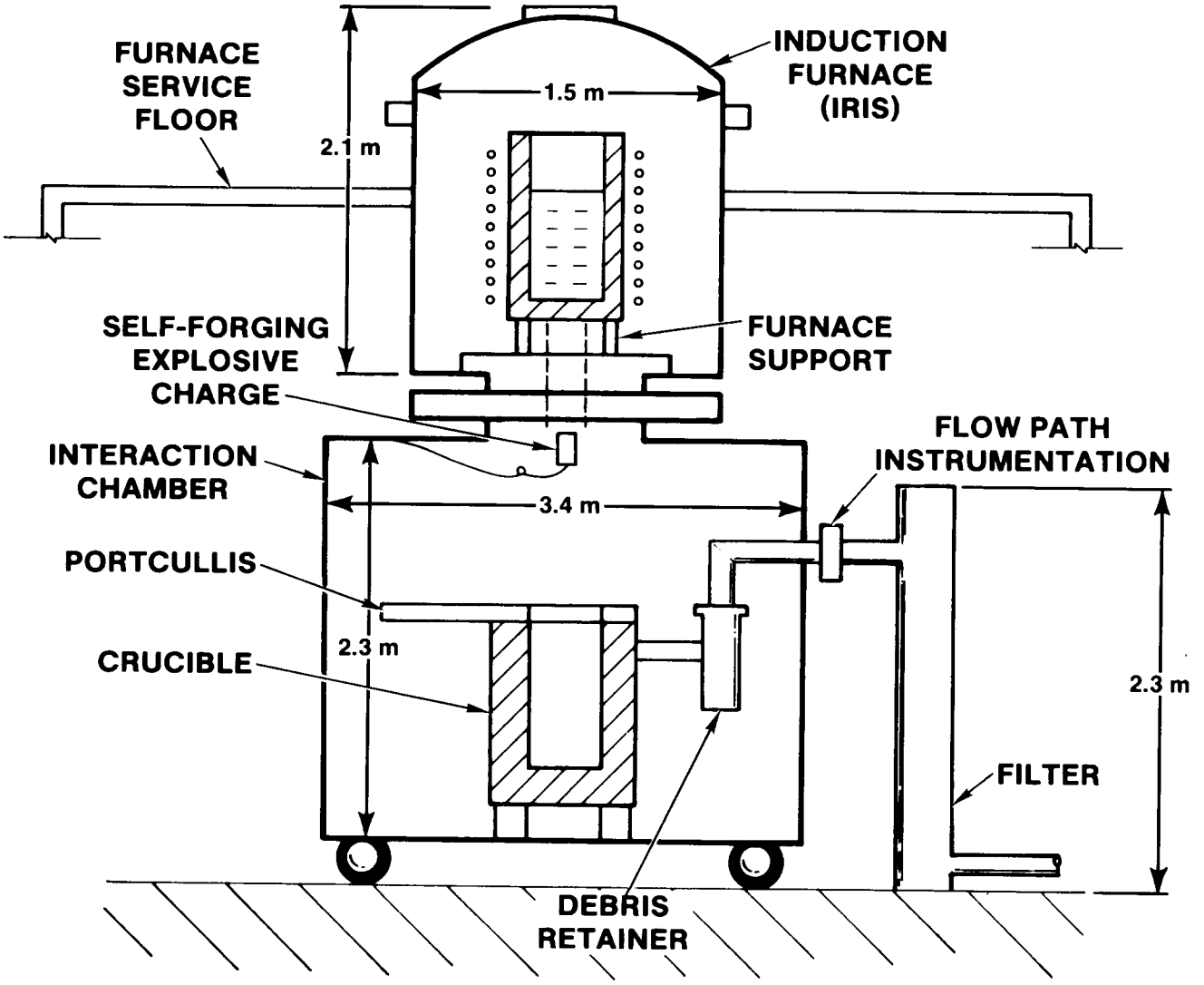

Figure 2.1. TURC2 and 3 Experimental Facility

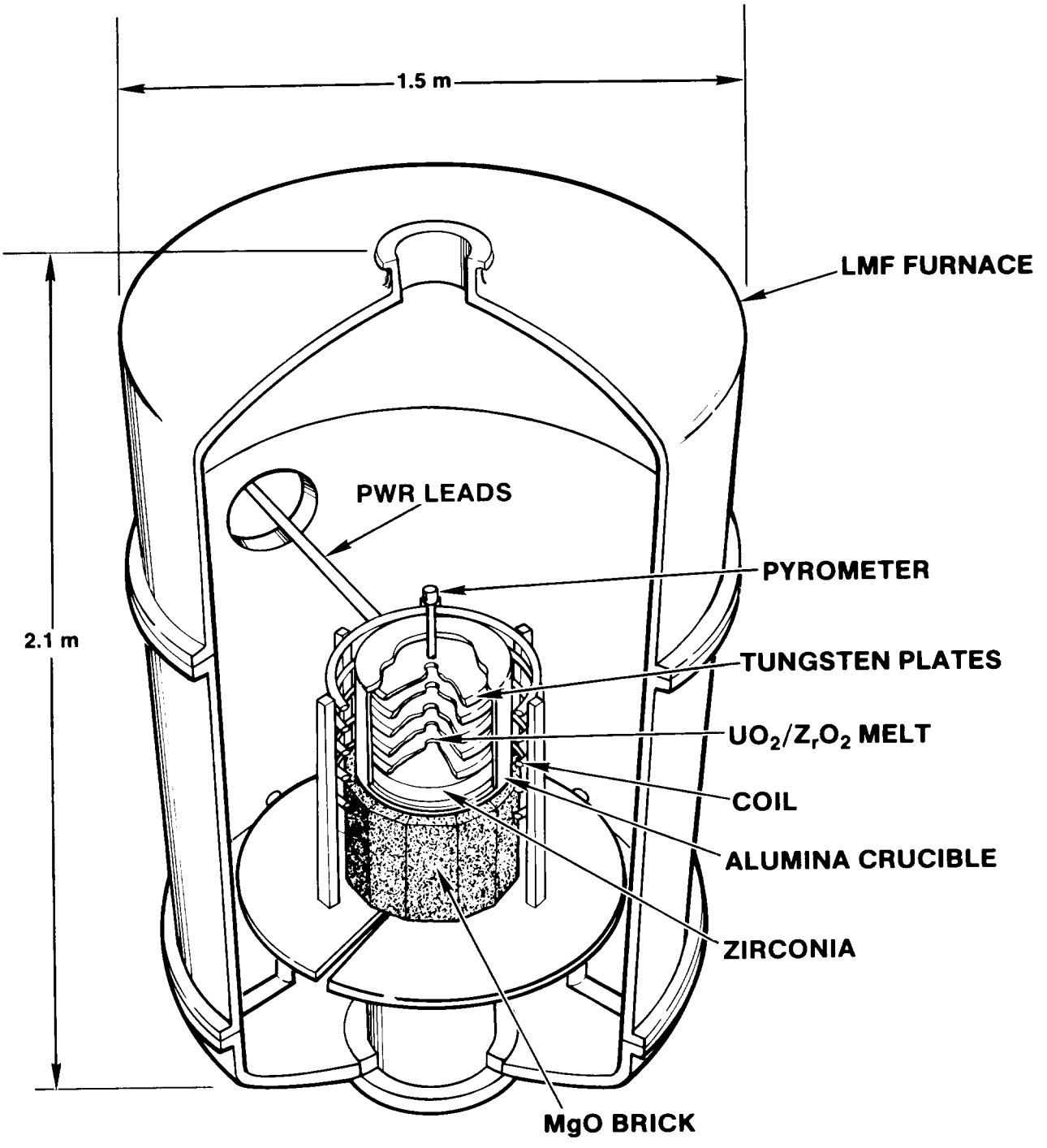

Figure 2.2. IRIS Melt Generator

Table 2.1

Bulk TURC2 and TURC3 Initial Debris Composition

Material	TURC2* weight %	Mass, Kg	TURC3* weight %	Mass, Kg
UO_2	70	140.0*	63.7	123.4
ZrO_2	30	60.0	27.3	54.6
Zr	0	0.0	9.0	18

*Plus fission product mock listed in Table 2.2.

Table 2.2

TURC2 and TURC3 Fission-Product Mocks

Fission Product	Quantity	Category
Te	1 kg*	Choleogens
Mn	1 kg**	Early Transition Elements
Mo	1 kg**	Early Transition Elements
CsI	1 kg*	Halogens
BaO	1 kg**	Alkaline Earths
ZrO_2	1 kg**	Tetravalents
CeO_2	1 kg**	Tetravalents
La_2O_3	1 kg**	Trivalents
Ni	1 kg**	Platiniods

*Loaded into experimental crucible
**Loaded into melt generator

2.2 Experiment Molten Debris

2.2.1 IRIS Melt Generator

The TURC2 and TURC3 molten debris was produced by melting about 200 kg of experiment debris material (see Table 2.1) in the IRIS melt generator shown in Figure 2.2.

The melt generator is housed within the Large Melt Facility (LMF) induction furnace. The induction furnace is approximately 1.5 meters in diameter and 2.1 meters tall. During furnace operation the internal atmosphere is continuously purged with argon at a normal rate of 14.1 m^3/hr at a furnace pressure of 0.114 MPa. The melt generator consists of several major components: the structural alumina crucible, tungsten rings, induction coil, instrumentation and experiment debris material.

The alumina crucible was 0.66 m high with an internal depth of 0.64 m. The crucible inside and outside diameters were 40 cm and 46 cm respectively.

Five tungsten rings were utilized to heat the experiment debris material by coupling to the induction field produced by the induction coil. The rings, shown in Figure 2.3, had outside diameters of 35.5 cm and inside diameters of 5 cm. Each ring was 3 mm thick. Five 2.5 cm holes were placed about the ring to permit relocation of molten debris during heating and teaming. Additionally, five, 7.5 mm holes were located near the outer diameter to provide for ring support rods during assembly.

The induction coil for the nominal 1 kHz, 280 kW power supply had two electrical sections with six turns in each section. The coil was 0.56 m in length and 0.53 m in diameter. All coil surfaces had a flexible insulating coating applied by the manufacturer (Inductotherm Corp.) to minimize arcing between coil turns.

The melt generator instrumentation consisted of Type 'K' thermocouples mounted on the outside of the alumina crucible and a pyrometer (in conjunction with a thermal well) to monitor the bulk temperature of the heated debris. The external crucible thermocouples were placed at approximately 10 cm intervals along the axial length of the crucible, in each of the four azimuthal quadrants. Thermocouples were also placed at various radial locations on the base of the crucible. The external thermocouples were used to monitor the outside wall temperature in order to assess the integrity of the crucible.

The debris temperature was measured by means of a pyrometer focused down a tungsten tube thermal wall, which was positioned along the radial centerline of the assembled melt generator (see Figure 2.4). The range of the pyrometer was from 1800 K to 3300 K.

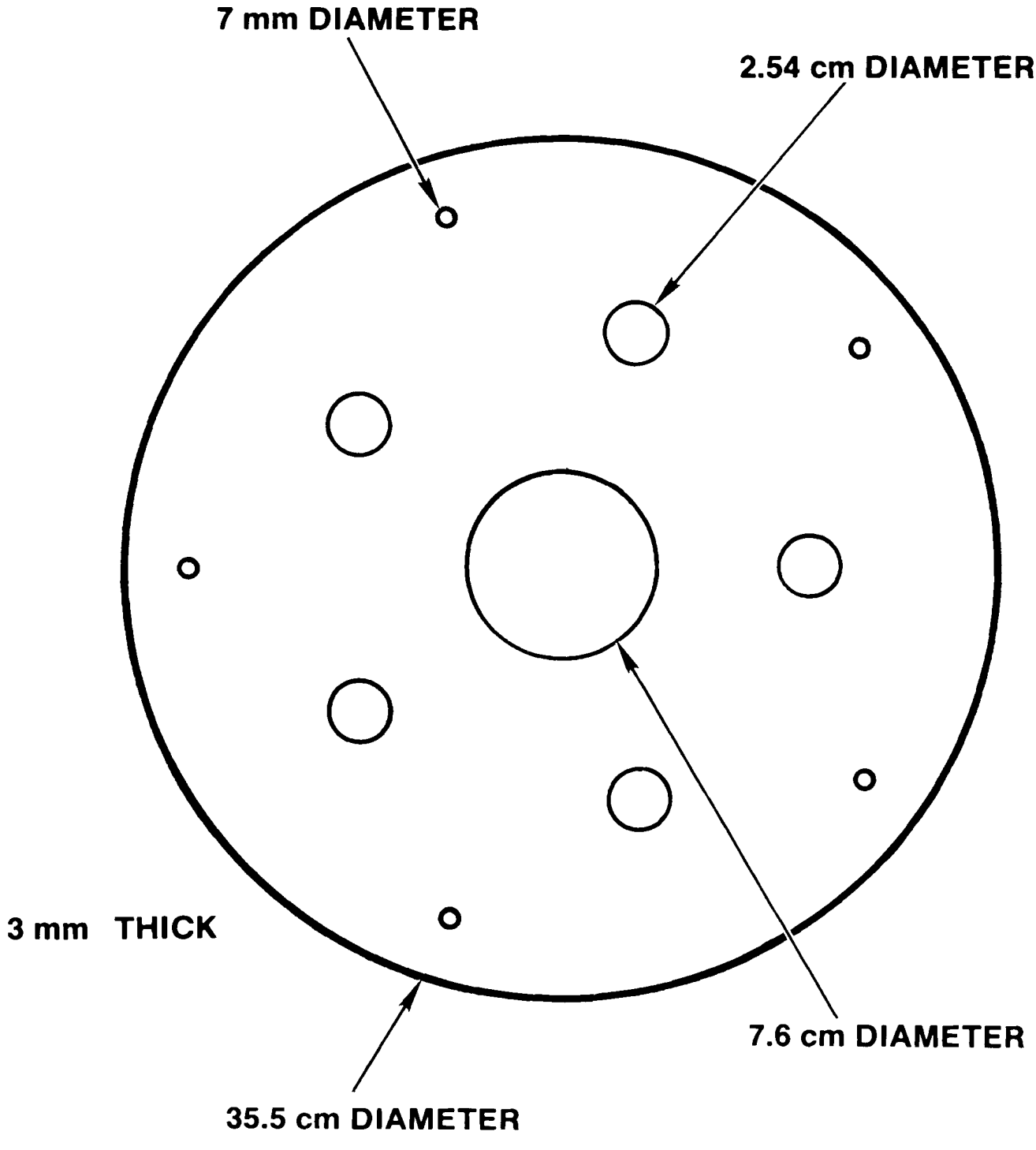

Figure 2.3. Tungsten Ring

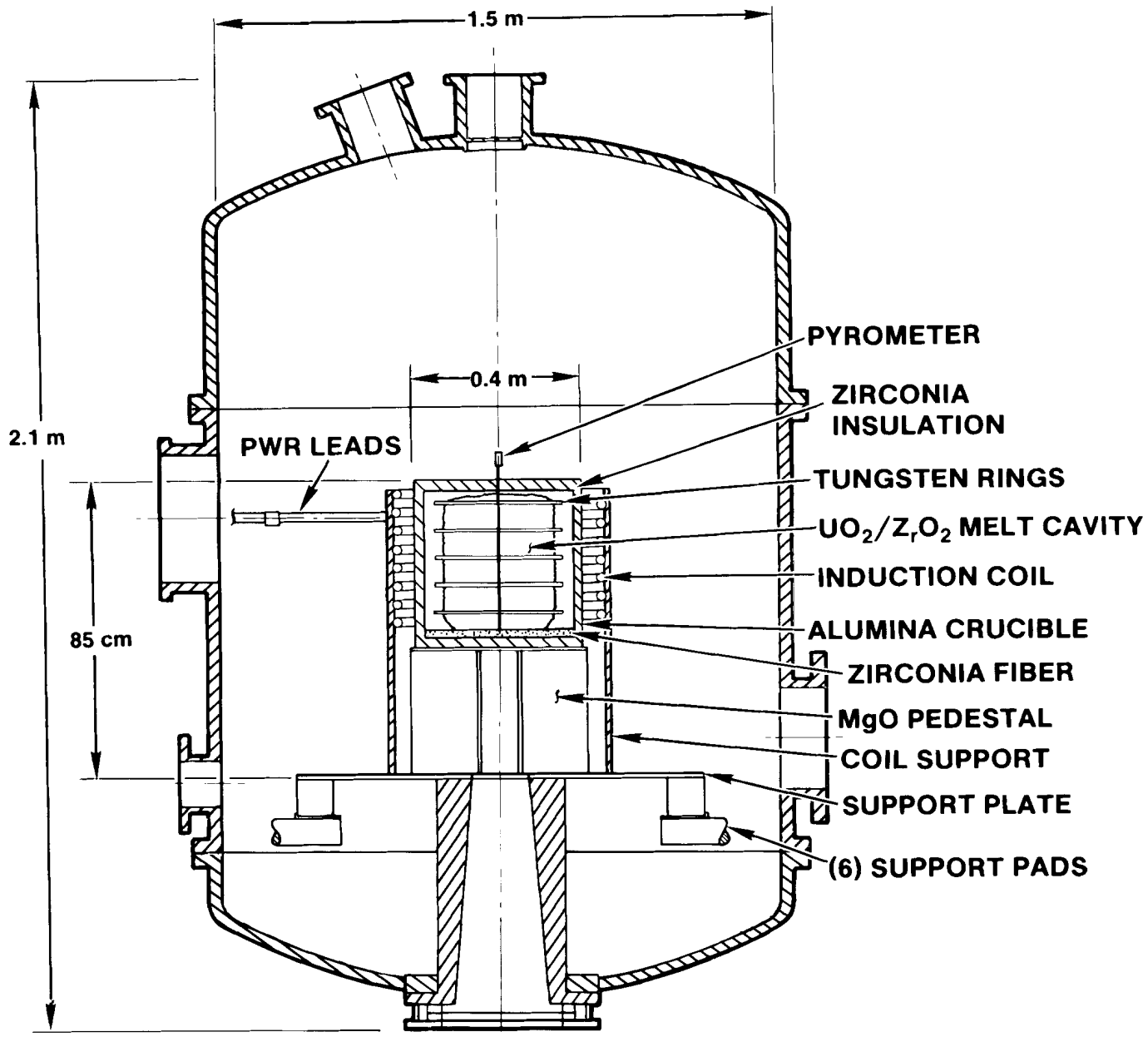

Figure 2.4. Schematic Representation of the Melt Generator Crucible Assembly

As shown schematically in Figure 2.4, assembly of the melt generator was initiated by installing a 2.5 cm thick plate of ZrO_2 insulating board in the base of the alumina crucible. This was followed by alternating layers of debris material and tungsten plates. The top surface of the debris was then covered with additional ZrO_2 boards.

The crucible was mounted on a MgO pedestal and the induction coil was installed. The spacing between the coil and the crucible was filled with dry magnesium oxide powder.

Melting of the debris material is accomplished by applying power to the induction coil which heats the tungsten plates. The tungsten plates in turn heats and melts the debris material. Typically a power of 100 kW for 2.5 to 3.0 hours is sufficient to melt the majority of the 200 Kg charge.

The teeming of the melt from the crucible is accomplished by firing an explosive self-forging projectile into the base of the alumina crucible. The explosive is mounted on a support tube just below the transfer section between the furnace chamber and the interaction chamber (see Figure 2.1). The explosive charge is remotely armed and fired. The explosive is approximately 3.8 cm in diameter and 7.5 cm in length. Alignment of the explosive is aided by a neon laser placed between two "sights" mounted on the explosive.

The explosive projectile impacts the alumina crucible forming a uniform 7.0-cm diameter hole. The melt then teems out under its own head and the 0.02 MPa overpressure of the furnace. Teeming is complete in approximately 3 seconds.

2.2.2 Experiment Debris Material

The composition of the debris material utilized in the TURC2 and 3 experiments is listed in Table 2.1. The principle difference between the two compositions is the inclusion of 9 w/o Zr metal in the TURC3 material. The debris material in both experiments contain various additional chemical species to aid in assessing the transport of fission products during melt-concrete interactions. The chemical species, listed in Table 2.2, commonly referred to as fission product mocks, were used to obtain data on aerosol release fractions for both volatile and refractory species during debris-concrete interactions. The fission product mocks which were used in the experiments are listed in Table 2.2.

The melting temperature of the debris material was determined by the cone slumping method. The TURC2 debris melted at 2660 K ± 10 K. The melting point of the TURC3 debris was 2573 K ± 25 K.

The UO_2 laden debris was fabricated by thoroughly mixing, in proper proportions, fine powders (1-10 μm) of the major debris constituents of UO_2, ZrO_2, and Zr. Once a uniform mixture was obtained, the mixed powder was isostatically pressed to form a large cylinder 20 cm in diameter by 10 to 15 cm in height. Due to furnace thermal and operational considerations, the cylinders were mechanically fractured into course gravel 0.5 to 2.0 cm in diameter.

2.3 Experiment Interaction Crucible

2.3.1 Interaction Crucible Description and Fabrication

The crucibles used in the TURC series of tests were of a new design and purpose. A crucible, shown schematically in Figure 2.5, consisted of an instrumented concrete slug 41 cm in diameter and 30 cm in height, cast at the base of a MgO annulus, 70 cm outside diameter and 1.2 meters in height.

The purpose of the crucible design is to force only axial or one-dimensional ablation of the concrete slug. By eliminating a concrete ablative sidewall, reaction products generated at the core debris-concrete interaction can be quantified, without the influence of reaction products generated at different thermo-physical conditions found at the sidewalls. These so-called 1-D crucibles were constructed to Sandia specifications by the New Mexico Civil Engineering Research Laboratory operated by the University of New Mexico.

The 1-D crucible is fabricated in two major steps: first, the construction of the MgO annulus, and second, casting of the concrete slug.

The MgO annulus was constructed using SONOTUBE* forms. The forms are right circular cylinders manufactured from paper. The MgO annulus, shown in Figure 2.6, was fabricated by arranging two sonotube forms in a concentric array in which a plywood base was installed. This was followed by the installation of the 7.5-cm diameter exhaust tube and the thermocouple arrays.

Each of the thermocouple arrays, shown in Figures 2.7 and 2.8, consisted of a 5-cm-diameter cylinder of the MgO castable material, in which four holes were drilled at 1-cm intervals. K-type, 1.5 mm diameter, thermocouples were installed in this fixture. The fixture was then installed at predetermined locations (see Table 2.7) within the annulus form. In the region where the concrete slug would be cast, a wire wrap, 1.5-mm diameter, with a 2-cm pitch, was installed in order to improve the bonding between the concrete slug and the MgO annulus.

---

*SONOTUBE forms trademark of the SONOCO Products.

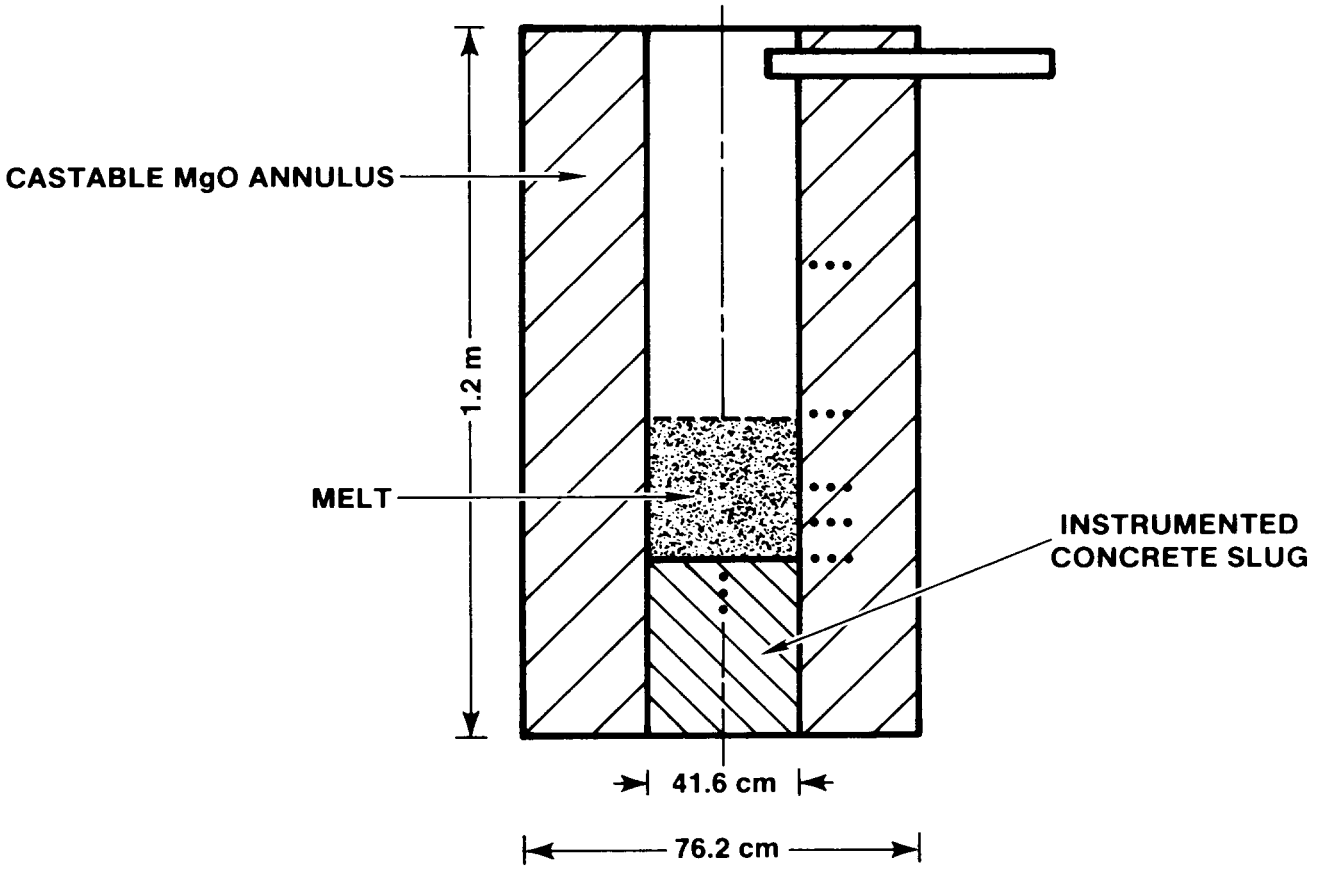

Figure 2.5. Schematic Drawing of the TURC Series Interaction Crucible

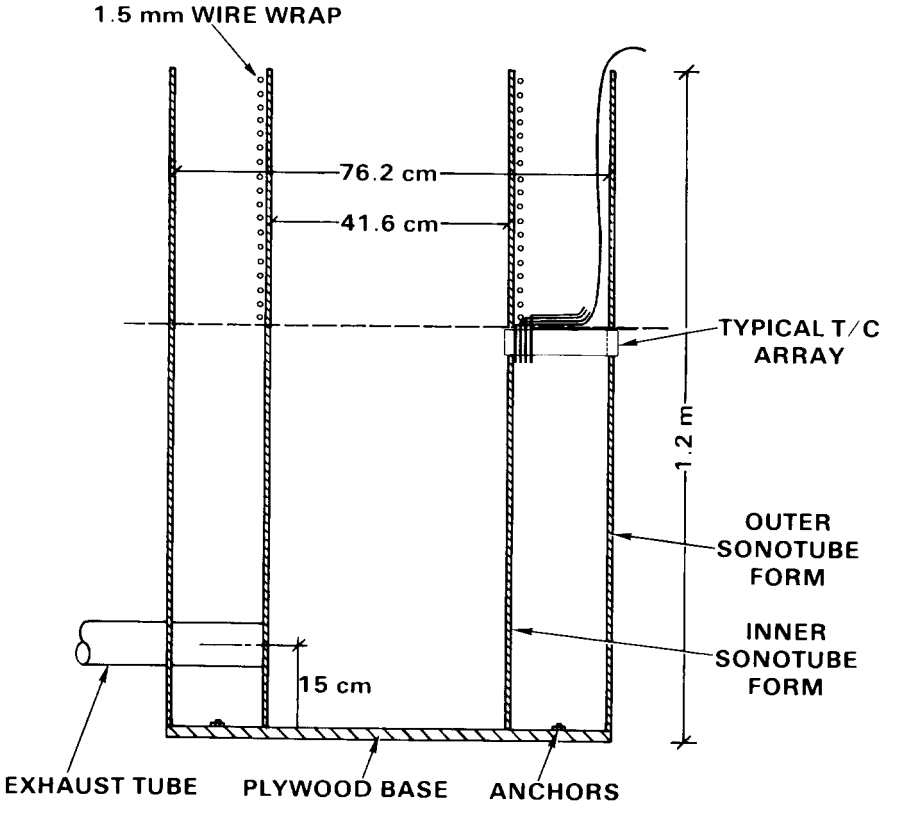

Figure 2.6. Fabrication Details of MgO Annulus

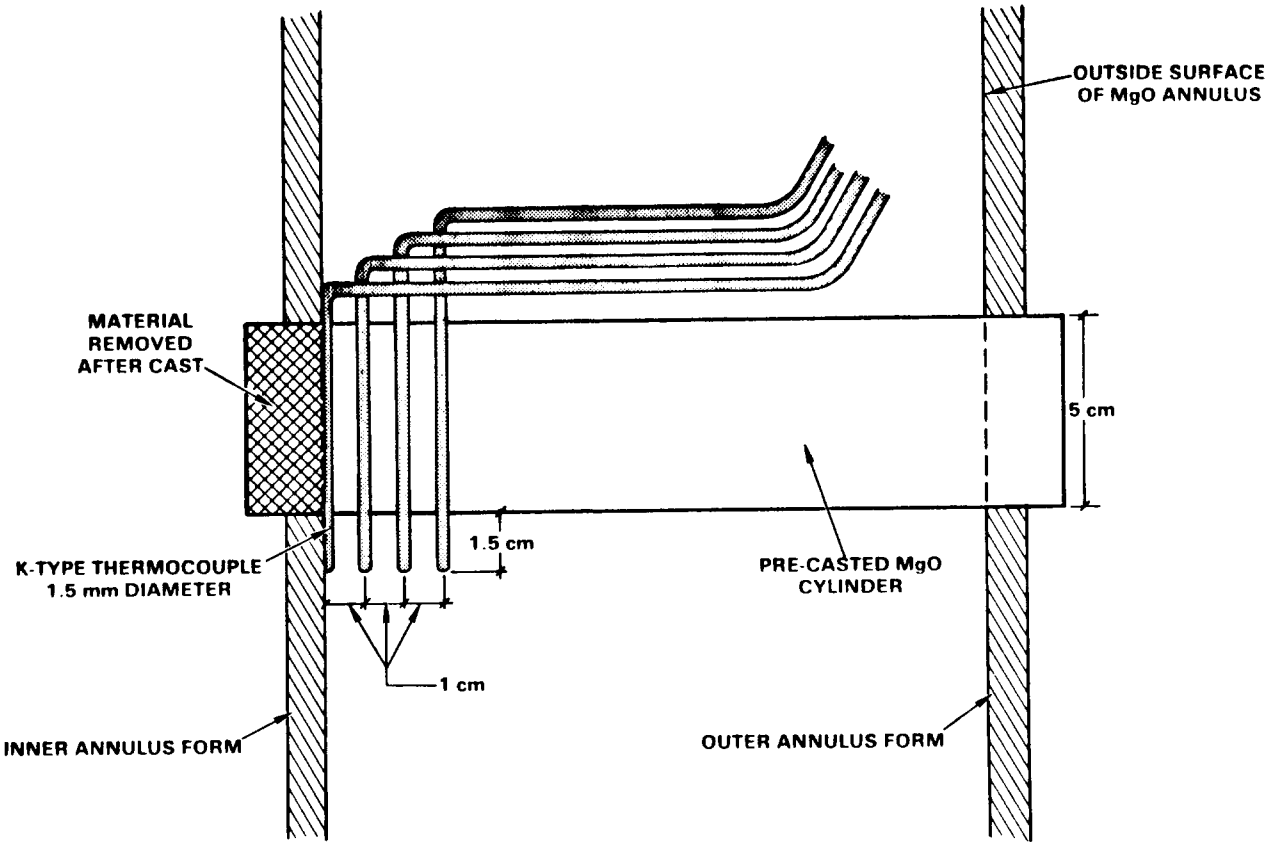

Figure 2.7. MgO Annulus Thermocouple Arrays

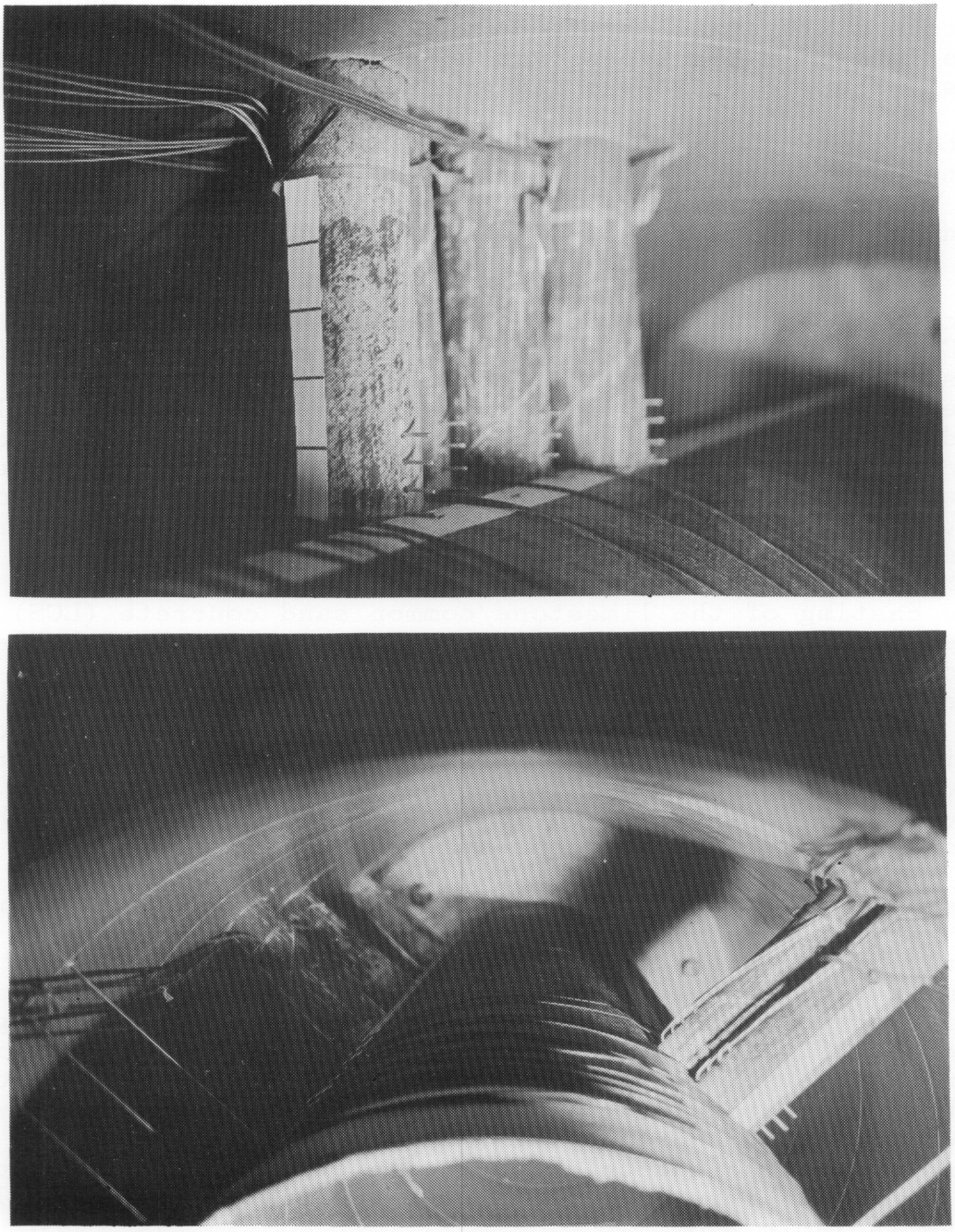

Figure 2.8. MgO Annulus Thermocouple Arrays Installed in Form

Once the form was prepared, the MgO castable, described in reference 9, was mixed in a clean paddle-type mixer. Once a homogeneous mixture was obtained, the material was hand-loaded into the forms. A high-speed vibrator was utilized to densify the mass. The procedure was repeated until the form was full.

After casting, the annulus was cured at ambient air temperature for three days. Further curing was accomplished by placing a heating element within the central cavity and maintaining a temperature of 473 K for 24 hours, followed by a cooling period of 24 hours.

Once the annulus was cooled to room temperature, the inner SONOTUBE form and wire wrap were removed, and a plywood platform was constructed 30 cm from the base of the MgO annulus (this is the same region where the wire wrap was installed). Carefully prepared thermocouple arrays, shown in Figure 2.9, held rigidly in place by a framework of 0.5 mm stainless steel wires, were installed on the platform and structural support was provided from outside the annulus. Location of these thermocouples are shown in Tables 2.7, 2.8, and 2.9.

The casting of the limestone/common sand concrete (LCS) was performed by mixing the concrete constituents listed in Table 2.3 in a paddle mixer. Once a homogeneous mixture was achieved, three test cylinders were cast and slump measurements made. Details of the measurements and other physical data will be discussed in the next sections. Approximately 0.021 m^3 of concrete was required per crucible. The concrete was allowed to cure for a minimum of 60 days before use. Curing was performed at ambient conditions. No special environmental chamber was utilized.

Inspection of the TURC2 crucible revealed that the concrete surface was not perpendicular to the MgO annulus sidewall. Apparently during casting of the concrete slug the plywood platform partially collapsed. To meet a critical deadline, a perpendicular concrete surface was re-established by grinding the concrete slug. Monitoring of the embedded thermocouples during the grinding operation indicated a maximum temperature rise of ~10 K above the ambient temperature. Several thermocouples were destroyed during this procedure. Additionally the relative locations of the thermocouples to the interior surface was, of course, altered. This is reflected in the listed thermocouple positions in Table 2.8.

2.3.2 Crucible Materials

The two major components of the 1-D crucible were limestone/common sand concrete and Kaiser K/R-CAST98* castable MgO refractory. In this section details of the physical and thermal properties of the concrete will be presented. A similar discussion

*Product of the Kaiser Refractory Corp.

3. EXPERIMENTAL RESULTS

3.1 Experimental Procedure

3.1.1 TURC2

The first UO_2 laden TURC series experiment was TURC2. The experiment was initiated by preparing the molten debris in the Large Melt Facility furnace. The melt generator utilized the IRIS technique described in Section 2.2.1. The heating period for TURC2 was approximately 172 min. The maximum temperature recorded by the pyrometer was 2780 K at 140 mins into the heat-up. This temperature was maintained for ~6 mins possibly indicating a phase change, after which the pyrometer output dropped sharply. The lost of output was due to a loss of alignment between the pyrometer and the tungsten sight tube. Apparently the sight tube shifted as a result of movement of molten debris or internal structures (i.e., tungsten ring). Heating was maintained for an additional 21 mins at which time the external thermocouples indicated possible melting of the alumina crucible. At this time the melt was teemed into the interaction crucible by firing the explosive charge through the bottom of the alumina crucible.

The teem was completed in approximately 10 sec after which the sliding portcullis was closed. External observations showed an aerosol cloud escaping from a mating coupling between the LMF and the interaction chamber during the teem. No further aerosol release was observed at the mating coupling or the filter exhaust port after closing the portcullis. (See Figure 2.1.)

The experiment data acquisition was terminated 30 mins after teeming of the melt, when it was apparent that the debris-concrete interactions had abated.

In Section 3.2.1 Posttest Observations, the thermal response of the crucible, gas and aerosol data will be discussed.

3.1.2 TURC3

The TURC3 experiment was initiated in the same manner as TURC2 by the production of the molten debris. The heating period for this experiment was approximately 136 mins, with a maximum temperature of 2473 K indicated by the pyrometer. Once again movement within the crucible shifted the tungsten sight tube making debris temperature measurements impossible. At 136 min the external thermocouples indicated failure of the crucible. At this time the explosive charge was fired, initiating melt teem. Furnace operational diagnostics showed abnormal pressures and

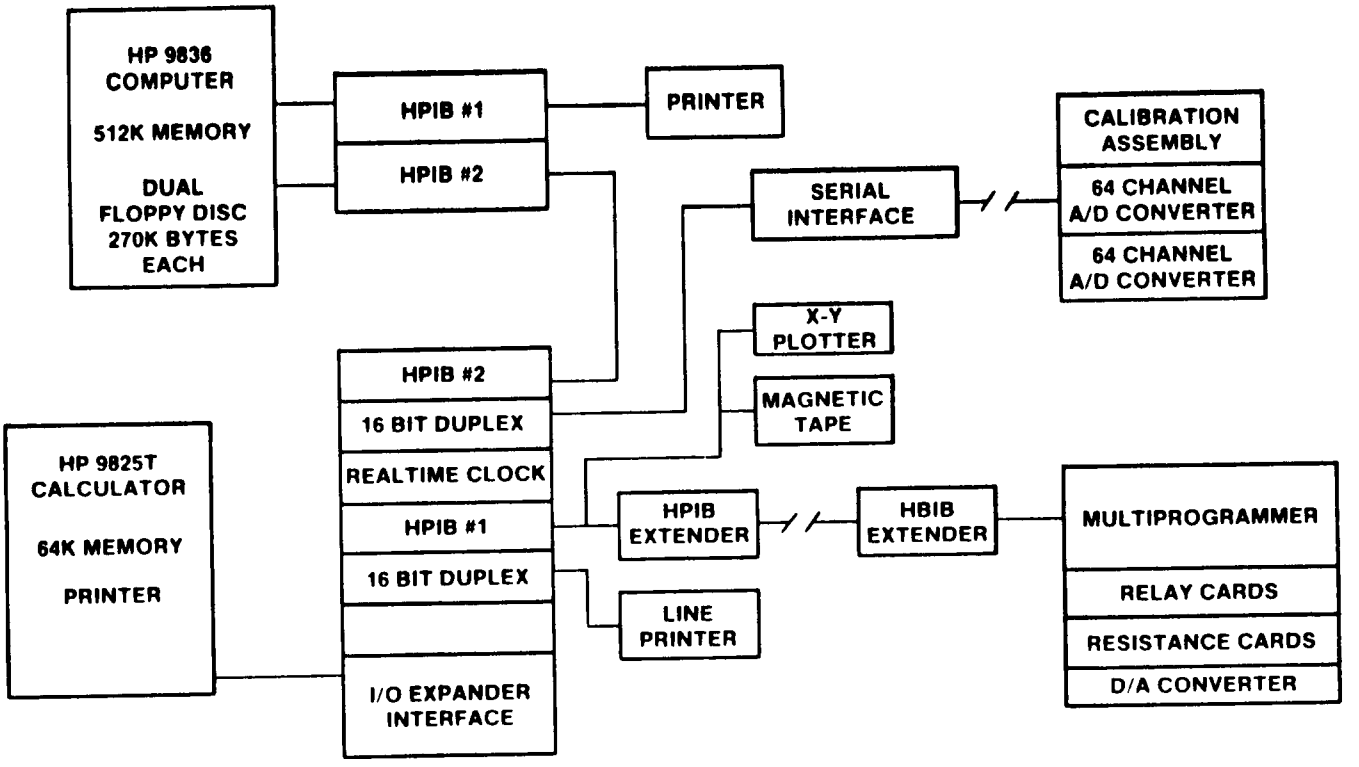

Figure 2.19. Data Acquisition System

$$Q_S = Q_T - Q_D$$

$$D = Q_T/Q_S$$

Note that the sample flow could be eliminated by a high enough dilution gas flow.

The dilution gas is heated to the impactor heater temperature of about 100°C. Its flow is regulated by a critical orifice and remote control valve. The upstream gas pressure controls the dilution gas flow and is set by a pressure regulator. Temperature and pressure upstream of the critical orifice are monitored to give the dilution gas flow rate which was approximately 9 standard liters/min. The diluted sample flow rate is known from the impactor sample flow.

2.4.4 Data Acquisition System

The data acquisition system for the experiment facility is shown schematically in Figure 2.19. One hundred twenty-eight channels of data may be acquired during an experiment. For the TURC experiments, 122 channels were used: 96 channels for type K thermocouples (chromel-alumel), 16 channels for type C thermocouples (tungsten-tungsten rhenium) and 10 channels for voltages up to 10 volts for other types of sensors.

Data are taken in a sample and hold mode in which four channels are measured in a 50 microsecond window. All 122 channels are thus acquired in 1.6 milliseconds. An analog-to-digital converter sequentially converts each channel and sends the data to the computer. At the computer, the data have calibration, correction, and conversion factors applied and are then stored on magnetic tape. In addition, the data may be printed or plotted. The data sampling rate is set by the computer. The fastest mode is one scan of all channels every second. The thermocouples are connected to the acquisition system through a reference junction which is set to 65.5°C.

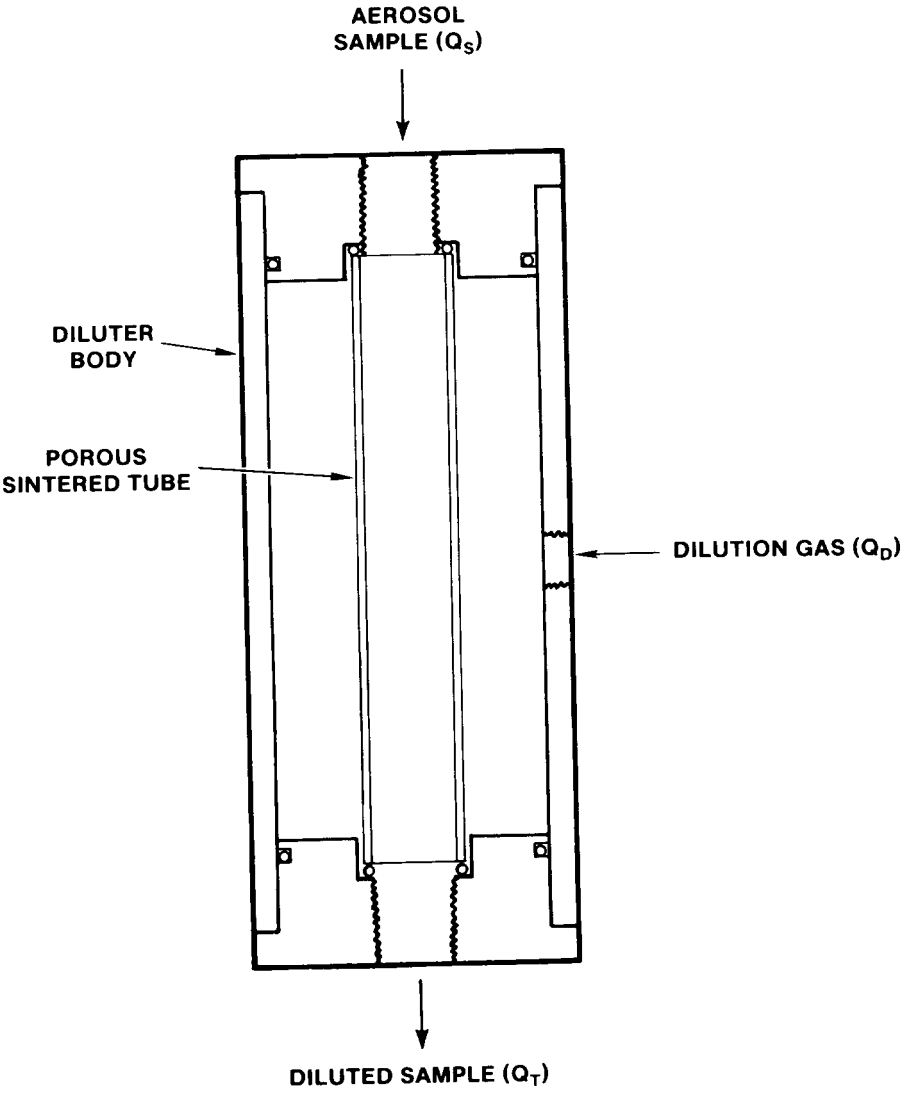

Figure 2.18. Schematic Diagram of Diluter

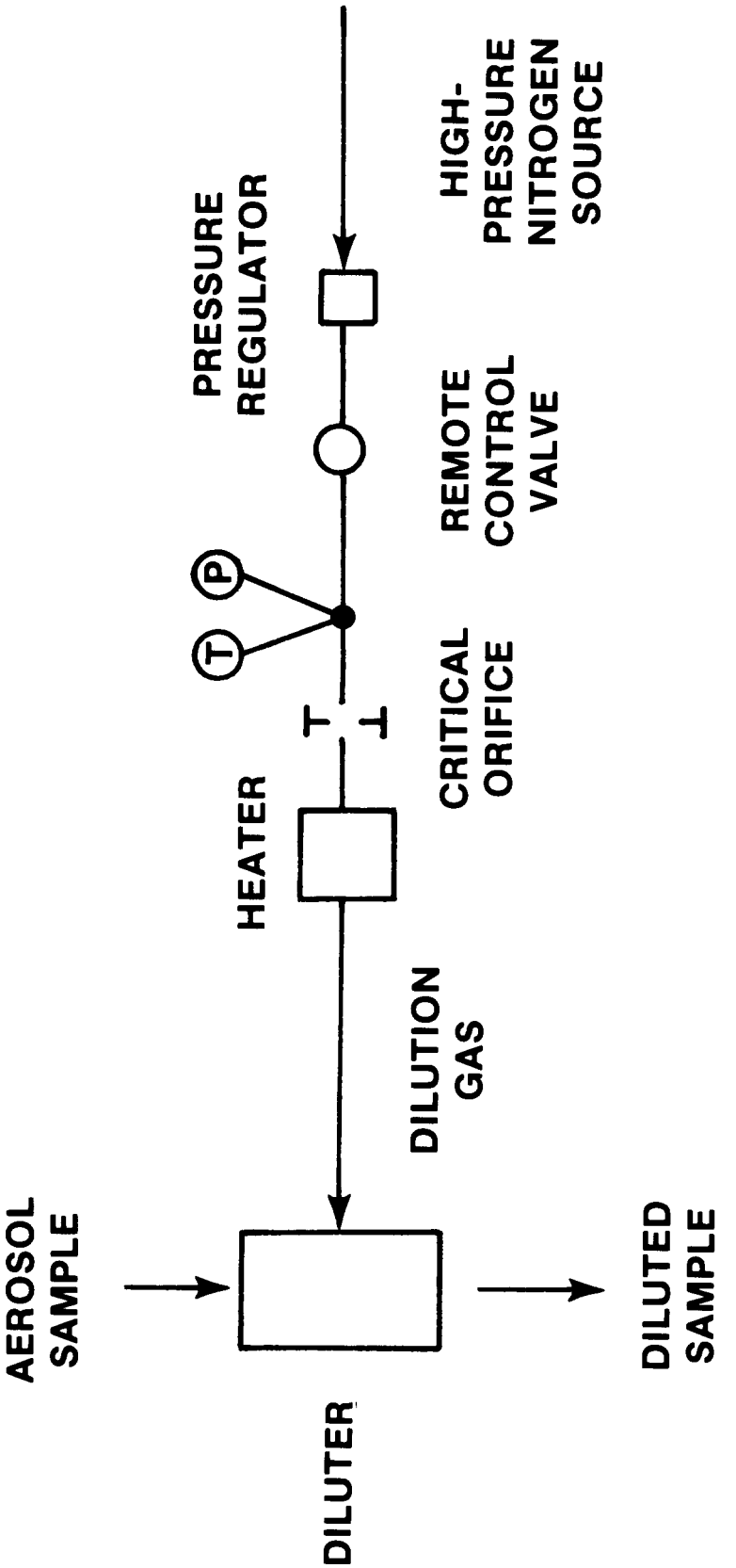

Figure 2.17. Schematic Diagram of Dilution System

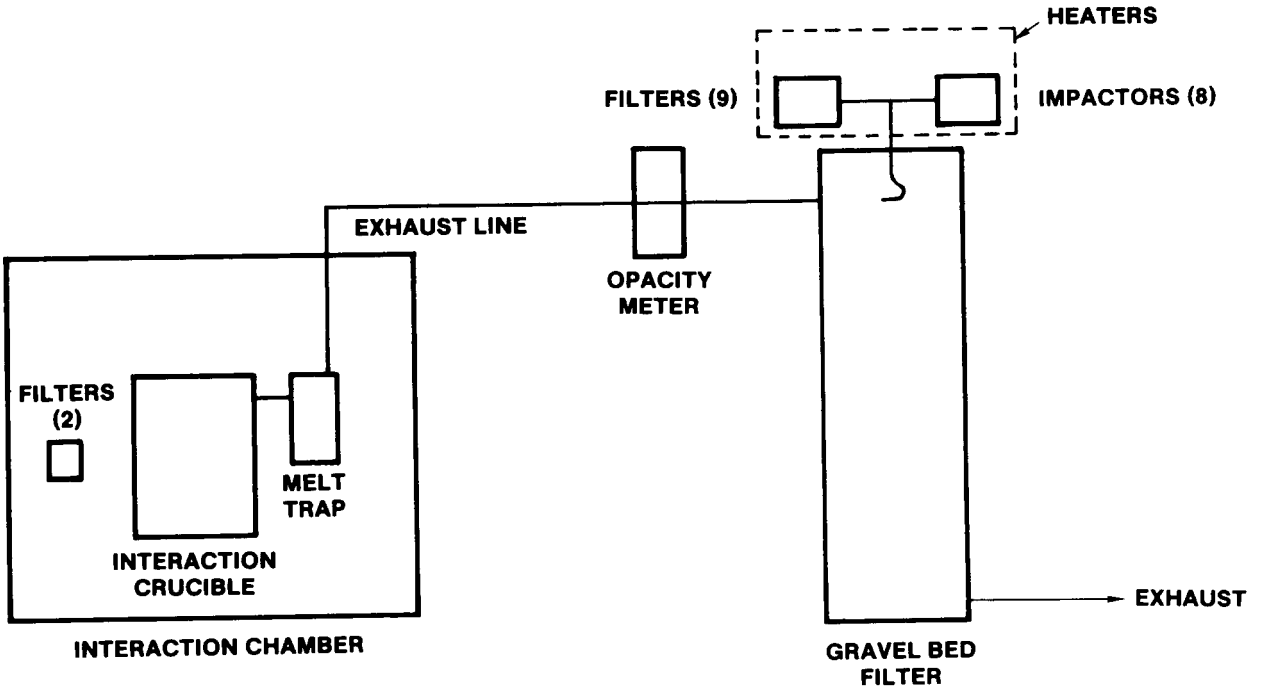

Figure 2.16. Schematic Diagram of TURC3 Location of Sampling Trains

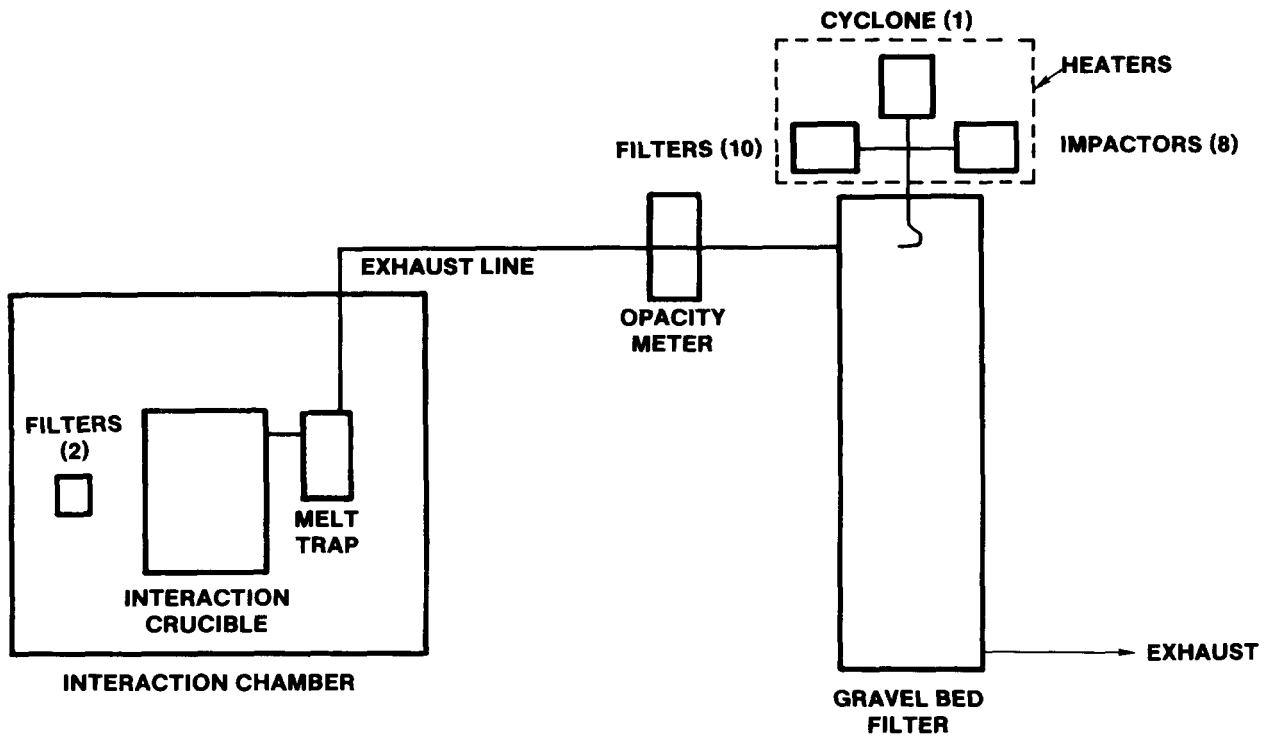

Figure 2.15. Schematic Diagram of TURC2 Location of Sampling Trains

Table 2.10

Aerosol Instrumentation for TURC2 and TURC3

	TURC2	TURC3
Anderson MkIII Cascade Impactors	8	8
Sierra Cascade Cyclone	1	-
Gelman High Pressure Filter Holders	10	9
Millipore Filter Holders	2	2
Dynatron Opacity Meter Model 301	1	1

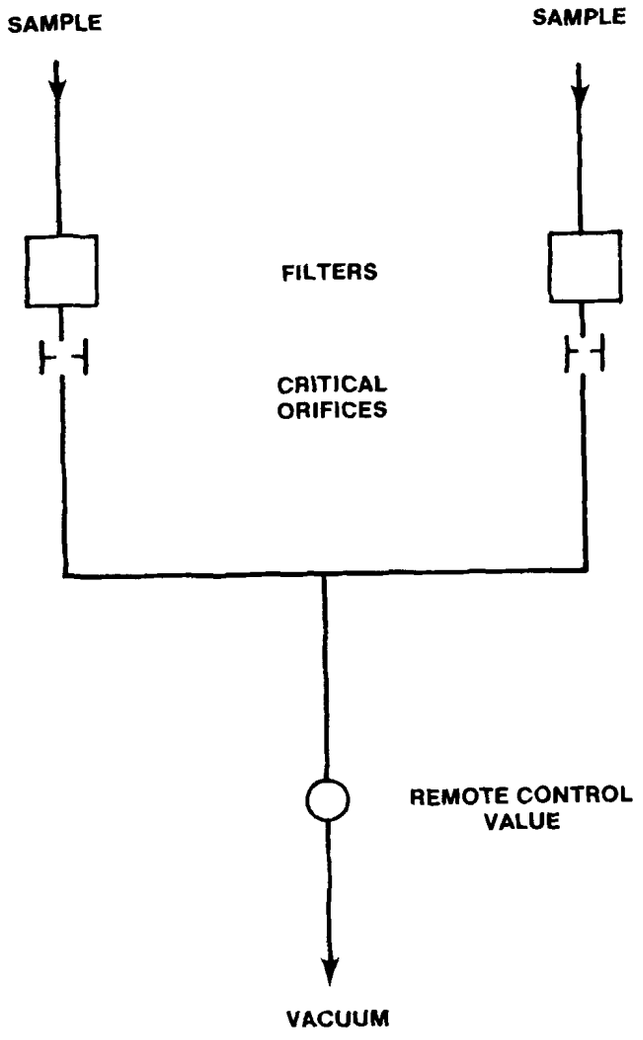

Figure 2.14. Schematic Diagram of Interaction Chamber Filter Sampling Train

concrete interaction. Millipore aerosol filter holders were used for this measurement.

The Millipore Aerosol Standard Filter Holder is 6.9 cm diameter and 17.8 cm long. (Millipore catalog number XX50-04700) It is designed for vacuum applications. The body and flow channel are made of stainless steel and the locking ring is of aluminum. It uses 47-mm diameter Durapore membrane filtration media from Millipore (catalog designation HVLP-047). The effective filtration area is 9.6 cm^2. The filter holder was used in an in-line configuration with the sample drawn through a 0.635-cm diameter inlet. Flow was controlled by a critical orifice at the outlet of the filter holder. Two such filter assemblies were used on each test. Samples were taken simultaneously. Figure 2.14 is a schematic of the interaction chamber filter sampling train. These filters were not heated.

The aerosol instrumentation for TURC2 is listed in Table 2.11. These devices were all connected to a vacuum pump through a system of remotely controlled valves as described in reference 9. Schematics and descriptions of the sampling trains are also contained in reference 9.

Figure 2.15 is a schematic of the TURC2 test showing the location of the sampling trains and opacity meter. The aerosol samples were drawn from the top of the gravel bed filter at the point where the exhaust line from the interaction crucible entered the upper plenum region of the gravel bed filter.

Aerosol Instrumentation on TURC 3

The aerosol instrumentation on the TURC3 test consisted of filter samples, cascade impactors, and an opacity meter and are listed in Table 2.10. No cyclone was used on TURC3 and 9 Gelman filter holders were used instead of 10. The sampling trains and locations are nearly identical to those in TURC2. Figure 2.16 is a schematic of the TURC3 test showing the location of the sampling trains and opacity meter. A modification to the cascade impactor sampling train was made by the addition of upstream aerosol dilution. This is described below.

A schematic of the dilution system is shown in Figure 2.17. The diluter itself (Figure 2.18) consists of a 1.905-cm diameter, 0.159-cm wall sintered stainless-steel tube 11.4 cm long. The tube is encased by an aluminum body leaving an annular region around the sintered tube. The sample is drawn through the porous tube and dilution gas is injected into the annular region flowing through the walls into the tube. The total amount of gas drawn, Q_T, is known, as is the dilution gas flow, Q_D. This allows the calculation of the aerosol sample flow, Q_S, and the dilution rate, D.

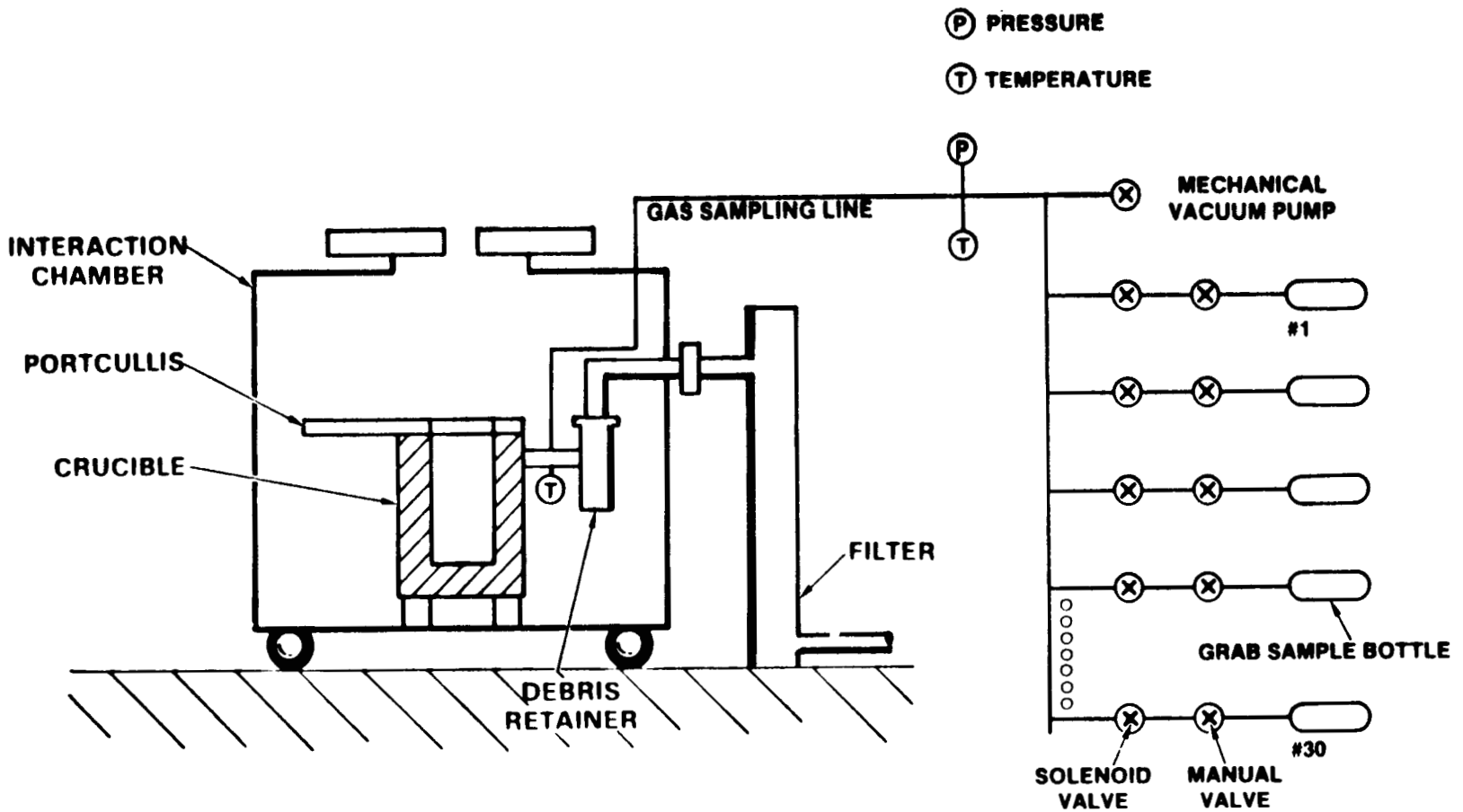

Figure 2.13. Gas Sample Technique for TURC Series of Experiments

The gas sampling system is shown in Figure 2.13. It consisted of a 2-m long sampling line which fed a remotely controlled valve network. A total of 30, 150-cm^3 gas samples can be taken with this equipment. The dead volume within the sample line and valve network was estimated at 50-cm^3, or one-third the sample volume. The sampling rate varied from 5 to 10 seconds between samples early in the experiment to 15 to 30 seconds between samples near the end of the experiment. Since the rate of sampling was almost continuous, the gases sampled were considered a reasonably close representation of the evolved gases.

The gas samples collected were analyzed with an H.P. 5836 Gas Chromatograph. Samples were injected directly from grab sample bottles into a Porapak Q, 80/100 mesh column which was time-temperature programmed from 223 K to 473 K (- 50°C to 200°C).

Detection was accomplished by using a thermal conductivity detector that was tuned to the primary standard gas mixture made up of the following constituents: H_2, N_2, Ar, CO, CH_4, CO_2, C_2H_4, C_2H_6, and O_2. The above gas species were used to calibrate the gas chromatograph. Only peaks that were assignable to the calibration standard were detected.

The sample introduction loop into the gas chromatograph was preceded by an activated charcoal trap that served the purpose of trapping condensibles such as water. This was a necessary step, since previous experiments[5] indicated H_2O was generated in excess of 5% of the total pressure. Also, this procedure served the purpose of preventing saturation or loading of the gas separation columns which would have made quantitative analysis of the gas composition more difficult.

2.4.3 Aerosol Measurements

Aerosol Instrumentation of TURC2

The aerosol instrumentation on the TURC2 test consisted of filter samples for bulk aerosol concentration determination, cascade impactors and cascade cyclones for aerosol size distribution measurement, and an opacity meter to monitor aerosol mass loading in the exhaust pipe. The filters, impactors, and cyclones were plumbed into the sampling train and the flows through the devices were regulated by critical orifices and remotely controlled valves. Descriptions of these devices are given in reference 9 and will not be repeated here.

A measurement taken during the TURC2 and TURC3 tests which was not taken during the TURC1 series of tests was an aerosol filter sample from inside the interaction chamber. This sample was taken just after portcullis closure to determine the concentration in the chamber after the melt teem and hence estimate the aerosol mass source term during the melt teem and initial melt/

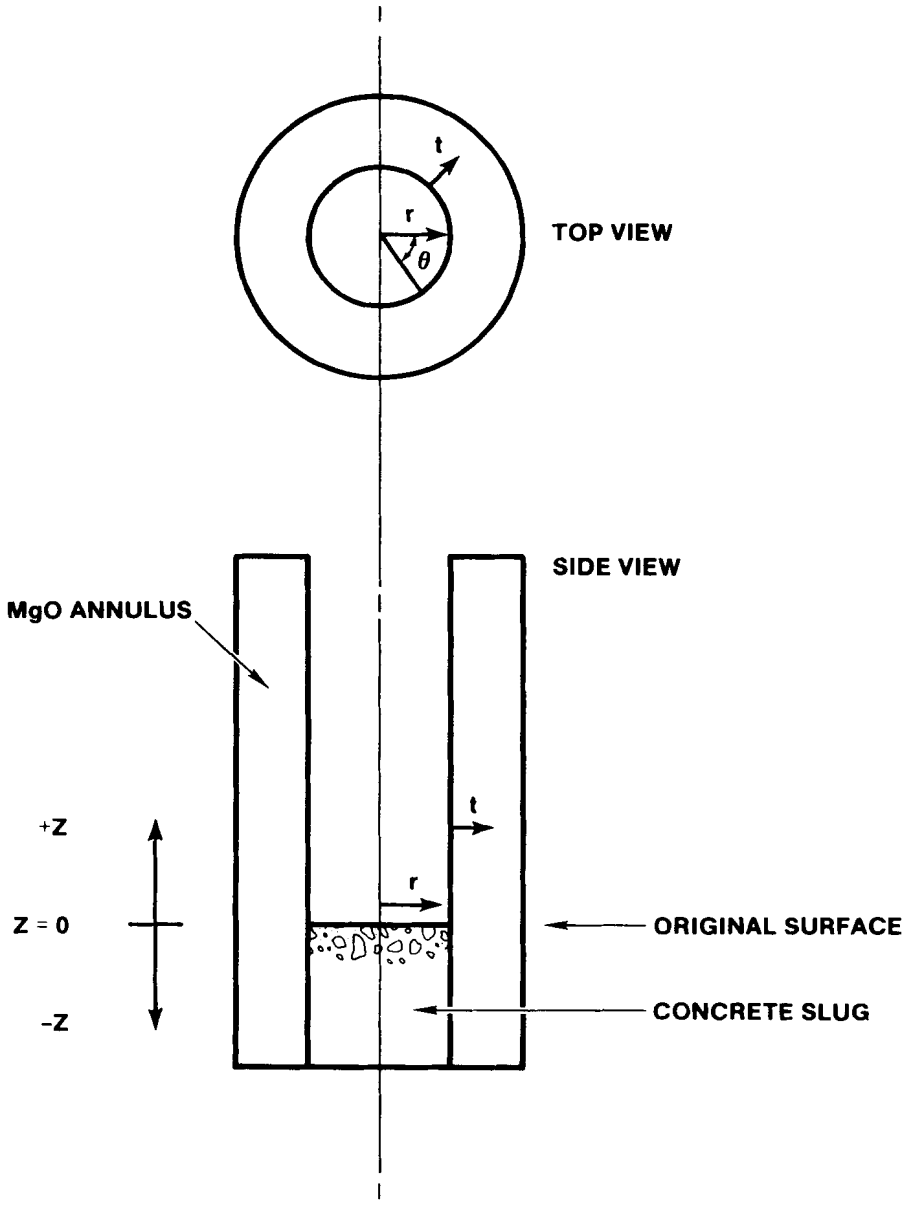

Figure 2.12. Thermocouple Placement Map (see Table 2.7)

Table 2.10

Location of Thermocouples Within the TURC3 Concrete Slug
(See Figure 2.12)

Thermocouple No.	r	θ	z
C1	0 cm	0 deg.	0 cm
C2	0	0	-1.1
C3	0	0	-2.0
C4	0	0	-3.0
C5	0	0	-4.0
C6	0	0	-5.0
C7	0	0	-5.9
C8	0	0	-7.1
C9	0	0	-8.0
C10	0	0	-9.0
C11	0	0	-10.0
C12	0	0	-11.8
C13	0	0	-14.0
C14	0	0	-16.0
C15	0	0	-18.0
C16	3	0	0
C17	3	0	-0.5
C18	3	0	-1.5
C19	3	0	-2.4
C20	3	0	-3.5
C21	3	0	-4.5
C22	3	0	-5.5
C23	3	0	-6.5
C24	3	0	-7.5
C25	3	0	-8.5
C26	3	0	-9.5
C27	3	0	-10.5
C28	3	0	-11.5
C29	18	0	0
C30	18	0	-1.0
C31	18	0	-2.0
C32	18	0	-3.1
C33	18	0	-4.0
C34	18	0	-5.0
C35	18	0	-6.0
C36	18	0	-7.0
C37	18	0	-7.9
C38	18	0	-9.0
C39	18	0	-10.0
C40	18	0	-11.0
C41	18	0	-12.0
C42	18	0	-14.0
C43	18	0	-16.0
C44	18	0	-18.0

Table 2.9

Location of Thermocouples Within the TURC2 Concrete Slug
(see Figure 2.12)

Thermocouple No.	r	θ	z
C1	0 cm	0 deg.	-0.44 cm
C2	0	0	-1.44
C3	0	0	-2.44
C4	0	0	-3.44
C5	0	0	-4.34
C6	0	0	-5.54
C7	0	0	-6.44
C8	0	0	-7.44
C9	0	0	-8.44
C10	0	0	-10.24
C11	0	0	-12.44
C12	0	0	-14.44
C13	0	0	-16.44
C16	3	0	0.00
C17	3	0	-0.64
C18	3	0	-2.64
C19	3	0	-2.44
C20	3	0	-3.44
C21	3	0	-4.44
C22	3	0	-5.44
C23	3	0	-6.44
C24	3	0	-7.44
C25	3	0	-8.44
C26	18	0	-0.24
C27	18	0	-1.34
C28	18	0	-2.24
C29	18	0	-3.24
C30	18	0	-4.24
C31	18	0	-5.24
C32	18	0	-6.14
C33	18	0	-7.24
C34	18	0	-8.24
C35	18	0	-9.24
C36	18	0	-10.24
C37	18	0	-12.24
C38	18	0	-14.24
C39	18	0	-16.24

Table 2.8

Location of Thermocouples within MgO Sidewall
(see Figure 2.12) TURC3

Thermocouple Designation	r	θ	z
MG1	0 cm	0 deg.	0 cm
MG2	1	0	0
MG3	2	0	0
MG4	3	0	0
MG5	0	0	+5.2
MG6	1	0	+5.2
MG7	2	0	+5.2
MG8	3	0	+5.2
MG9	0	90	+15.0
MG10	1	90	+15.0
MG11	2	90	+15.0
MG12	3	90	+15.0
MG13	0	90	+30.0
MG14	1	90	+30.0
MG15	2	90	+30.0
MG16	3	90	+30.0
MG17	0	90	+60.0
MG18	1	90	+60.0
MG19	2	90	+60.0
MG20	3	90	+60.0
MG21	0	0	-5.1
MG22	1	0	-5.1
MG23	2	0	-5.1
MG24	3	0	-5.1
MG25	0	0	-10.0
MG26	1	0	-10.0
MG27	2	0	-10.0
MG28	3	0	-10.0

Table 2.7

Location of Thermocouples within MgO Sidewall
(see Figure 2.12) TURC2

Thermocouple Designation	r	θ	z
MG1	0 cm	0 deg.	2 cm
MG2	1	0	2
MG3	2	0	2
MG4	3	0	2
MG5	0	0	+7.2
MG6	1	0	+7.2
MG7	2	0	+7.2
MG8	3	0	+7.2
MG9	0	90	+17.0
MG10	1	90	+17.0
MG11	2	90	+17.0
MG12	3	90	+17.0
MG13	0	90	+32.0
MG14	1	90	+32.0
MG15	2	90	+32.0
MG16	3	90	+32.0
MG17	0	90	+62.0
MG18	1	90	+62.0
MG19	2	90	+62.0
MG20	3	90	+62.0
MG21	0	0	-3.1
MG22	1	0	-3.1
MG23	2	0	-3.1
MG24	3	0	-3.1
MG25	0	0	-8.0
MG26	1	0	-8.0
MG27	2	0	-8.0
MG28	3	0	-8.0

agent (AE) was added to the concrete mix per ASTM C-494-71 specifications. Additionally, a curing compound was applied to the concrete surfaces. The curing compound, BURKE Res-X*, was applied at the recommended rate of coverage. It forms a thin film that inhibits the evaporation of water from the concrete, thus assuring a constant supply of water for hydration of the Portland cement. The thin film oxidizes and dissipates after exposure to air for 45 to 60 days.

2.4 Experiment Instrumentation

The instrumentation utilized in the TURC2 and TURC3 experiments consisted of embedded thermocouples within the interaction crucible, grab sampling of evolved gas, and aerosol measurements. The following sections will describe the instrumentation as well as the data acquisition system.

2.4.1 Crucible Instrumentation

Instrumentation within the crucible consisted of K-type thermocouples located within the concrete slug and MgO annulus. The thermocouples were utilized to determine concrete erosion rates, location of the physical isotherms (such as the concrete dehydration front), and for the determination of heat fluxes into the concrete and MgO sidewalls.

Axial temperature profiles within the concrete slug were measured at three radial locations (0, 3, and 18 cm from centerline). Overall thermocouple axial separation resulted in a spatial resolution of 0.5 cm. Additional thermocouple arrays located within the MgO annulus measured radial temperature profiles at several axial locations. Tables 2.7 through Table 2.10, and Figure 2.12 summarize the thermocouple locations.

A heat flux gauge was constructed within the sliding crucible portcullis to measure the upward heat flux from the melt pool surface. The gauge consisted of a 2.5 cm mild steel slug, 1.3 cm in height, in which two K-type thermocouple were embedded with an axial separation of 5 mm. The front face of the gauge was exposed to the crucible interior when the portcullis was closed. (The back surface was heavily insulated.) The thermocouple data was analyzed by the IHCP code discussed in Section 3.2.1.2 to calculate the heat flux due to radiative and convective heat transfer from the melt pool.

2.4.2 Gas Measurements

The composition of the gases generated during the test were determined from grab samples. The gases were sampled at the exit port of the interaction crucible.

---

*Burke Res-X is a product of Burke Concrete Accessories, Inc.

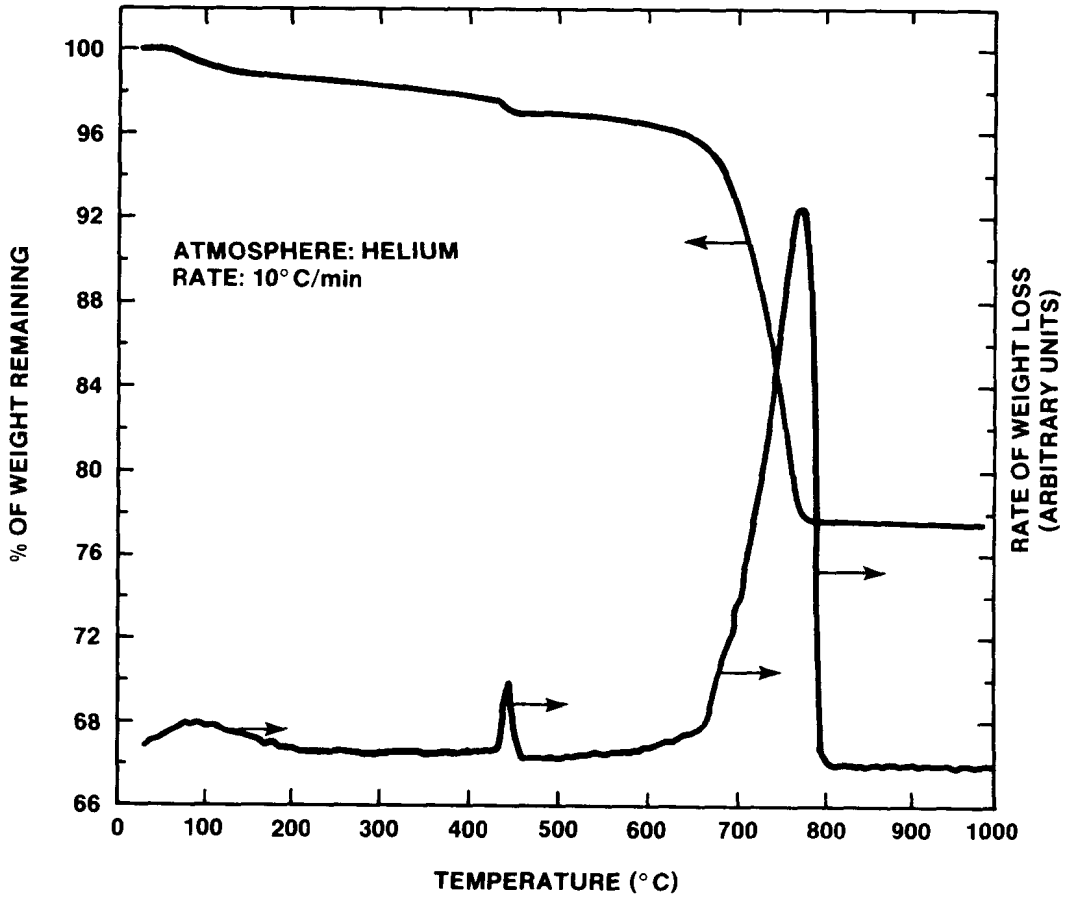

Figure 2.11. Thermogram (TGA) of Limestone/Common Sand Concrete

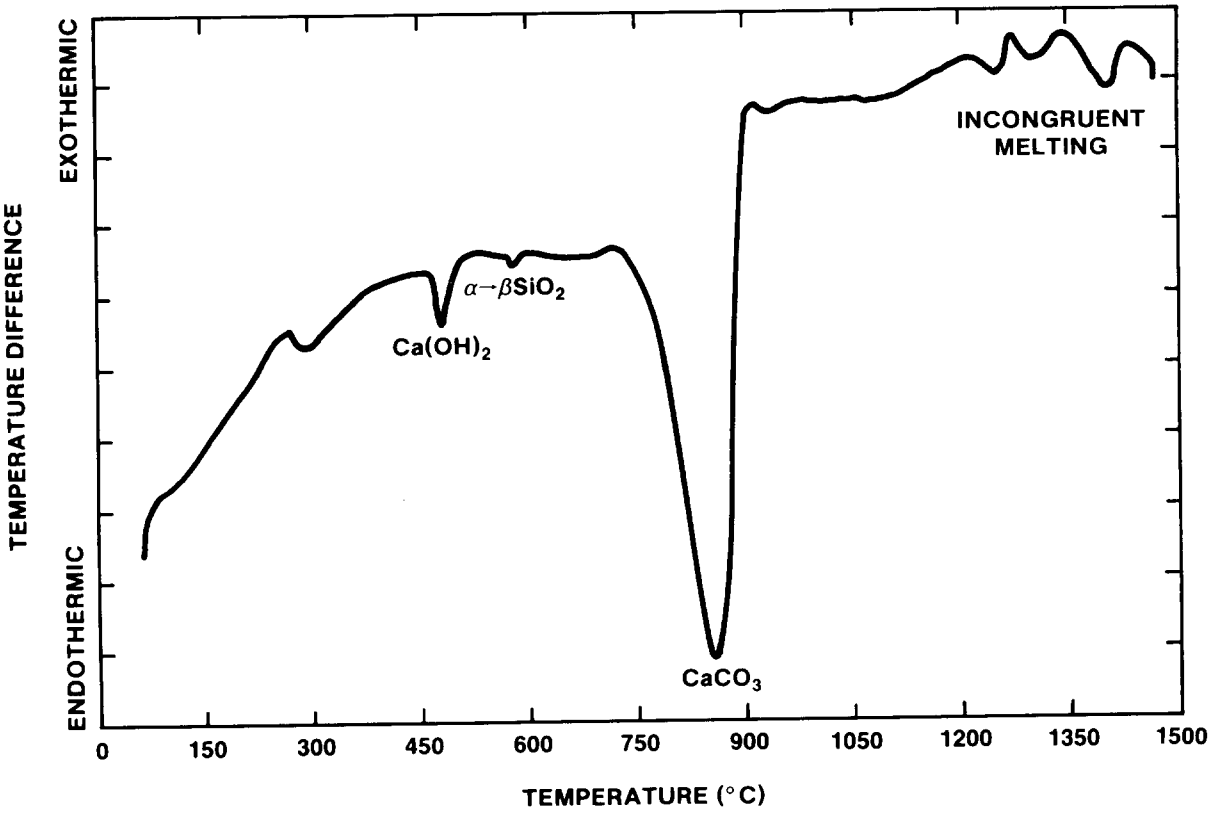

Figure 2.10. Differential Thermogram of Limestone/Common Sand Concrete

Table 2.6

Stoichiometry of Thermal Events in the Decomposition of Limestone/Common Sand Concrete (Cured 90 Days)

Thermal Events	Limestone/ Common Sand Concrete
Free water (weight %)	2.7 ± 0.3
Enthalpy of free water loss* (KJ/kg)	81.6 ± 9.0
Bound water (weight %)	2.0 ± 0.3
Enthalpy of bound water loss (KJ/kg)	120 ± 20
Carbon dioxide (weight %)	22.0 ± 0.7
Enthalpy of carbon dioxide loss (KJ/kg)	962 ± 50
Free SiO_2 (weight %)	30 ± 2
Enthalpy of SiO_2 phase change (KJ/kg)	3.1 ± 0.5
Melting temperature range (K)	1423 to 1673
Enthalpy of melting (KJ/kg)	500 ± 75

*All enthalpic values are reported as KJ/kg virgin concrete

Table 2.5

Chemical Compositions of the Limestone/Common Sand Concrete and the Concrete Constituents

Oxide	Cement w/o	Limestone/ Common Sand Concrete w/o	Expected Error w/o
Fe_2O_3	4.11	1.44	0.3
Cr_2O_3	0.011	0.014	0.01
MnO	0.08	0.03	0.02
TiO_2	0.2	0.18	0.04
K_2O	0.54	1.22	0.4
Na_2O	0.27	0.82	0.2
CaO	63.5	31.2	1.0
MgO	1.53	0.48	0.5
SiO_2	20.1	35.7	1.5
Al_2O_3	4.2	3.6	0.2
CO_2	ND	22	1.0
H_2O	ND	4.8	0.5
SO_2	1.0	<0.2	0.2

Table 2.4

Concrete Casting Data

Test	Concrete Type	Cure (days)	Cold Compressive Strength After 28 Days (MPa)
TURC2	LCS	61	28.7
TURC3	LCS	147	28.4

describing the physical and thermal properties of the castable MgO material is presented in reference 9.

The concrete used in the TURC series of experiments, limestone/common sand, was chosen because of its composition and physical characteristics between that of basaltic (siliceous) and limestone (calcareous) concretes.[3]

Due to the transient nature of the TURC experiments the initial energy in the molten debris is the driving potential behind the debris-concrete interaction. It is also apparent that one of the largest losses of energy from the molten debris occurs during the decomposition and melting of the concrete. Thus, a concrete with a low enthalpy of decomposition and melting is desirable to achieve a prolonged interaction time for a given energy inventory within the melt.

A comparison of the three principal concrete types found in American reactors shows that the basaltic concrete has the lowest enthalpy of heating, decomposition and melting (2000 J/g), followed by limestone/common sand (2800 J/g), and limestone (4000 J/g).[3] Thus, based on thermal characteristics, basaltic concrete would be the most desirable concrete for the TURC experiments.

Other characteristics of interest in these preliminary large-scale molten debris-concrete interaction experiments are the physical source terms of combustible gas production (H_2 and CO) and the transport of fission products from the molten debris. In order to provide an experimental environment in which these source terms could be observed, a significant source of gas release from the decomposing concrete was desirable.

The two major gases released from decomposing concrete are water vapor and carbon dioxide. The water released from all three types of concrete is approximately the same, but the carbon dioxide release is significantly different. Limestone concrete contains the highest CO_2 content of concretes at 35.7 w/o followed by limestone/common sand at 22.0 w/o, and basaltic containing only 1.5 w/o. Based on an experimental gas-release criteria, limestone concrete is the most desirable.

Thus, in order to address both experimental thermal and physical considerations the limestone common sand (LCS) concrete was chosen. A fairly complete description of the chemical, physical, and thermal characteristics of limestone/common sand concrete was presented by Powers.[3] Portions of the Powers data are presented in Tables 2.5 and 2.6 and Figures 2.10 and 2.11.

A summary of the concrete casting data for the two experiments is shown in Table 2.4.

The mixing, forming, and casting of the concrete follow establish procedures for the industry.[14] An air entrainment

Table 2.3

Composition of Limestone/Common Sand Concrete

Item	Proportion	Fraction
Cement, type I & II	42.7 kg	0.15
Water	19.1	0.07
Concrete Sand (common)	93.2	0.33
Aggregate, Limestone 1.9 cm max.	85	0.031
Limestone Sand	42.3	0.14
Air Entrainment Agent (AE)	0.021	
TOTAL	282.3 kg	1.00

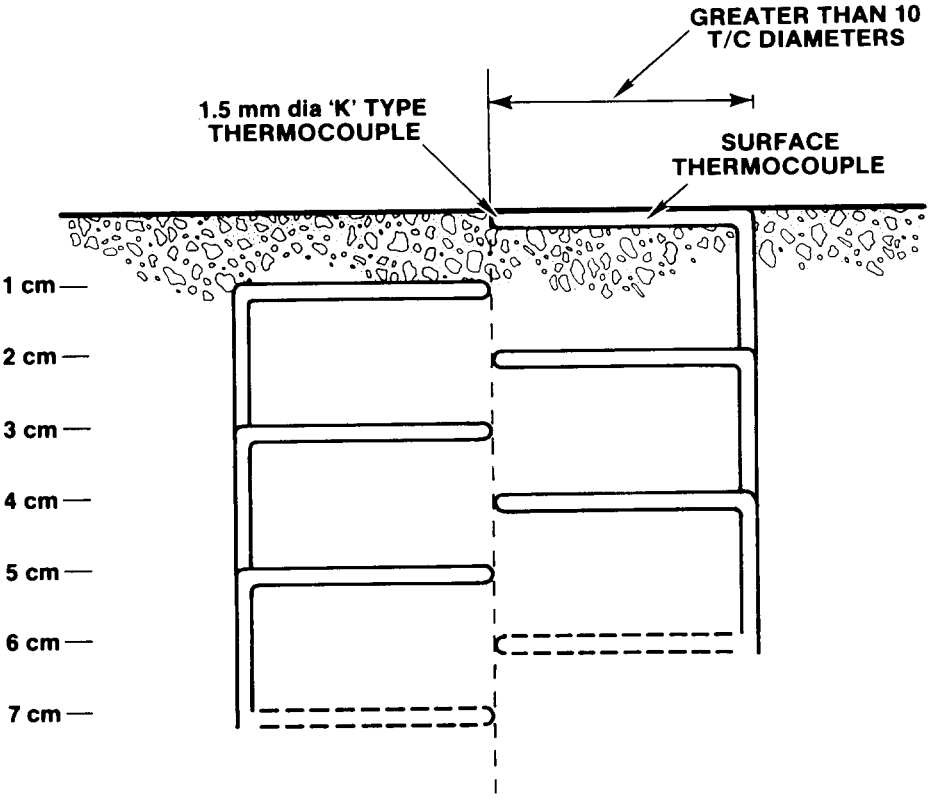

Figure 2.9. Concrete Thermocouple Array Details

temperatures within the furnace shell. Once the teeming was completed, the interaction crucible portcullis was closed. As with the TURC2 experiment, a relatively benign melt-concrete interaction was observed. The experiment duration was similar to TURC2. The acquisition of data was terminated 20 mins after the melt teem.

The TURC3 experimental results are presented in Section 3.2.2.

3.2 Experimental Results

3.2.1 TURC2

3.2.1.1 Posttest Observations

Following a cool-down period of two days, the TURC2 experiment crucible was removed from the interaction chamber. The crucible was covered and stored for several months until the completion of the TURC series of experiments.

An external examination of the TURC2 crucible showed little damage from the intense internal experiment environment. Unlike the TURC1 series crucibles, no external cracks were found.

The portcullis was removed to gain access to the interior of the crucible. Inspection of the interior sidewall revealed a crust 1-3 cm thick, extending 35-40 cm above the top surface of the melt pool. Above the crusted sidewall, a deposit of fine particulate adhering to the MgO was found.

As shown in Figure 3.1, the top surface of the melt pool was convoluted and cracked with 2-5 mm diameter depressions or dimples uniformly distributed over the surface.

An X-ray of the lower portion of the crucible is shown in Figure 3.2. The X-ray shows a solidified pool approximately 12.5 cm thick. The solidified pool appears to be in contact with the concrete slug. No apparent concrete erosion was observed. Along the melt pool-MgO sidewall interface a gap of several millimeters is apparent. The upper sidewall crust is clearly visible above the melt pool.

The crucible was sectioned by removing a 120° arc of the MgO annulus, exposing the interior sidewall, melt pool, and concrete slug. The melt pool was partially removed, as shown in Figure 3.3, to expose the melt-concrete interface and interior structure of the melt pool.

The melt pool was fragmented in numerous large chunks with a characteristic length of 3-6 cm. The pool material contained numerous voids 2-5 mm in diameter which were uniformly distributed. The voids were most likely the result of solidification

Figure 3.1. Posttest Photograph of Top Surface of TURC2 Melt Pool

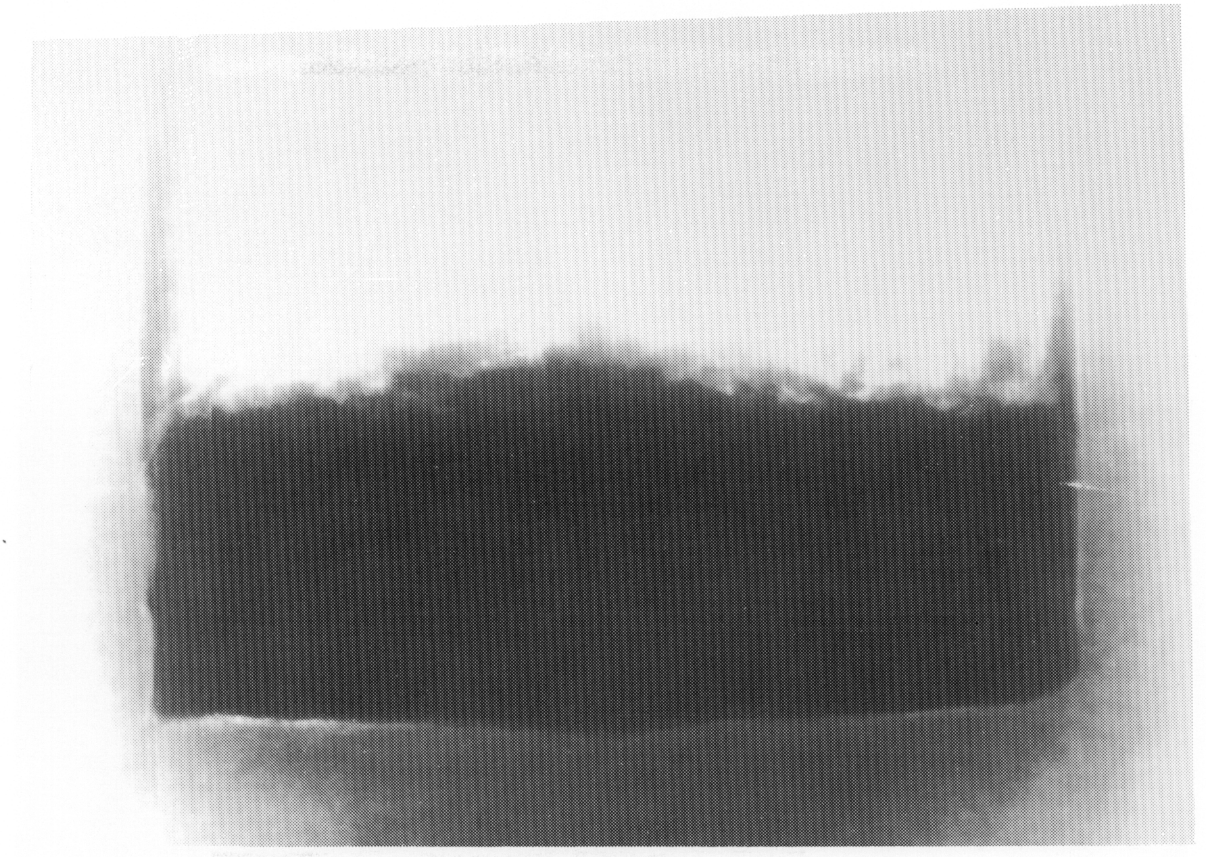

Figure 3.2. Posttest X-ray of Lower Section of TURC2 Crucible

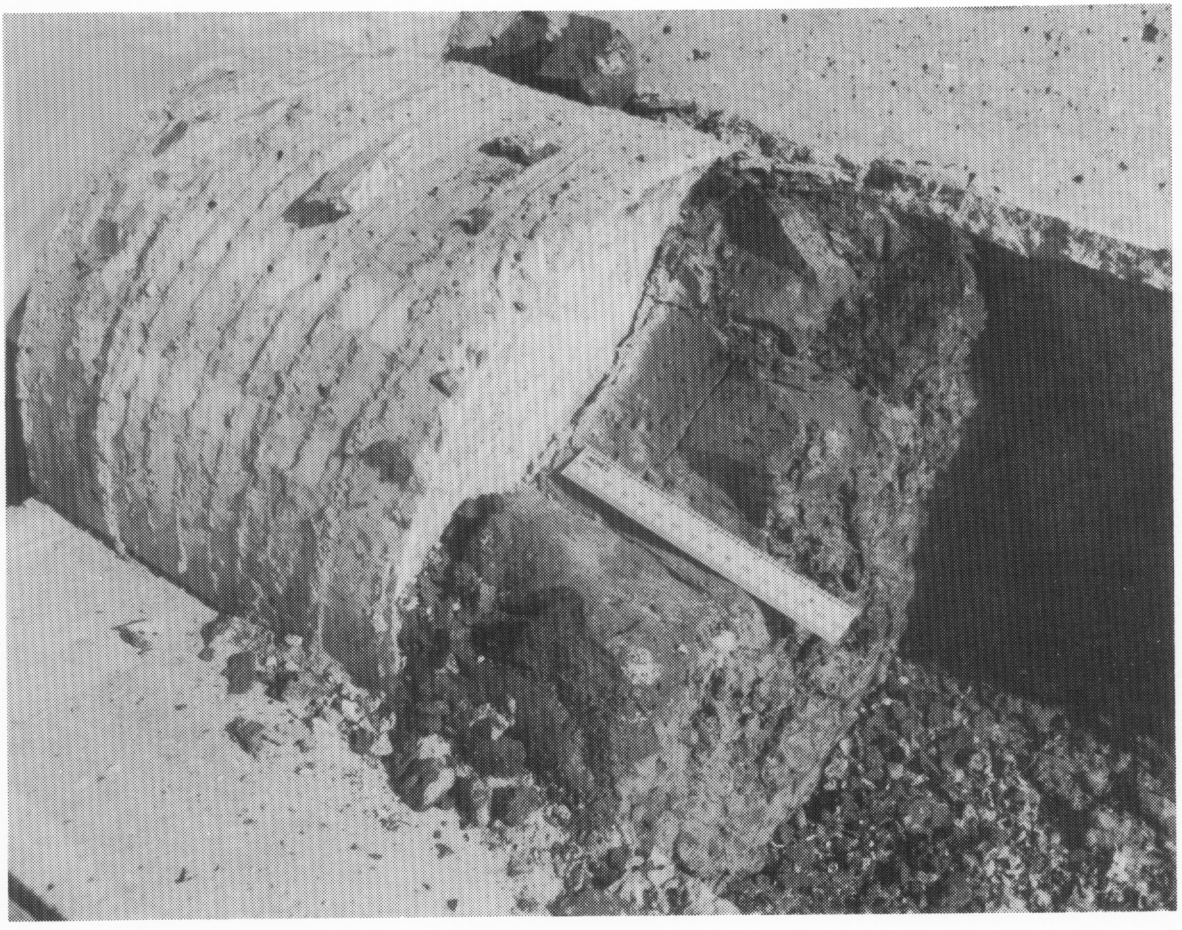

Figure 3.3. Sectioned Crucible of TURC2 Experiment

of the melt pool. With the exception of the melt-concrete interface, the melt pool was uniform in color.

An examination of the melt pool-concrete interface showed what appeared to be concrete constituents diffusing into the melt pool over a length of ~1 cm. The structure of the pool material in direct contact with the concrete appeared to be thin crusts (~1-3 mm thick) followed by a gas gap and the bulk of the pool material. The crust material was porous and firmly adhered to the concrete. The crust structure was also found along the melt pool-MgO annulus interface within an axial elevation of a few cm from the concrete interface.

The molten pool-MgO wall interface was examined. As mentioned above, the thin crust structure found at the concrete interface was also formed at the wall. The MgO wall material showed little thermal degradation. No gross evidence of chemical attack of the MgO wall by the melt pool was found.

The solidified pool material was removed from the crucible. The mass of the solidified pool was 103.6 kg and the crust above the solidified pool was 40.4 kg. The upper concrete surface was white (most probably due to decomposition of $CaCO_3$). The concrete surface location indicated very little, if any, ablation (less than 5 mm). The degradation of the concrete surface was uniform and there was no evidence of pool material diffusion into the concrete.

The TURC2 solidified pool debris was fractured for sample preparation and disposal. During this activity several tungsten components were found at the bottom surface of the debris pool. It is speculated that during the teeming of the melt pool, several broken ring support rods were entrained into the molten debris. The tungsten rods settled within the molten debris onto or near the concrete underface. It is clear from their location that the rods were exposed to the decomposing concrete.

3.2.1.2 TURC2 Concrete and MgO Annulus Thermal Response

The temperatures indicated by thermocouples imbedded at selected depths within the concrete slug are shown in Figures 3.4 through 3.6. Based on these data, several observations are made.

The erosion front through concrete has in the past been successfully tracked by the failure of thermocouple junctions embedded within the concrete slug. Utilizing this technique no concrete erosion was observed within the concrete slug. This is consistent with the posttest inspection of the concrete slug.

A review of the shallow embedded thermocouple data indicates higher maximum temperatures at the radial centerline than at r = 18 cm. This observation indicates the heat flux into the concrete was less at the outer radius than toward the center of the concrete slug.

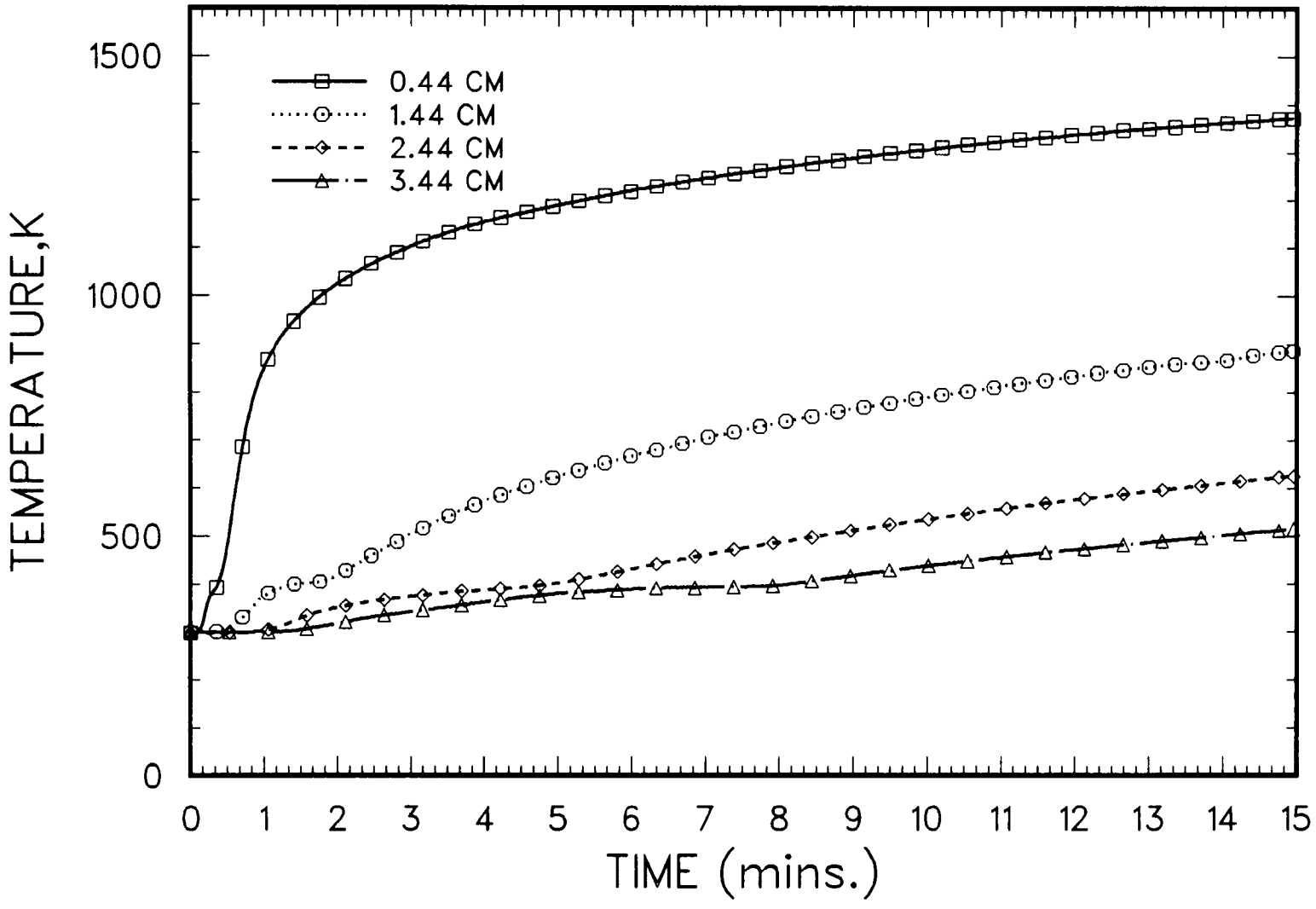

Figure 3.4. TURC2 Concrete Thermocouple Data, Location: Concrete Slug Centerline

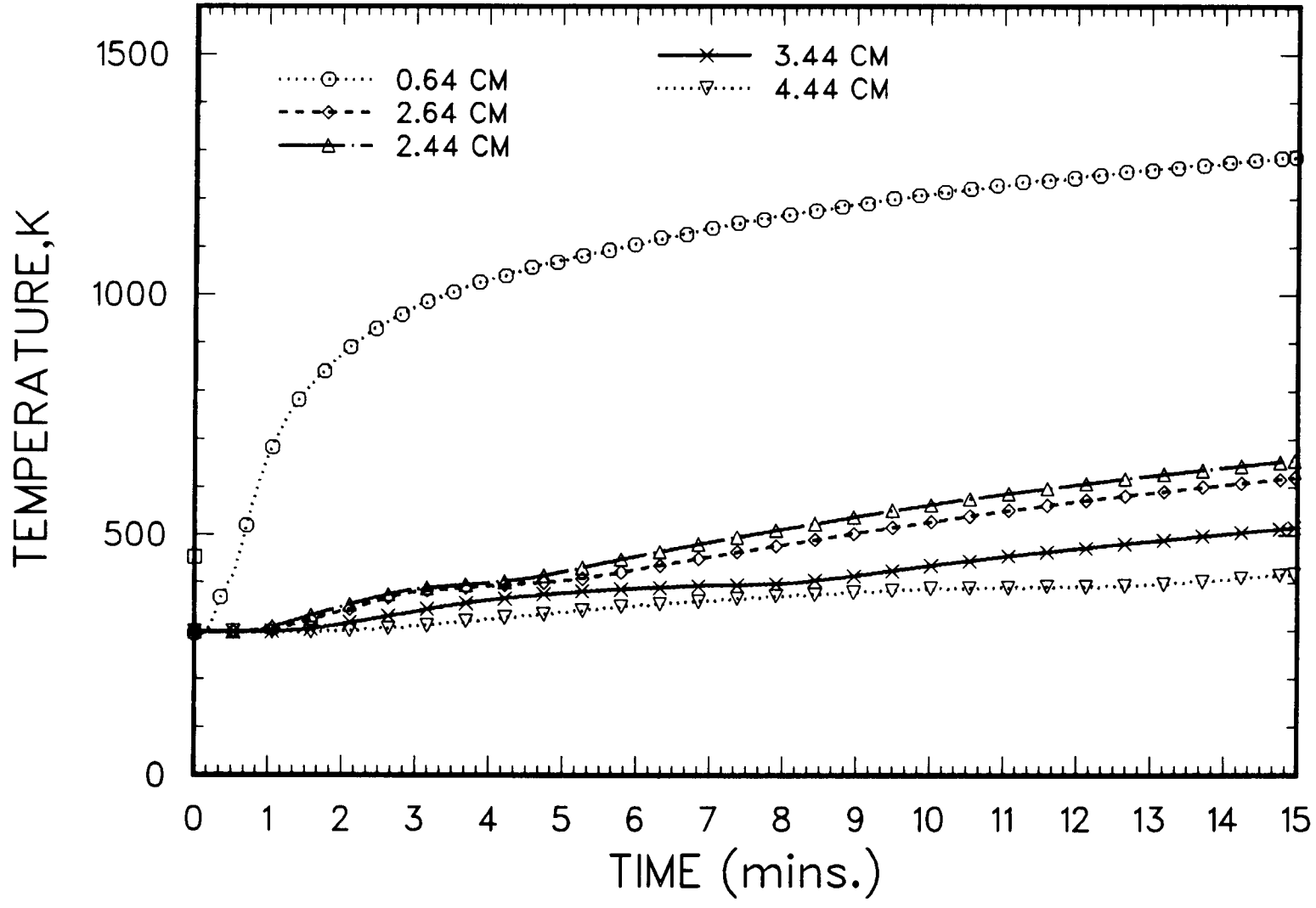

Figure 3.5. TURC2 Concrete Thermocouple Data, Location: r = 3 cm

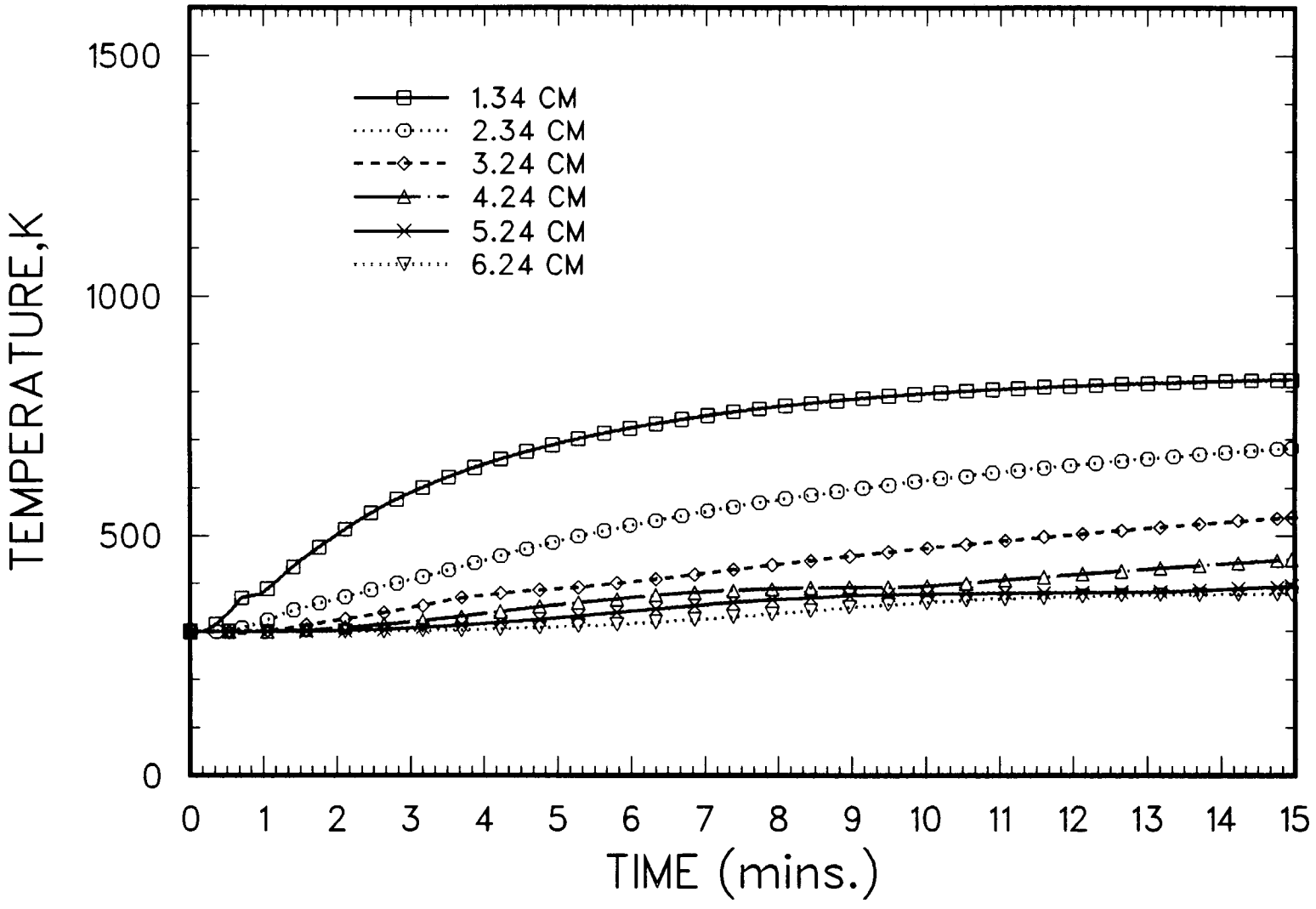

Figure 3.6. TURC2 Concrete Thermocouple Data, Location: r = 18 cm

A review of the temperature traces of thermocouples embedded within the concrete shows a distinct thermal arrest at approximately 400 K is observed; where the evaporable water vaporizes and escapes from the concrete. This transition zone to a dehydrated concrete is referred to as the wet-dry interface. Figure 3.7 is a plot of the location of the wet-dry interface. A comparison of the locations of the wet-dry interface at various radical locations suggests the outer radius region of the concrete was exposed to a lower heat flux than toward the center of the slug. This is supported by the magnitude of the temperatures discussed above.

As will be apparent in Section 4.0, the heat flux into the MgO annulus is a required measurement in order to perform a global energy balance. A direct measurement of the MgO heat flux is a difficult task to perform within the experiment environment. As discussed in Section 2.3, several arrays of thermocouples were embedded within the MgO annulus. Calculation of the heat flux into the MgO, at several axial elevations, was based upon the thermal histories as measured by these thermocouples.

The calculation of heat flux to the MgO walls is a classic example of an "inverse" heat conduction problem (IHCP) where the boundary condition (e.g., heat flux) is determined from known interior temperatures. Of the available methods for solving the IHCP, the one that appears to be the most successful for the widest variety of applications is the nonlinear estimation technique proposed by Beck.[15] In this method, the calculated heat flux is that value which minimizes the square of the differences between the calculated and experimental temperatures. A computer code, IHCP, has been written based on Beck's methods by Bradley.[16] The code, IHCP, was tested using a variety of exact solution problems and was found to perform well. The accuracy of this method is strongly dependent upon the accuracy of the thermocouple temperature data. In general, it was found that the greater the number of thermocouples utilized in the analysis, the greater the accuracy of the solution. However, Bradley found that beyond three thermocouples, the improvement in accuracy was not sufficient to justify additional thermocouples. The experimental data recorded, and utilized in IHCP, consisted of at least three thermocouples at depths ranging from the surface to 3 cm into the MgO sidewall.

The results of the IHCP heat flux calculation are shown in Figures 3.8 and 3.9 for axial locations: 2 and 7 cm above the melt-concrete interface. (Figures 3.10 and 3.11 show the thermocouple data for these locations.) Both results show similar characteristics of an elevated heat flux followed by a steady decrease. Note that the heat flux decreases more rapidly at the melt-concrete interfaces than 5 cm above it. This behavior is expected because of the two-dimensional heat transfer that occurs near the interface. The two-dimensional heat transfer causes the melt near the interface to cool more rapidly.

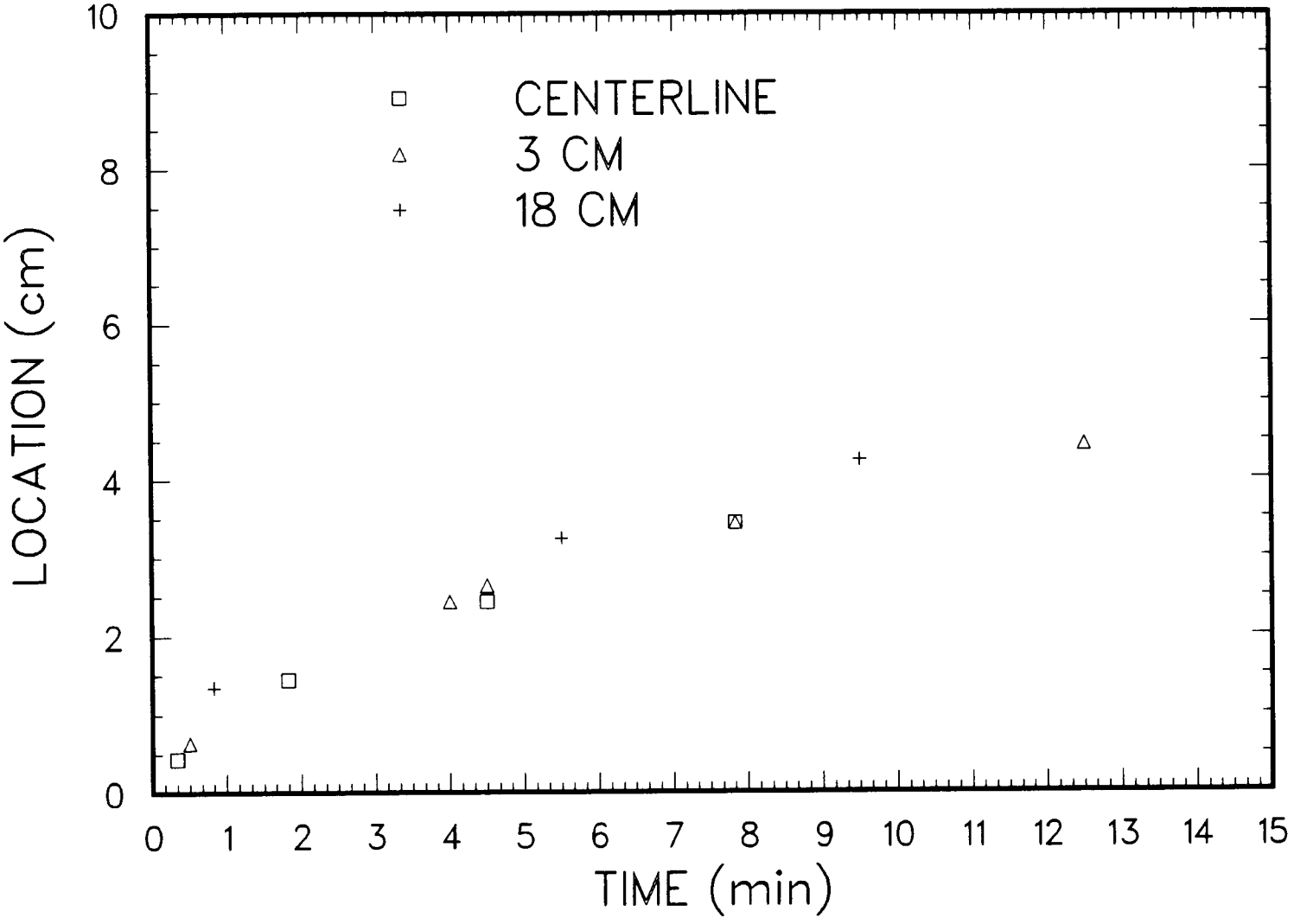

Figure 3.7. TURC2 Wet/Dry Interface Location

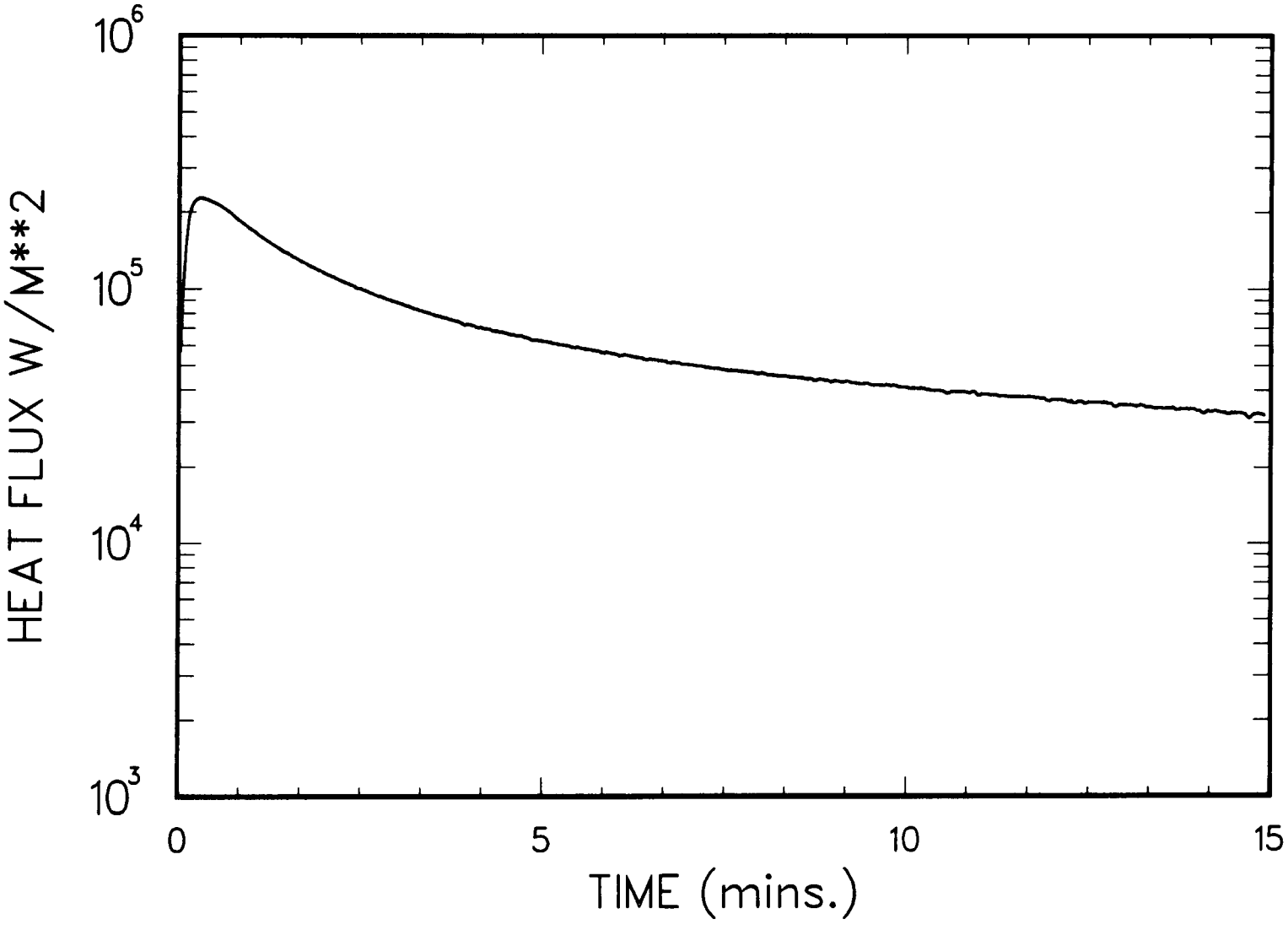

Figure 3.8. TURC2 MgO Sidewall Heat Flux at 2 cm Above the Melt-Concrete Interface

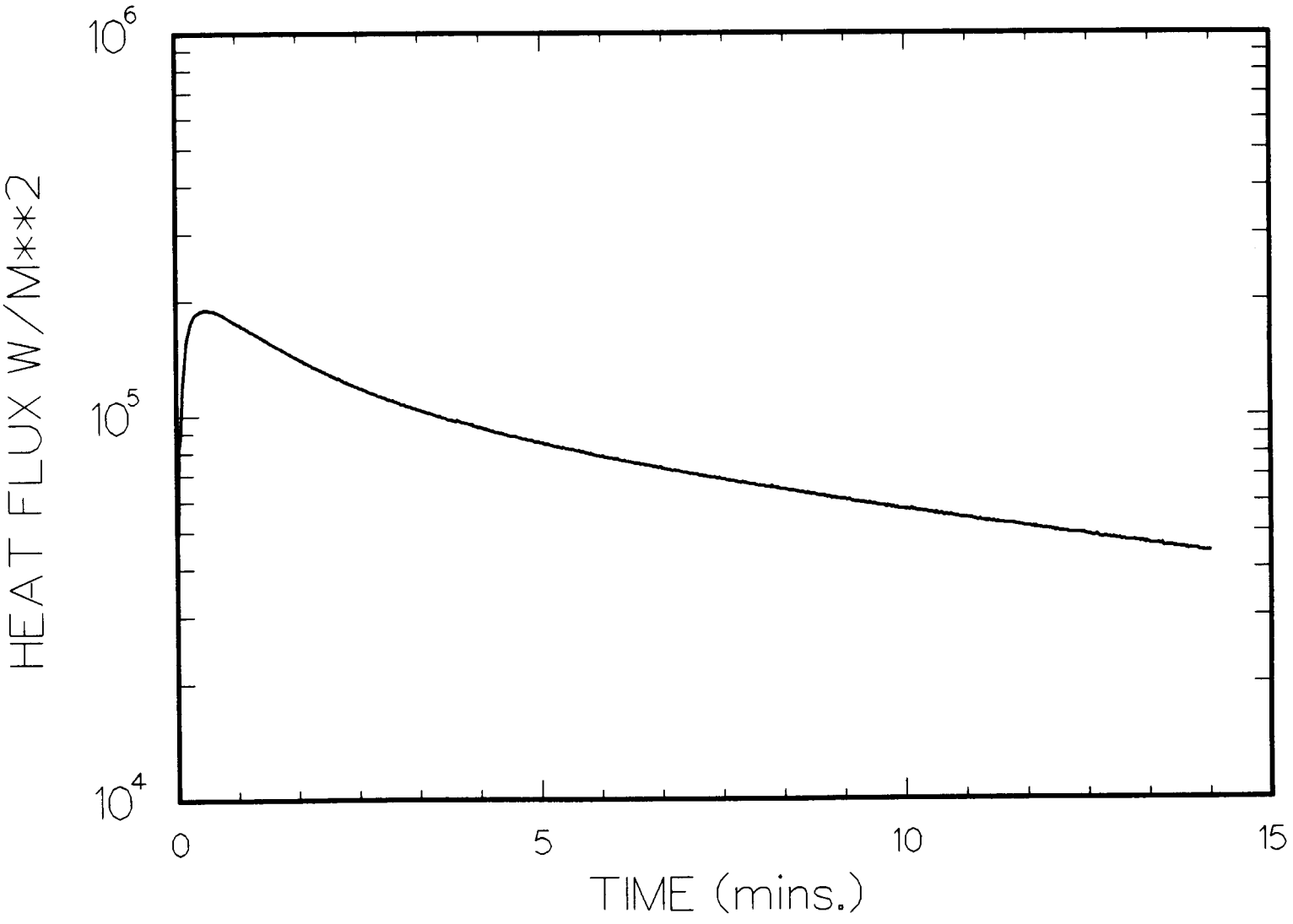

Figure 3.9. TURC2 MgO Sidewall Heat Flux at 7 cm Above the Melt-Concrete Interface

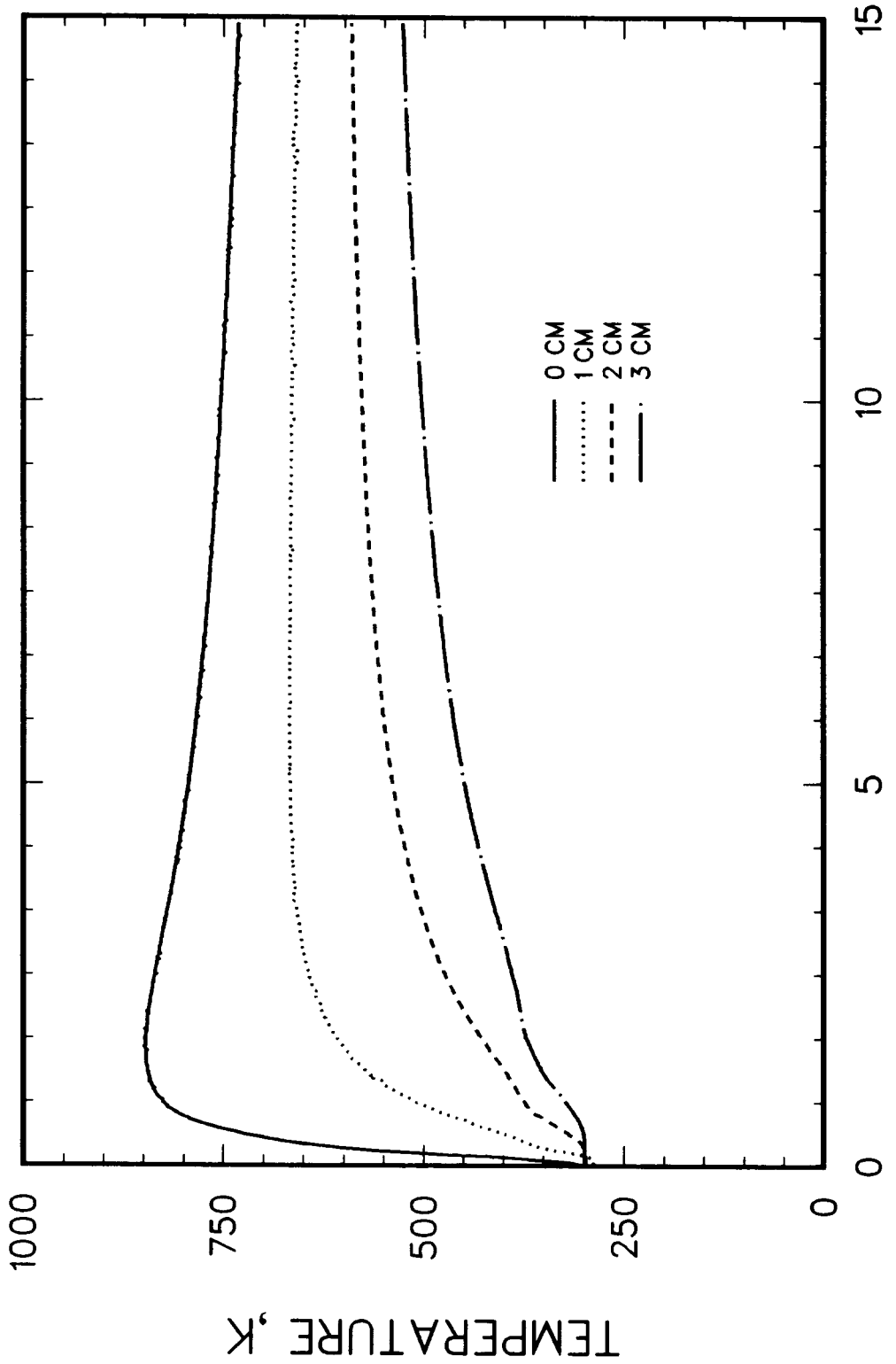

Figure 3.10. MgO Wall Thermocouple Data at 2 cm Above Melt-Concrete Interface

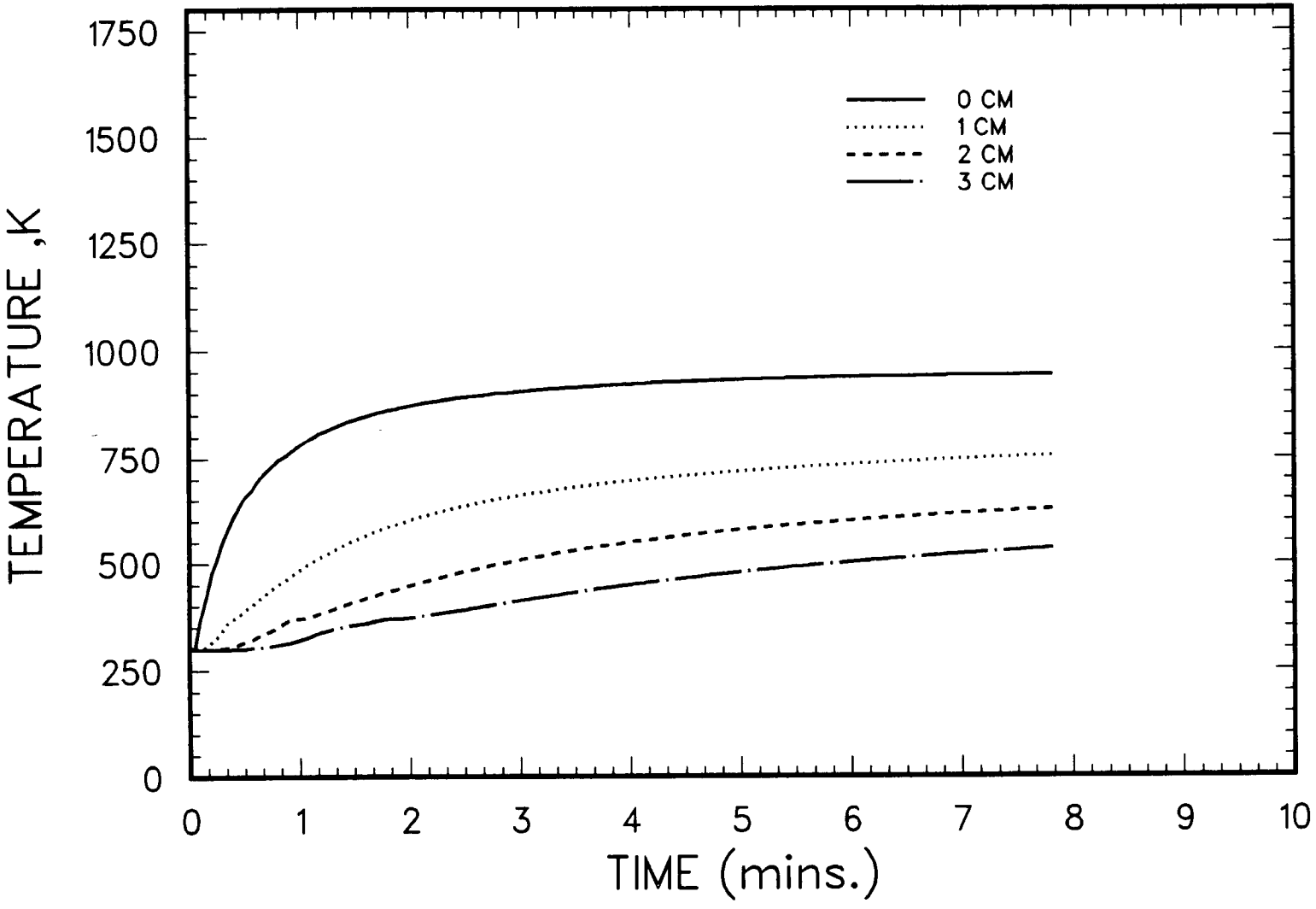

Figure 3.11. MgO Wall Thermocouple Data at 7 cm Above Melt-Concrete Interface

The upper heat flux from the melt pool surface was measured by a heat flux gauge discussed in Section 2.4. As with the MgO sidewall, IHCP[16] was employed to calculate the heat flux based on embedded thermocouples within a mild steel plug mounted in the portcullis. The thermocouple data is shown in Figure 3.12. The results of the calculation are shown in Figure 3.13. This heat flux is a result of radiative and convective heat transfer within the upper plenum of the crucible. Due to the geometry of the thermal system, a shape factor correction is necessary to obtain the actual melt pool radiative heat flux. Utilizing the shape factor for parallel circular disks by Siegel and Howell,[17] a correction factor of 100 is required for the radiative component. Since the radiative component dominates the upper heat flux it is suggested that the correction factor be applied to the data in Figure 3.10 in order to obtain the surface heat flux.

3.2.1.3 TURC2 Gas Composition

As described in Section 2.4.2, discrete grab gas samples of evolving gases were taken throughout the test. The gas samples were analyzed for H_2, N_2, O_2, Ar, CO, CO_2, and CH_4. The composition of the gases sampled are listed in Table 3.1. The reported time of each sample is referenced to initial contact of melt with concrete. After the teem was complete, the sliding portcullis was closed (time ~10 sec). Reaction products from the melt-concrete interaction were then vented out the crucible exit port, past the gas sample port (see Figure 2.1).

Gas samples 1-3 were taken prior to closure of the portcullis. These samples were of the interaction chamber gases which consisted of air and Ar. (The Ar gas was injected into the interaction chamber when the lower furnace valve was opened to permit the teeming of the melt.)

Past melt-concrete experiments[2,3,4,5], utilized grab samples similar to those used in these experiments and have shown the determined compositions to be consistent with equilibrium gas mixtures at temperatures ranging from 1000-1100 K. At the location of the gas sampling the gas temperature was ~500 K, as shown in Figure 3.14. Thus the gases had been quenched within the MgO crucible. Thermodynamic calculations would be required to assess the composition at the sample temperatures. Unfortunately, measurements of water vapor content within the sampled gas were unsuccessful; therefore, quantitative equilibrium calculations are not possible.

It is apparent from the gas composition that water vapor and CO_2 released from the decomposing concrete were reduced to combustible H_2 and CO. Shown in Figure 3.15 is the molar ratio of

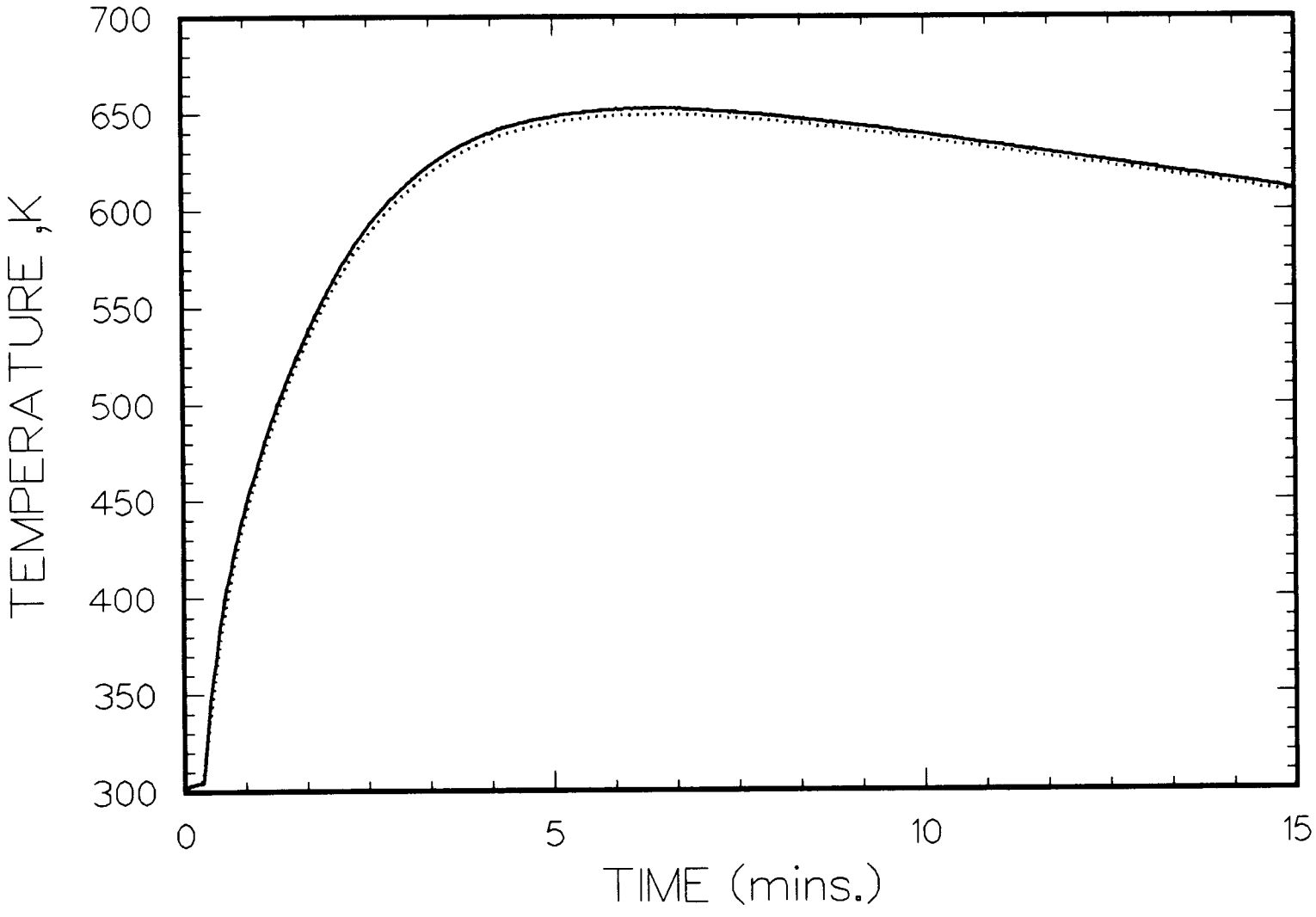

Figure 3.12. Thermocouple Data from Heat Flux Gauge Located in Portcullis

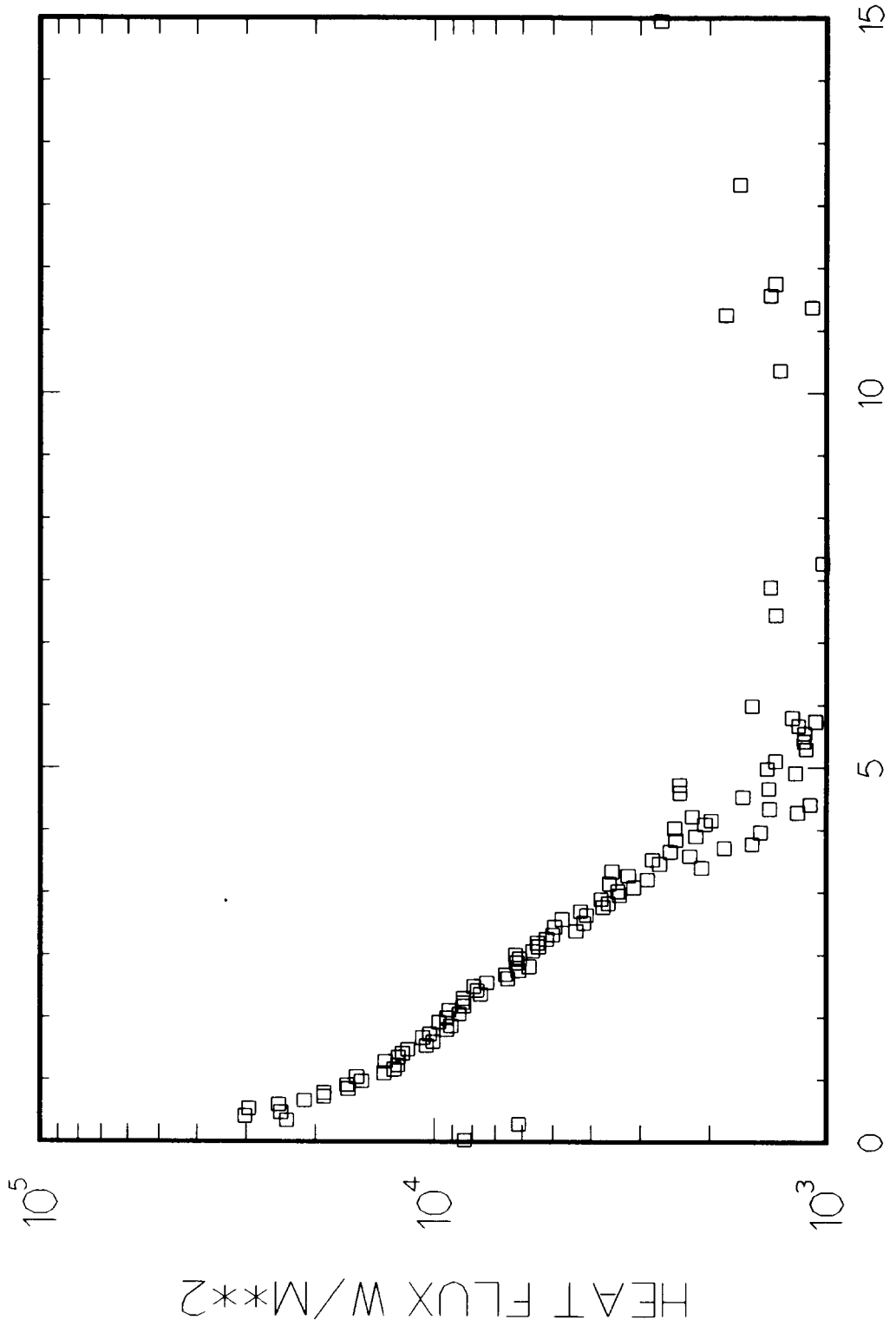

Figure 3.13. TURC2 Melt Pool Upward Heat Flux at the Portcullis

Table 3.1

TURC2 Gas Sample Compositions

Volume Fraction of Individual Gas Species (%)

Time	H_2	N_2	O_2	AR	CO	CO_2
-60.	0.0000	0.7730	0.2040	0.0227	0.0000	0.0000
6.	0.0000	0.7384	0.1970	0.0646	0.0000	0.0000
10.	0.0000	0.7340	0.1960	0.0210	0.0276	0.0290
15.	0.2340	0.4186	0.0393	0.0946	0.1667	0.0465
20.	0.4315	0.0920	0.0077	0.0000	0.3376	0.1311
25.	0.4497	0.1139	0.0078	0.0508	0.2608	0.1169
30.	0.4610	0.1050	0.0083	0.0000	0.3020	0.1240
35.	0.4165	0.1110	0.0085	0.1370	0.2200	0.1070
40.	0.3980	0.0890	0.0073	0.2020	0.1970	0.1060
45.	0.3980	0.0820	0.0061	0.2590	0.1570	0.0976
50.	0.3395	0.0680	0.0054	0.3420	0.1448	0.1000
55.	0.3097	0.0585	0.0046	0.3914	0.1380	0.0970
58.	0.2918	0.0898	0.0069	0.4136	0.1120	0.0857
60.	0.2790	0.0918	0.0073	0.4310	0.1090	0.0820
70.	0.2610	0.0970	0.0080	0.4520	0.1010	0.0810
90.	0.2230	0.0973	0.0077	0.5070	0.0880	0.0770
120.	0.2190	0.0610	0.0056	0.5750	0.0650	0.0740
150.	0.1875	0.1134	0.0094	0.5420	0.0720	0.0750
180.	0.1879	0.0220	0.0000	0.6910	0.0550	0.0439
210.	0.1697	0.0650	0.0110	0.6200	0.0530	0.0800
240.	0.1697	0.0505	0.0079	0.6395	0.0498	0.0826
270.	0.1660	0.0450	0.0051	0.6450	0.0560	0.0837
300.	0.0860	0.0680	0.0069	0.7170	0.0400	0.0810
390.	0.0830	0.3680	0.0230	0.4400	0.0300	0.0560
450.	0.0000	0.8770	0.0830	0.0355	0.0000	0.0000

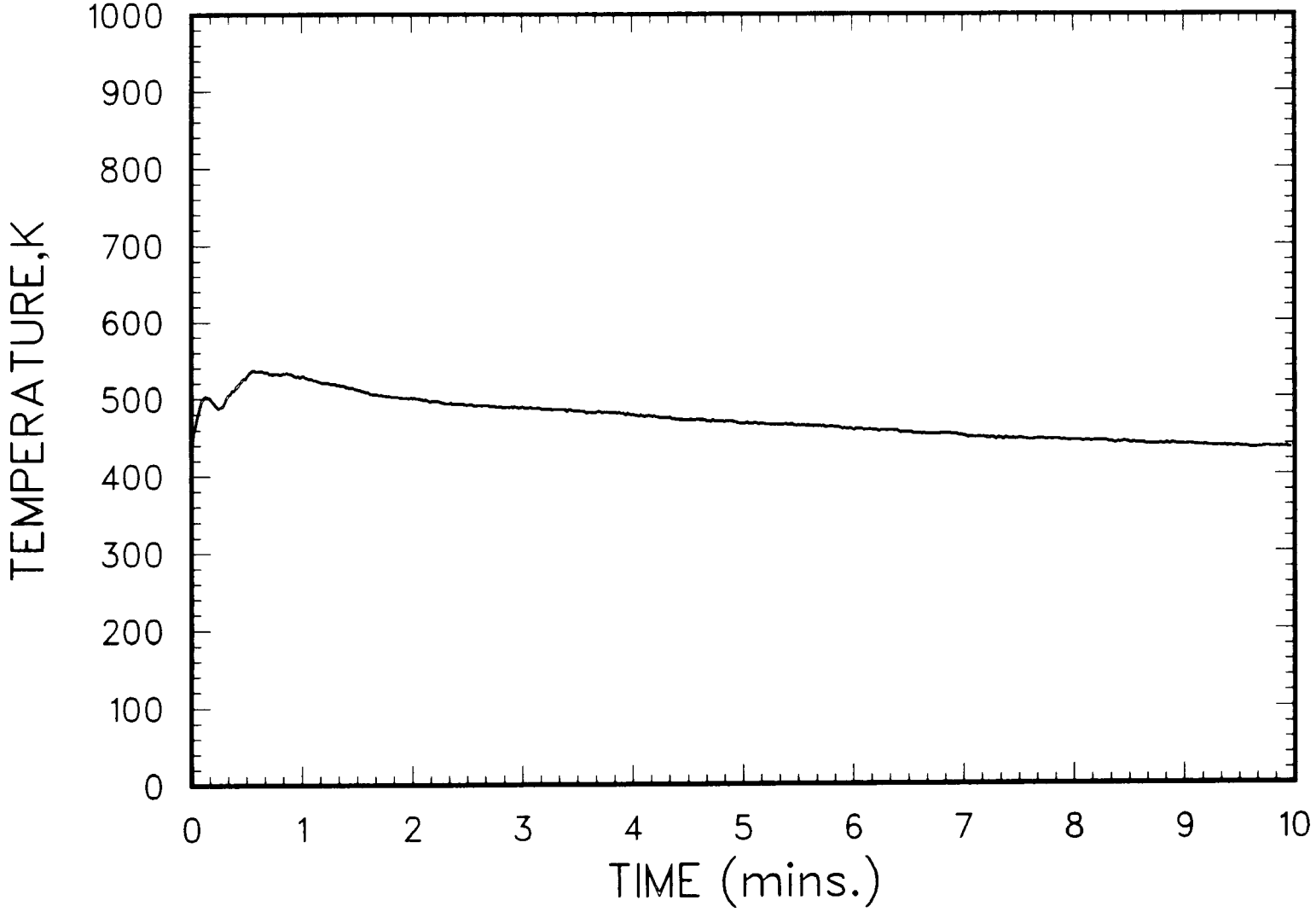

Figure 3.14. TURC2: Temperature of Sampled Gases

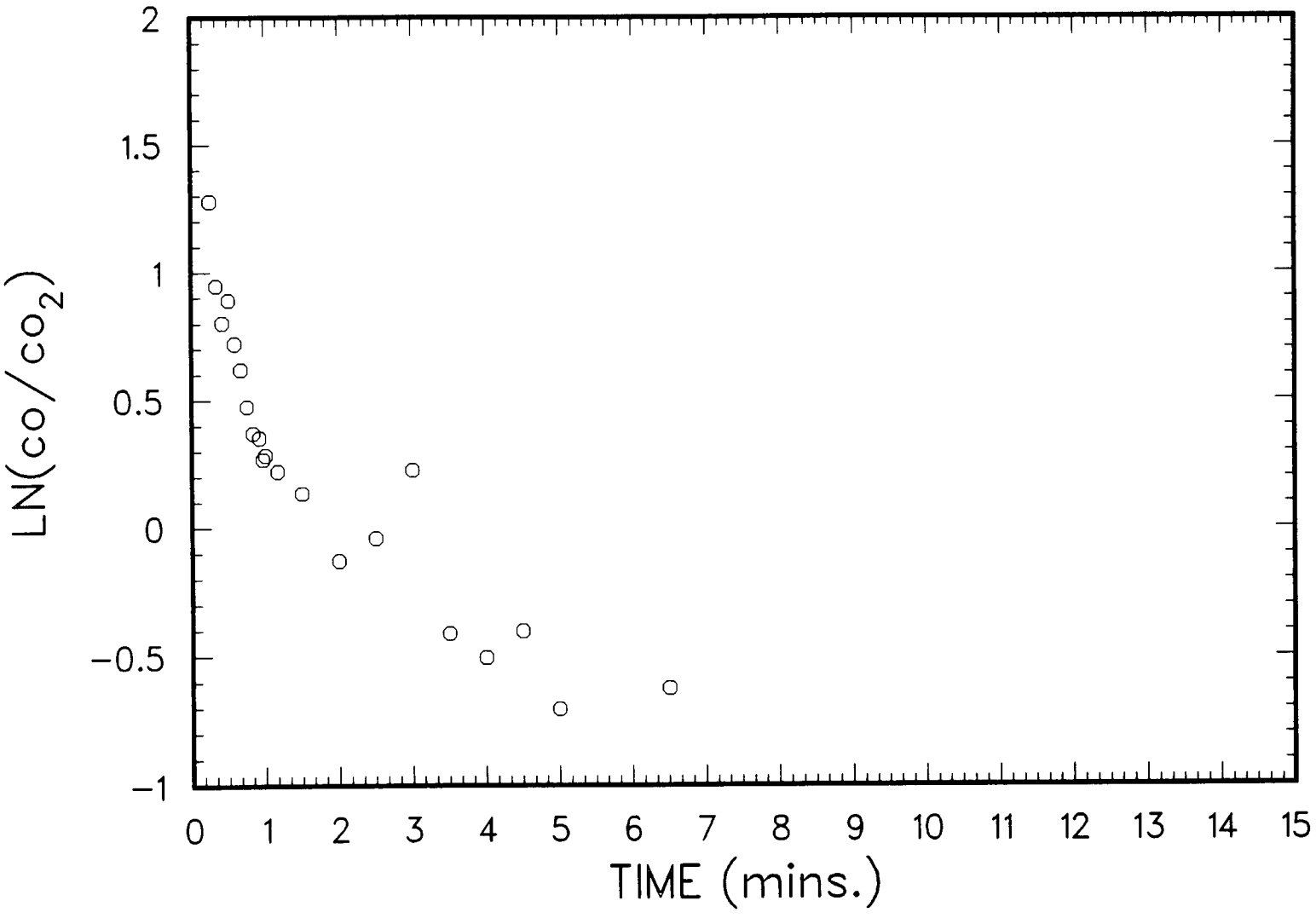

Figure 3.15. TURC2: Logarithm of Mole Ratio of CO to CO_2

CO to CO_2 at various times during the experiment. It is clear from this data that for very early times considerable reduction of CO_2 to CO took place. However, within the first minute of the experiment, there was a rapid decrease in the reduction of CO_2.

Reduction of CO_2 to CO is a function of the chemical and physical environment of the gases. Assuming no other environmental changes, the temperature of the chemical system is a principal

factor in the reduction of CO_2. In light of the rapid decrease in the CO/CO_2 ratio, one might assume the melt pool temperature responsible, if the gases released from the concrete were to pass through the melt pool. The above argument would, therefore, require a rapid decrease in the melt pool temperature. As will be presented in Section 4.1, other physical evidence and analyses suggest this not to be the case. Thus, other alternatives are for the gases to bypass the melt pool, most likely along the MgO sidewall or through frozen channels within the pool. The posttest X-rays, disassembly of the melt pool and the MgO sidewall heat flux data seem to support these possibilities.

Gas flowrates were inferred from the gas composition data by examining the mass fraction of the argon constituent. As discussed in Section 2.4.2, argon gas was injected into the interaction crucible. The argon flowrate was continuously monitored throughout the experiment. By examining the mass fraction of argon present in the individual gas samples (coupled with the measured argon flowrate) the total mass flowrate within the experiment was calculated. The injection of argon gas was delayed until after approximately 30 seconds from the initiation of the melt teem, therefore the calculated flowrates are only available from 35 to 300 sec.

Shown in Figure 3.16 are the flowrates as determined from the gas composition and argon injection. As would be expected for the benign transient melt-concrete observed, the flowrate is relatively low. In fact, most of the total flow is from the Ar injection flowrate.

Using the same technique described above, the gaseous carbon mass flowrate was calculated. The carbon mass flowrate is the total carbon from CO_2 and CO released during the melt-concrete interaction. These data are useful when compared to analytical models of CO_2 released from concrete during melt-concrete interaction. The data is shown in Figure 3.17. Further discussion of this point is presented in Section 4.1.

3.2.1.4 Aerosol Data for TURC2

Upon retrieval and disassembly of the aerosol sampling instruments from the TURC2 test, the following observations were made.

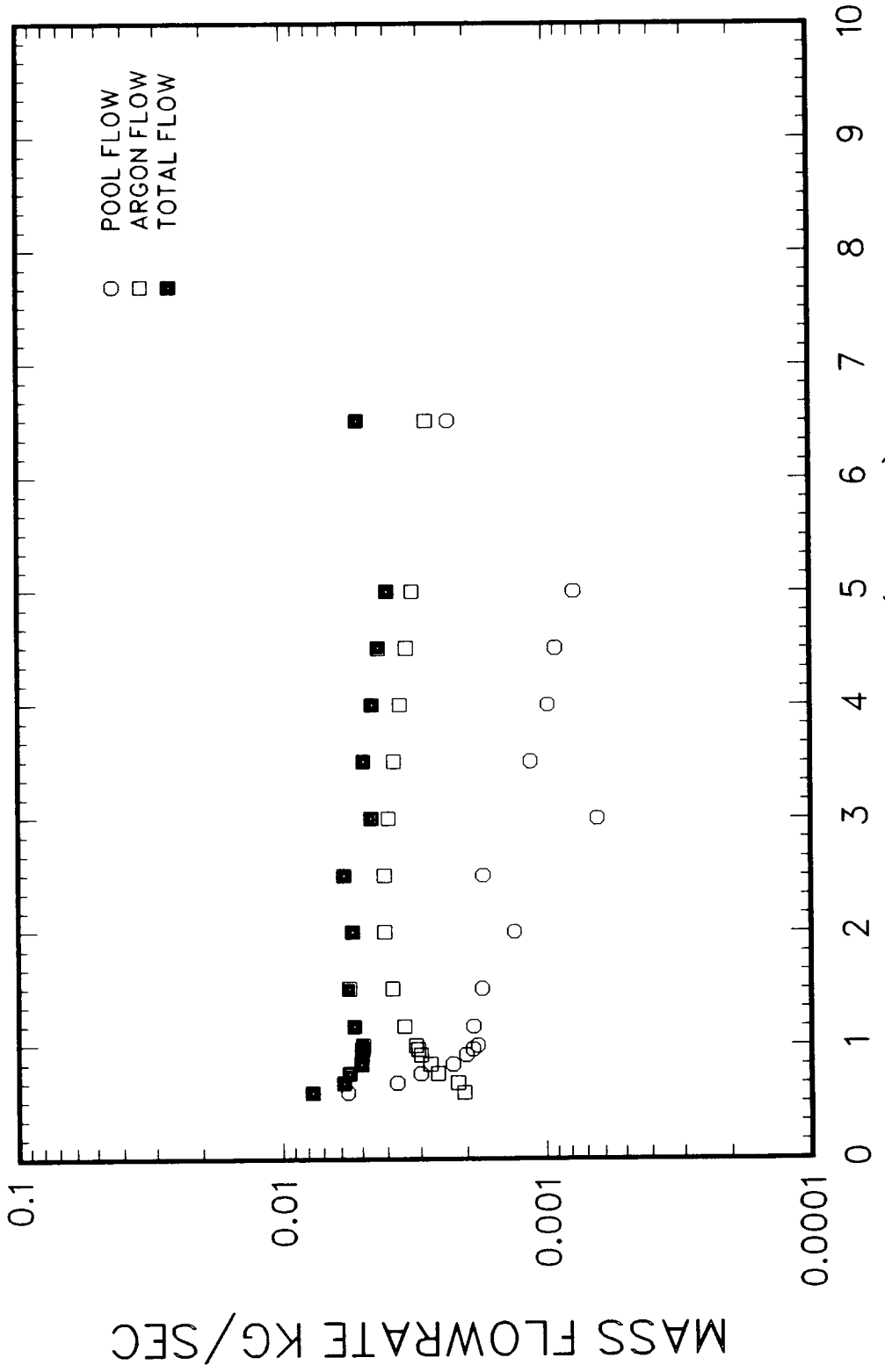

Figure 3.16. TURC2 Gas Flowrates

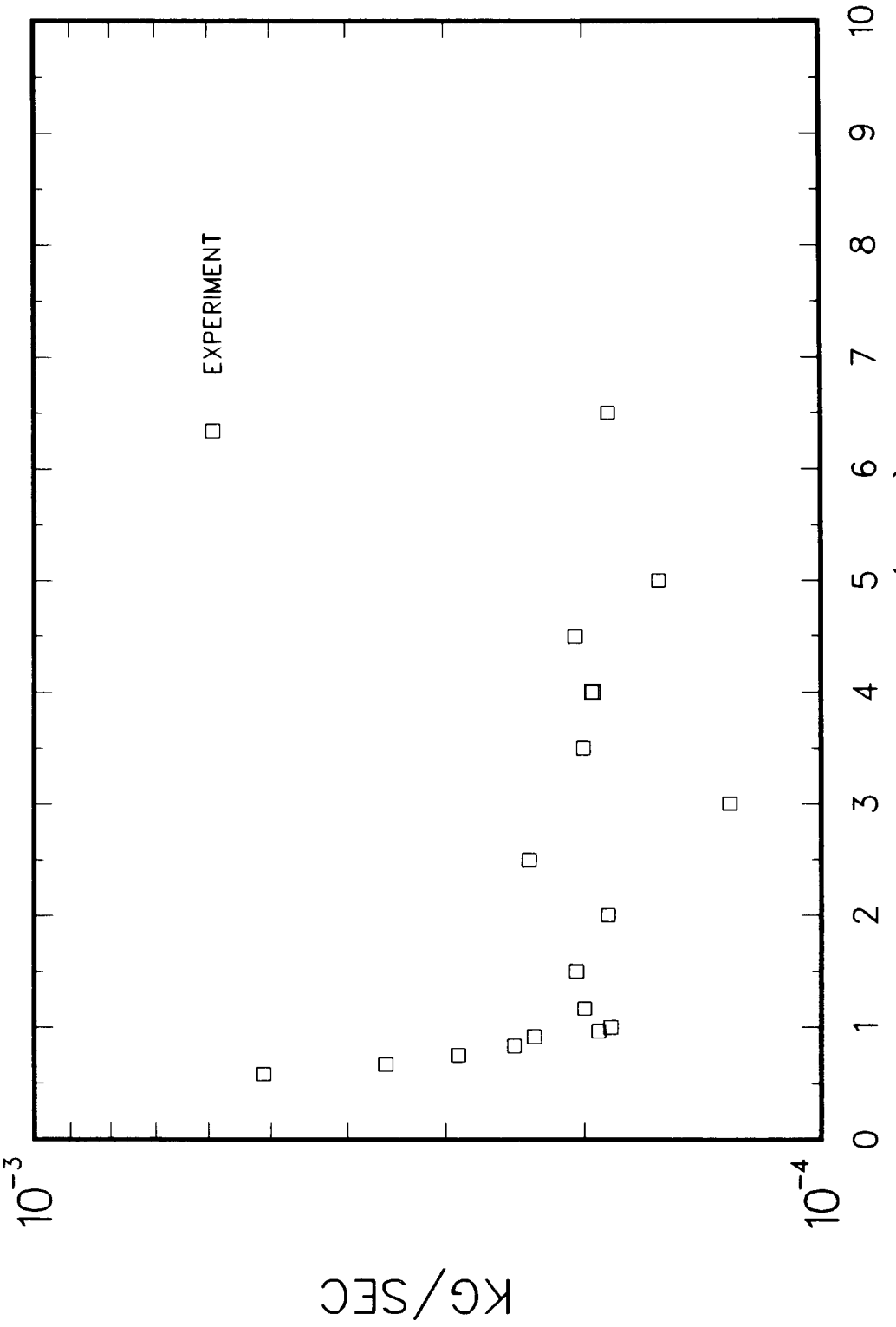

Figure 3.17. TURC2 Carbon Mass Flow

(1) The view windows of the opacity monitor were found to be coated with dark grey aerosols of sufficient amount to block the light. No useful data were obtained from the output of this instrument.

(2) The impactor samples exhibited overloading of the stages collecting at about 1 μm aerodynamic equivalent diameter (stages 5, 6, and 7) in some (1, 2, 3, 4, 5, and 6) of the samples.

(3) The aerosol collected by the impactors and the filters was dark, almost black in appearance.

Filter Data: The filter samples gave the aerosol concentrations at the point where the exhaust line entered the top of the gravel bed filter and in the interaction chamber at selected times. The aerosol concentration and sample times are given in Table 3.2. The zero time is taken as the time of portcullis closure, 10 seconds after the start of the teem. The concentrations and sample flow rates are given at STP. The aerosol samples taken from the exhaust line were preceded by a preseparator which effectively removed particles larger than about 10 μm aerodynamic equivalent diameter.

Opacity Monitor: The reading went to 100% opacity and remained there during and after the test. The windows were coated with dark grey aerosol. It was later determined that the purge gas flow designed to keep the windows clean had not been established early enough to be effective.

Impactor Samples: Impactor samples were taken from the top of the gravel bed filter where the exhaust line entered. Although they were overloaded they provided aerosol size distribution information. Overloading of a stage occurs when more than 15 mg of material is collected on that stage or when the deposits on a stage appear heavy enough to influence impaction. Overloading did not begin to occur until the size of particles being collected dropped below 1 μm aerodynamic equivalent diameter, i.e., stages 5, 6, and 7. This indicates that the aerosol had a mass mean aerodynamic diameter on the order of 1 μm.

Impactors 7 and 8 were run from 5 to 6 minutes after portcullis closure. No gas flow data was taken after 300 seconds and the pool flows are not known. At low pool flow rates, the argon purge might only carry off residual aerosols from the crucible cavity region. Data from these samples may be characteristic of the residual aerosol from late in the test and not representative of an active aerosol source.

Impactor 1 was not severely overloaded and yielded the size distribution shown in Figure 3.18. This distribution appears unimodal with the mass mean aerodynamic diameter located between 1 and 2 μm and a geometric standard deviation of about 2.0. This

Table 3.2

Aerosol Filter Data for TURC2

Sample	Sample Time* (sec)	Collected Mass (mg)	Sample Flow Rate (SLPM)	Aerosol Concentration at STP (g/m^3)
Exhaust Line				
A	0-10**+	41.4	4.0	62.1
B	10-20	42.2	4.4	57.5
C	20-40+	43.8	5.1	25.8
D	40-60+	52.7	4.3	36.8
E	60-120**+	84.1	4.0	21.0
F	120-180	36.3	3.9	9.3
G	180-240	11.1	3.8	2.9
H	300-360	3.3	3.6	0.9
I	420-480	2.5	4.4	0.57
J	540-600	2.2	4.0	0.55
Interaction Chamber (2 locations)				
	0-20	11.05	2.0	16.6
	0-20	6.15	2.0	9.2

*Time after portcullis closure

**Analyzed by XRF

+Analyzed by PIXE

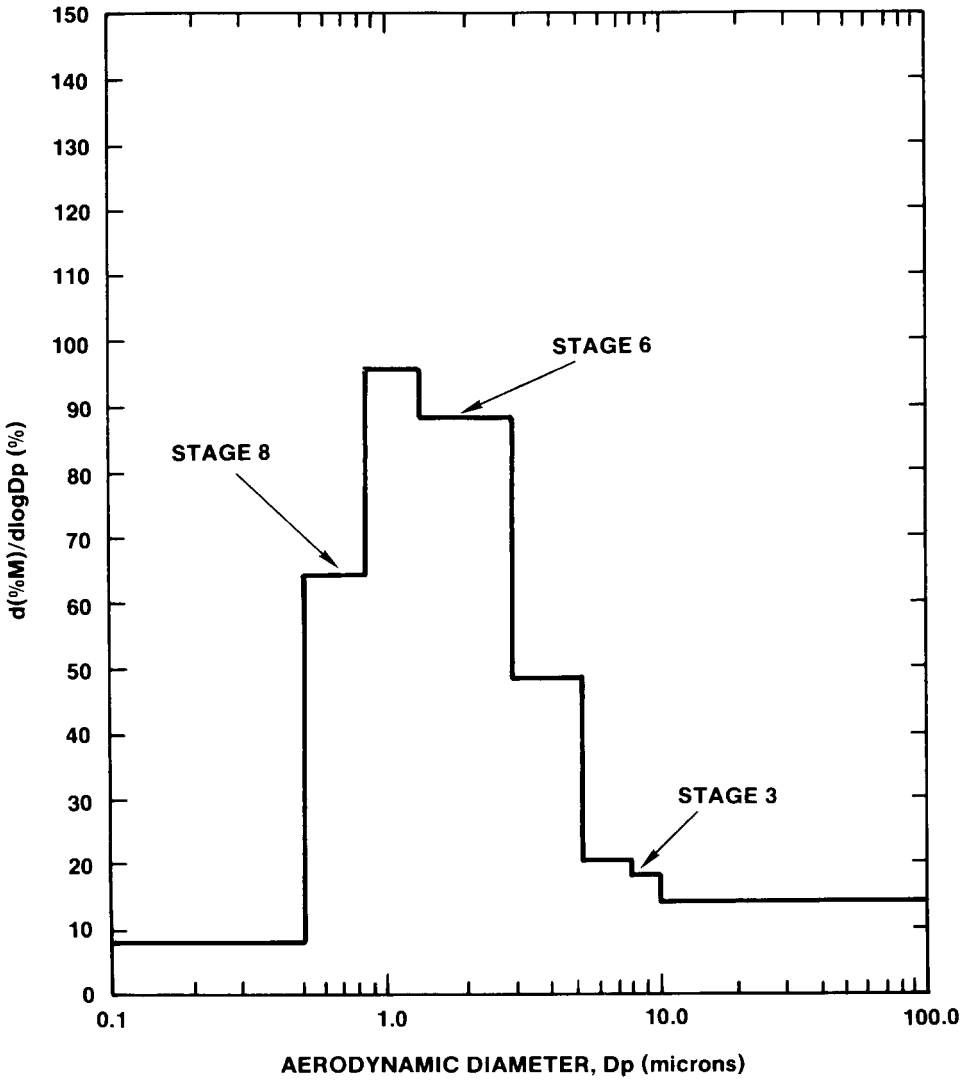

Figure 3.18. Measured Aerosol Size Distribution from TURC2 Impactor

sample was taken from 0 to 10 seconds after portcullis closure. The sections of the distribution corresponding to stages 3, 6, and 8 in the impactor are indicated. Figure 3.19 contains electronmicrographs of the aerosol collected on these impactor stages.

Table 3.3 contains the gross impactor data for the impactors run on the TURC2 tests. Sample time, mass collected, flowrate, and aerosol concentration are given also.

Cyclone Sample: No analysis has been performed on the cyclone sample. Such analysis will not yield detailed distribution information because the sample was taken over the duration of the test. This effectively integrates the distribution over time with an unknown weighting function. The purpose of this sample was to collect bulk aerosol material for chemical analysis. This analysis has not been performed to date.

Chemical Analysis: As discussed in Section 2.0 nonradioactive dopants representing fission products were placed in the melt generator and the interaction crucible. Table 2.2 lists the dopants and their location.

X-ray Fluorescence (XRF) elemental analysis has been performed for two selected filter samples from TURC2 (sample A; 0 to 10 sec and sample E; 60 to 120 sec: see Table 3.2). Table 3.4 contains the results of this analysis for the elements analyzed. A number of elements were analyzed qualitatively, while quantitative analysis was performed for Mo, Te, and U. Detectability limits influence and may hinder detection so that failure to detect a given element does not exclude its presence.

Proton induced X-ray-emission (PIXE) has also been performed on selected aerosol filter samples from TURC2. They are A (0-10 seconds), C (20-40 seconds), D (40-60 seconds), and E (60-120 seconds). The results from the PIXE analysis, although qualitative, concur with the XRF results. Tungsten, an element not analyzed for in XRF, was seen to form a major component of the aerosol sampled from the TURC2 test. Tungsten rods from the ring support structure were found in the melt at the melt/concrete interface. The oxidizing gases could have reacted with the tungsten causing the tungsten release.

3.2.1.5 TURC2 Posttest Melt Pool Composition and Melting Point

Several samples of the melt pool debris were removed for elemental composition analyses by X-ray fluorescence (XRF). The XRF analysis was qualitative in nature and was performed to examine gross compositional changes in the melt pool debris. Table 3.5 is a summary of the XRF analysis for TURC2 debris. Analysis of pretest TURC3 material was included to provide a comparison with original bulk debris material. Note the TURC2 and TURC3 debris were identical materials with the exception of

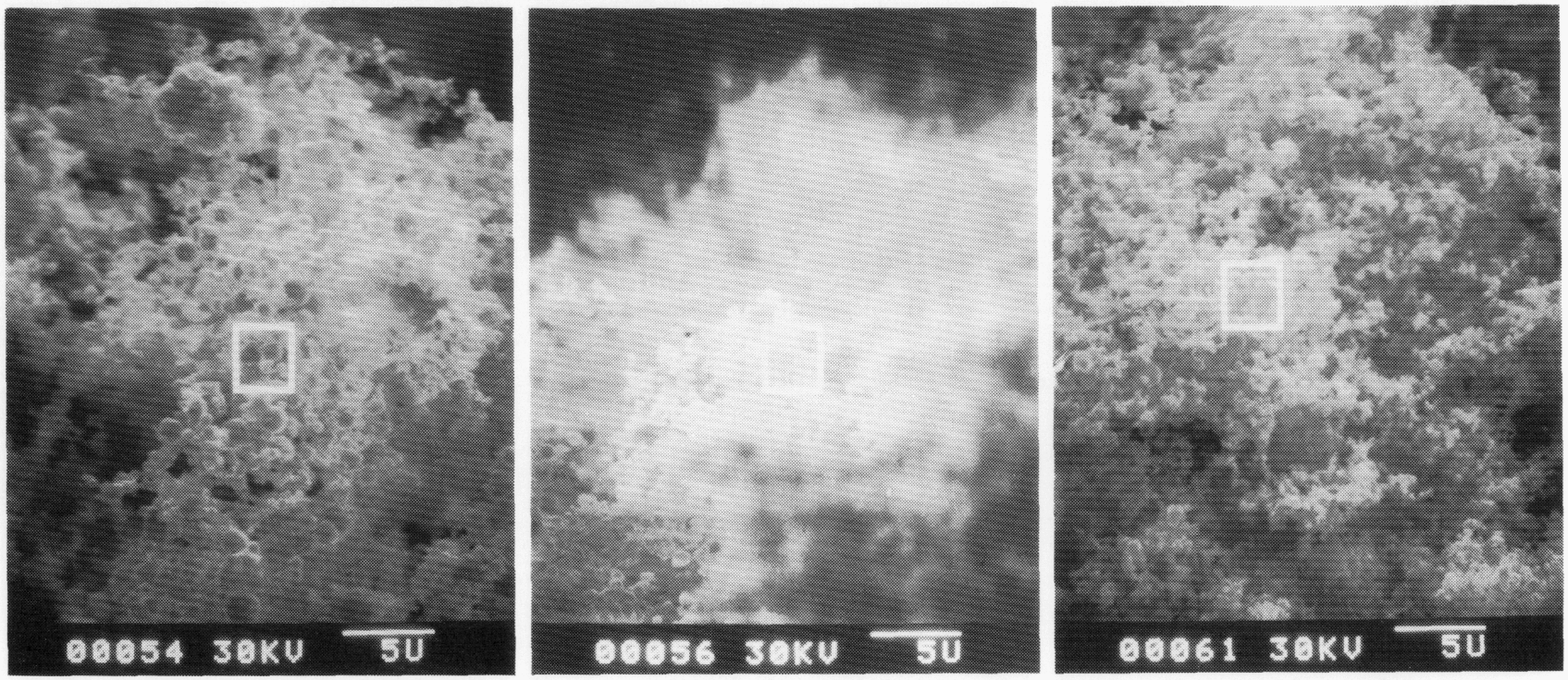

Figure 3.19. Electron Micrographs of TURC2 Aerosol from Impactor 1, Stages 3, 6, and 8

Table 3.3

Aerosol Impactor Data for TURC2

Sample Time* (sec)	Impactor (-)	Collected Mass (mg)	Sample Flow Rate (SLPM)	Combined Aerosol Concentration (g/m^3)
0-10	1	50	7.7	52.
0-10	2	113	11.1	
20-40	3	57	9.5	16.6
20-40	4	70	13.5	
60-120	5	191	10.6	20.
60-120	6	173	7.6	
300-600	7	5.0	8.1	0.6
300-600	8	7.9	12.3	

*Time after portcullis closure

Table 3.4

XRF Analysis of TURC2 Aerosol Filter Samples

	Qualitative Analysis Sample		Quantitative Analysis Sample	
Element	Filter A (0 to 10 s)	Filter E (60 to 120s)	Filter A (0 to 10 s)	Filter E (60 to 120 s)
Si	T	T		
Fe	T	T		
Mo	T	S	1.69 w/o	6.53 w/o
Cs	T	-		
Ce	T	T		
Ca	T	T		
Ni	S	S		
Te	M	M	8.06 w/o	7.26 w/o
Ba	T	T		
Mn	T	T		
Zr	T	T		
I	S	-		
La	-	-		
U	S	S	2.5 w/o	4.93 w/o

Levels: M = Major Constituent
S = Minor Constituent
T = Trace
- = Uncertain

Table 3.5

TURC2 X-Ray Fluorescence Qualitative Composition Analysis

Element	Pretest* Material	Posttest TURC2 Melt-Concrete Interface	Posttest TURC2 Side Wall Melt Interior
U	M	M	M
Ti	-	-	-
Mn	-	-	-
Fe	-	S	S
Zr	M	M	M
I	-	-	-
Cs	-	-	-
Al	-	-	-
Si	-	S	-
Ca	-	S	S
Ba	-	-	-
K	-	-	-
Mo	-	-	-
W	-	-	-

NOTE: M: Major Component
S: Small Component
T: Trace Component
-: Not Detected

*$UO_2/ZrO_2/Zr$ material, no fission product mocks

the added Zr metal (9 w/o) in TURC3. Note also that no fission product mock materials were added to the pretest material that was analyzed by XRF.

As shown by the qualitative XRF analysis, the posttest debris contains small quantities of Fe, Si, and Ca. These elements were most likely introduced by the decomposition of concrete. The mechanism of entrainment of these species within the melt debris has not been established.

Summarized in Table 3.6 are the pretest and posttest melting temperatures of the melt pool debris. The melting temperatures were determined by the cone slump method and represent bulk values.

A comparison of the data shows a significant drop in the melting temperature of the posttest debris. This is most probably due to the presence of SiO_2, CaO, and FeO within the debris.

Although a phase diagram for this complex system does not exist, Lang et al.[18] and Alberman, et al.[19] report significant reduction in the melting point of UO_2-SiO_2 and UO_2-CaO binary mixtures for even small quantities of SiO_2 and CaO.

3.2.2 TURC3

As discussed in Section 3.1.2, during the melting phase of the TURC3 experiment the external thermocouples indicated a breach of the melt crucible within the LMF furnace. Posttest examination of the LMF furnace cavity confirm furnace diagnostics. A large hole (~8 cm in diameter) located on the side wall of the crucible enabled approximately 120 Kg of UO_2 laden melt to pour onto internal furnace structures. The crucible failure appeared to be caused by a tungsten ring which shifted from its original position and melted through the crucible sidewall. It was also apparent that the flowing molten debris enlarged the original breach. Damage to the LMF furnace was minimal due to several design features within the furnace (i.e., water cooled copper core catches on the furnace bottom plate). The remainder of the melt was either teemed into the interaction crucible or remained within the melt generator crucible as slag.

3.2.2.1 Posttest Observations

The day after the completion of the TURC3 experiment, the crucible was removed from the interaction chamber for posttest analysis.

X-rays of the lower section of the crucible were taken. A representative X-ray of the crucible is shown in Figure 3.20. The X-ray shows a melt pool approximately 7.8 cm thick. The melt pool appears to be in contact with the concrete base. A gap

Table 3.6

TURC2 Melt Pool Melting Point

Material Description	Melting Point[+]
TURC2 Original Material*	2657 • 10 K
TURC2 Melt Pool Center	2396 ± 10 K
TURC2 Melt-Concrete Interface	2355 • 10 K
TURC2 Sidewall Melt Pool Interior	2275 ± 10 K

*UO_2 (70 w/o), ZrO_2 (30 w/o), no fission product mocks

[+]Note: Errors indicate temperature measurement errors only, not melt point uncertainty.

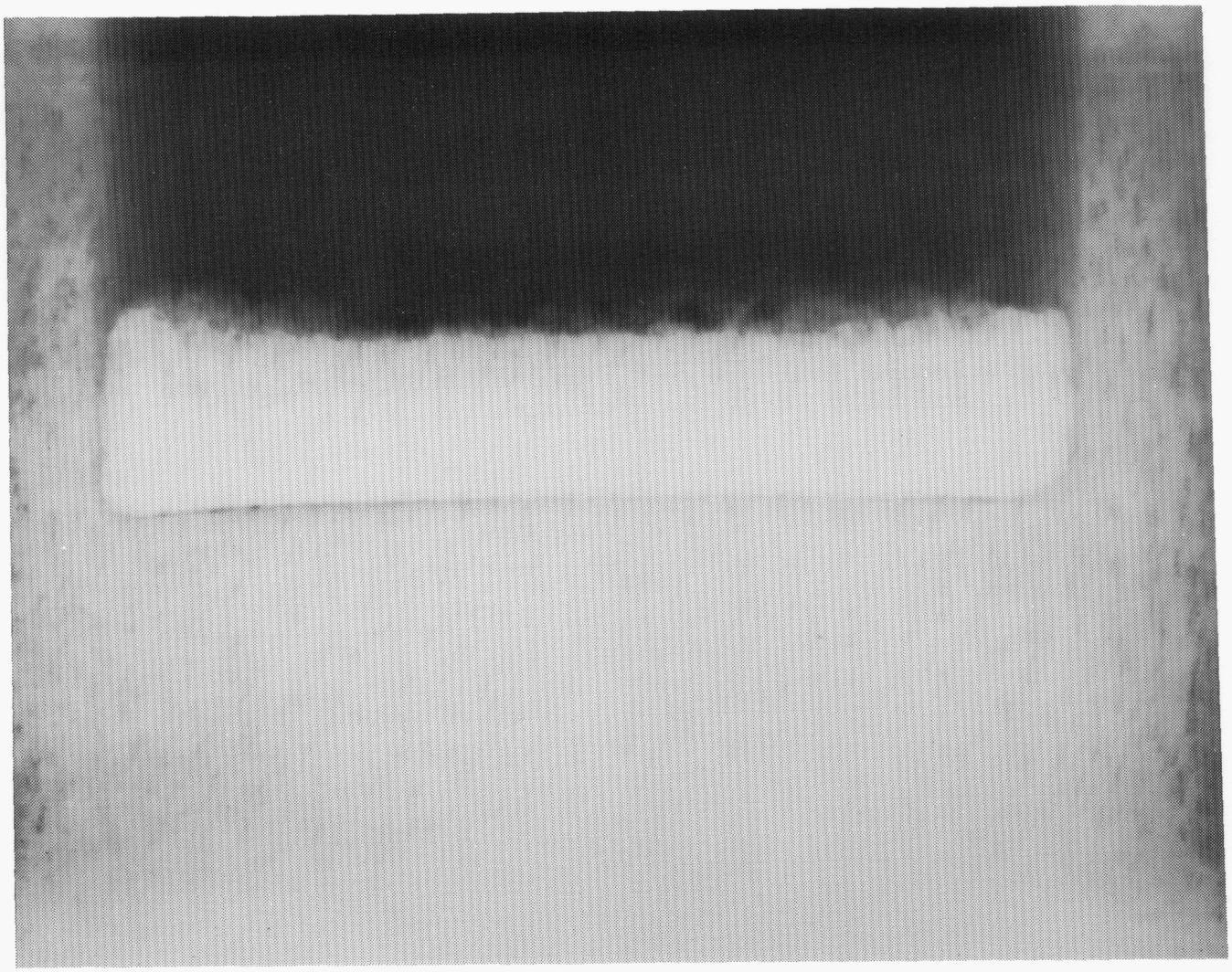

Figure 3.20. TURC3 Posttest X-Ray

along the MgO sidewall is apparent. No evidence of degradation of the MgO sidewall was observed from the X-ray.

The external crucible instrumentation and portcullis were removed to gain access to the interior of the crucible. The melt top surface, shown in Figure 3.21 was convoluted and cracked. Depositions of 1 to 3 mm spheres or droplets were uniformly distributed over the pool surface. The crucible interior sidewall was uniformly covered with a deposit of a fine particulate. Additionally, irregular shaped particles ~ 0.5 to 2 mm were found adhered to the wall.

Following the preliminary inspection, the crucible was sectioned along its vertical length. A 120° section was removed, revealing the interior crucible cavity, melt pool, and concrete slug.

Shown in Figure 3.22 is a close-up photograph of the melt pool outer diameter (vertical) surface and the melt-concrete interface. The melt pool is porous, with numerous channels running from the melt-concrete interface to the top surface. Also apparent are small (<1 mm) diameter metallic appearing spheres uniformly dispersed throughout the surface.

Due to the relatively small mass of the melt pool (46.45 Kg) the melt pool was removed nearly intact. As shown in Figure 3.23, the bottom of the melt pool consisted of a area from the center to approximately 15 cm out on the radius which apparently was in contact with the concrete. This region was white in color, relatively flat, with a rough granular texture. The remaining portion of the melt pool surface (15 to 20 cm on the radius) was significantly different, in that a thick deposit of a green colored powder material was found. X-ray fluorescence (XRF) analysis of this material showed major quantities of Cs and I, a small quantity of Mn and a trace amount of U. The XRF analysis was qualitative and indicated only elemental composition. It is important to note that fission product mocks of Cs, I and Mn were uniformly placed on the concrete surface prior to melt teeming.

Samples of the molten pool material from several representative locations were removed for analysis. The melt temperature and XRF elemental analysis of the debris material are summarized in Section 3.2.2.5.

As shown in Figure 3.23, the melt pool was sectioned revealing the internal structure. The pool was not as dense a structure as was the TURC2 pool. Numerous voids were uniformly dispersed throughout the vertical axis of the melt. The voids diameters ranged from a millimeter to a centimeter in diameter. The portion of the melt pool in contact with the concrete contained mostly the smaller diameter voids (~1 mm) and was representative of a foam-like material in some locations.

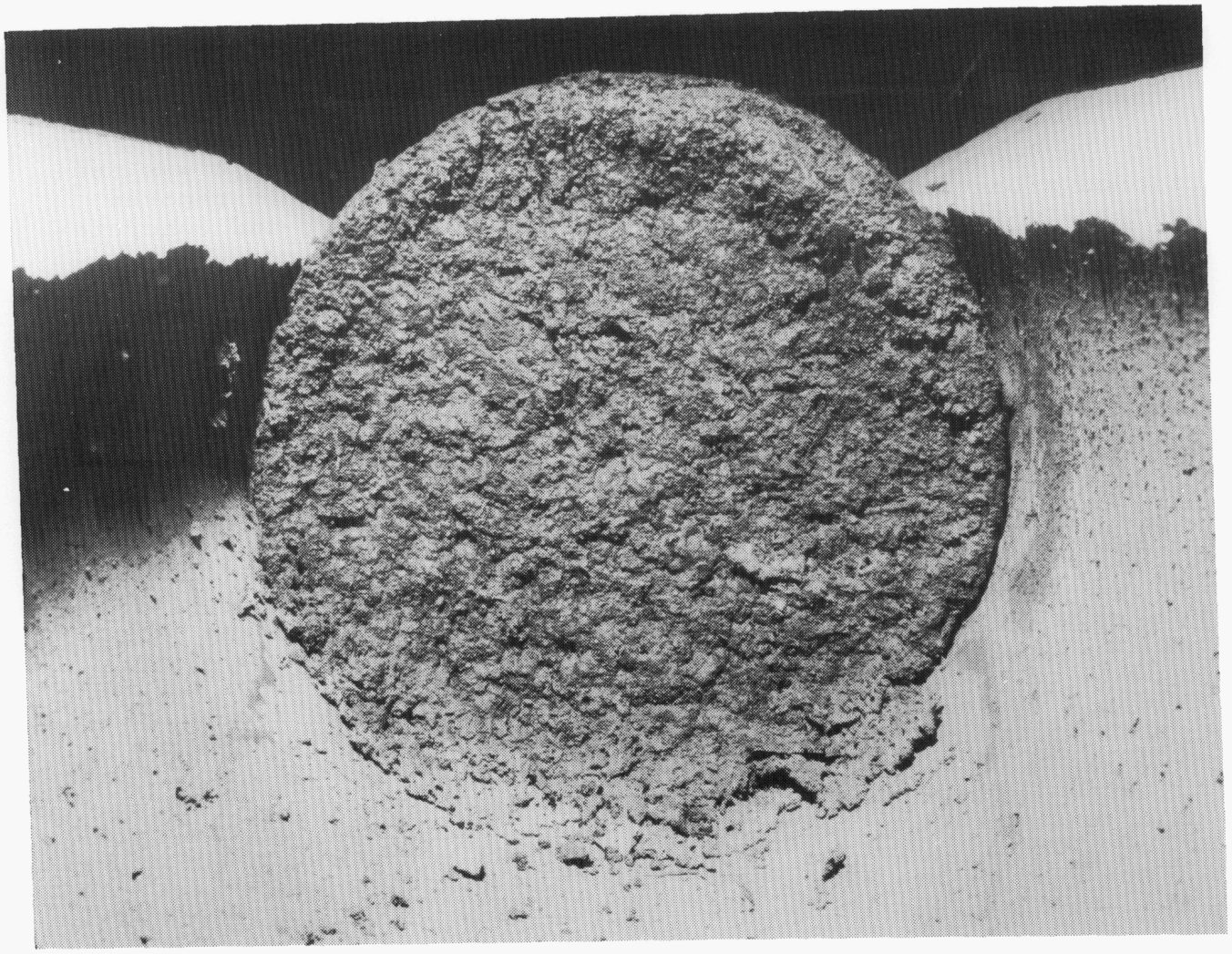

Figure 3.21. TURC3 Melt Pool Top Surface

Figure 3.22. TURC3 Concrete Slug and Melt Pool

Figure 3.23. Sectioned TURC3 Melt Pool

Unlike the TURC2, no tungsten components were found within the debris pool. As with the TURC2 experiment, little or no attack of the MgO sidewall by the melt pool was found.

3.2.2.2 TURC3 Concrete Erosion and Crucible Thermal Response

The temperature history measured by thermocouple embedded at various depths within the concrete slug is shown in Figures 3.24 through 3.26. As with TURC2, the thermocouple data indicate no significant concrete ablation occurred. This is supported by posttest observations of the concrete slug.

A review of the peak temperature data within the first centimeter of concrete, at various radial locations shows the r = 18 cm region to be considerable lower in temperature than the radial centerline region. This observation indicates that the heat flux into the concrete was considerably less on the outer radius of the slug. This is consistent with the posttest observation of the green colored powder material described in Section 3.2.2.1, which caused a thermal resistance to the high temperatures of the melt pool.

As with the TURC2 thermocouple data, a distinct thermal arrest at ~400 K can be observed in the TURC concrete temperature data. As discussed in Section 3.2.1.2, this is referred to as the wet-dry interface.

In Figure 3.27, the location of the wet-dry interface is shown for the three radial locations. Once again, a comparison of the wet-dry interface position as a function of radial location suggests a lower heat flux into the concrete at r = 18 cm.

As outlined in Section 3.2.1.2 the calculation of the heat flux into the MgO wall, based on measured thermocouple response, was performed using the IHCP code. Results for axial locations 0 cm and 5.2 cm above the concrete interface are shown in Figures 3.28 and 3.29. At all locations, a similar characteristic of an elevated heat flux followed by a steady decrease was observed. However, the peak heat flux at z = 5.2 cm is lower than the z = 0 cm locations. The reason for this lower heat flux is not clear. It is speculated that the lower heat flux is a result of a deposit of material on the sidewall, possible Cs/I, near the melt-concrete interface.

The upper heat flux from the melt pool was measured by a heat flux gauge located in the sliding portcullis as discussed in Section 2.4. As with TURC2 the IHCP code was utilized to calculated the heat flux. The results are shown in Figure 3.30. This heat flux is a result of radiative and convective heat transfer within the upper plenum. As discussed in Section 3.2.1.2 a shape factor correction of 100 should be applied to the data in Figure 3.30 in order to obtain the melt pool surface heat flux.

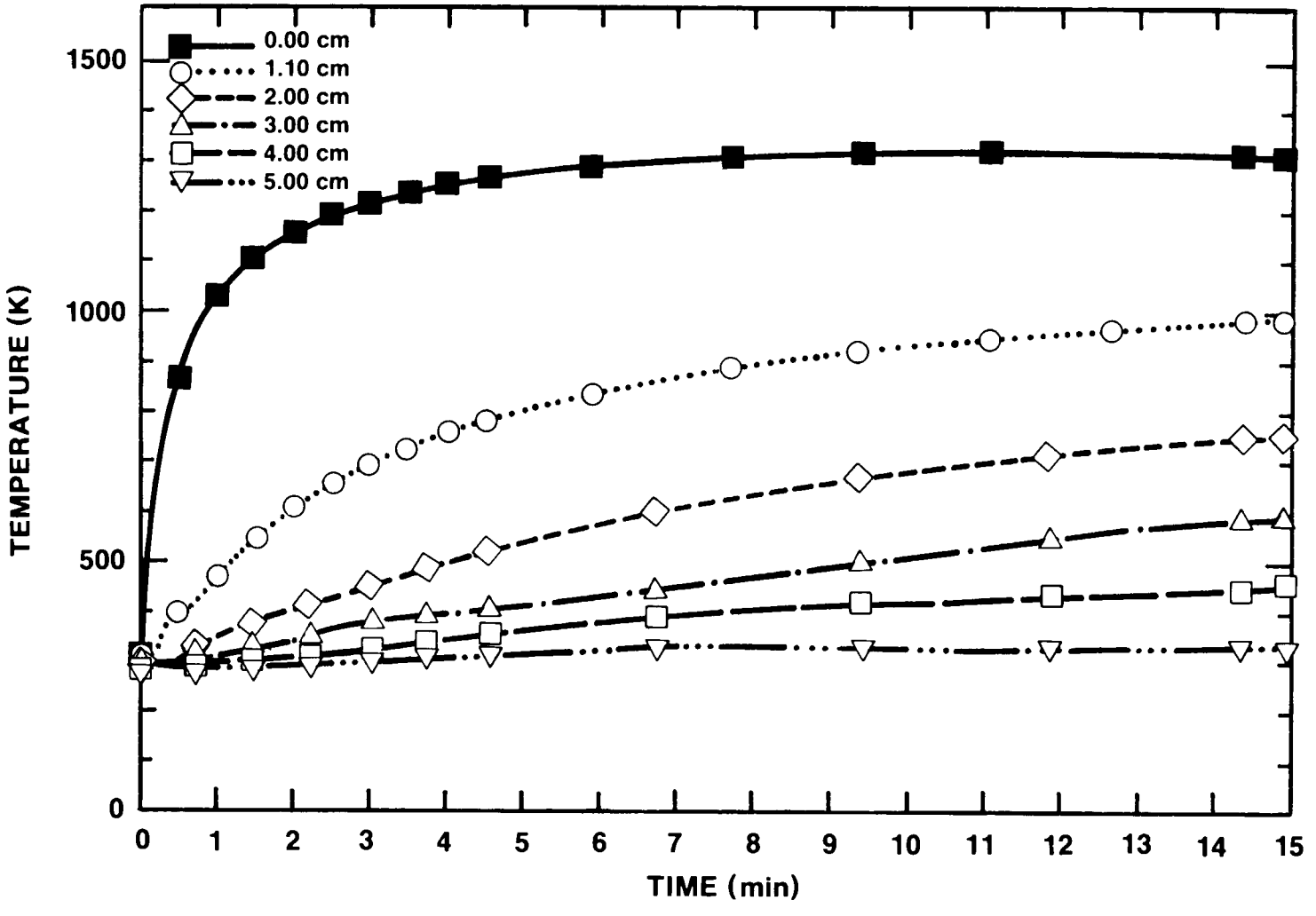

Figure 3.24. TURC3 Concrete Thermocouple Data, Location: Concrete Slug Centerline

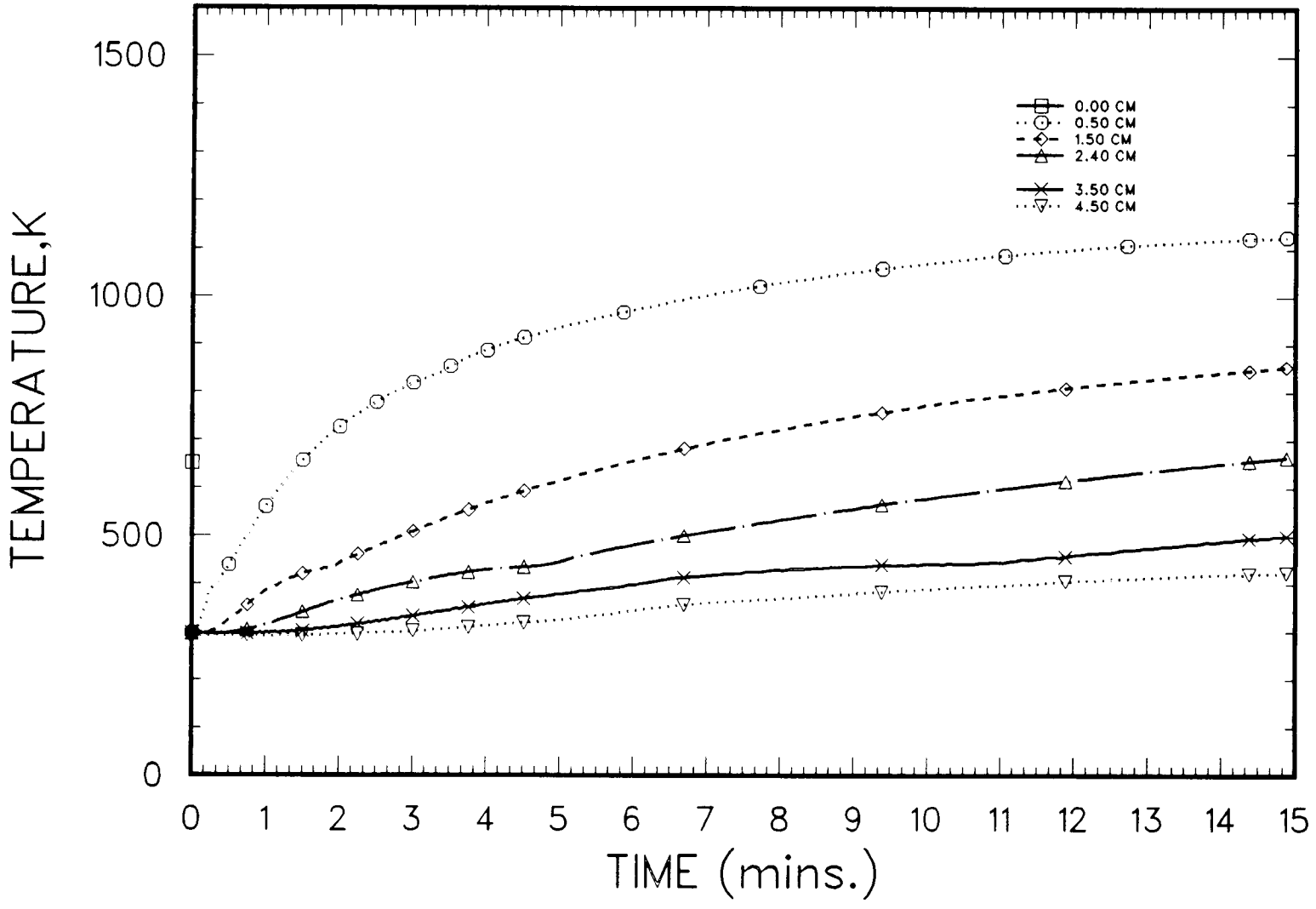

Figure 3.25. TURC3 Concrete Thermocouple Data, Location: r = 3 cm

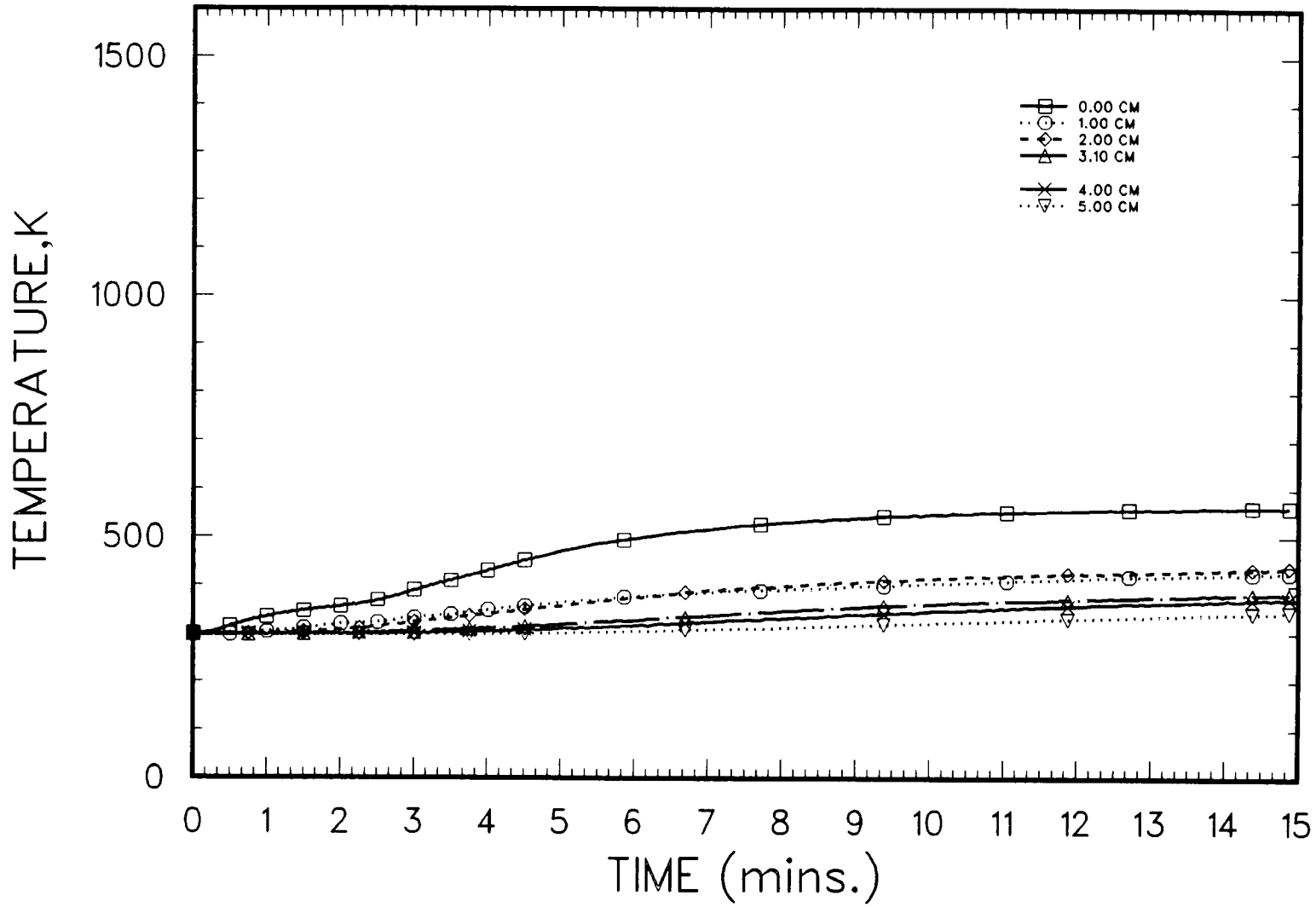

Figure 3.26. TURC3 Concrete Thermocouple Data, Location: r = 18 cm

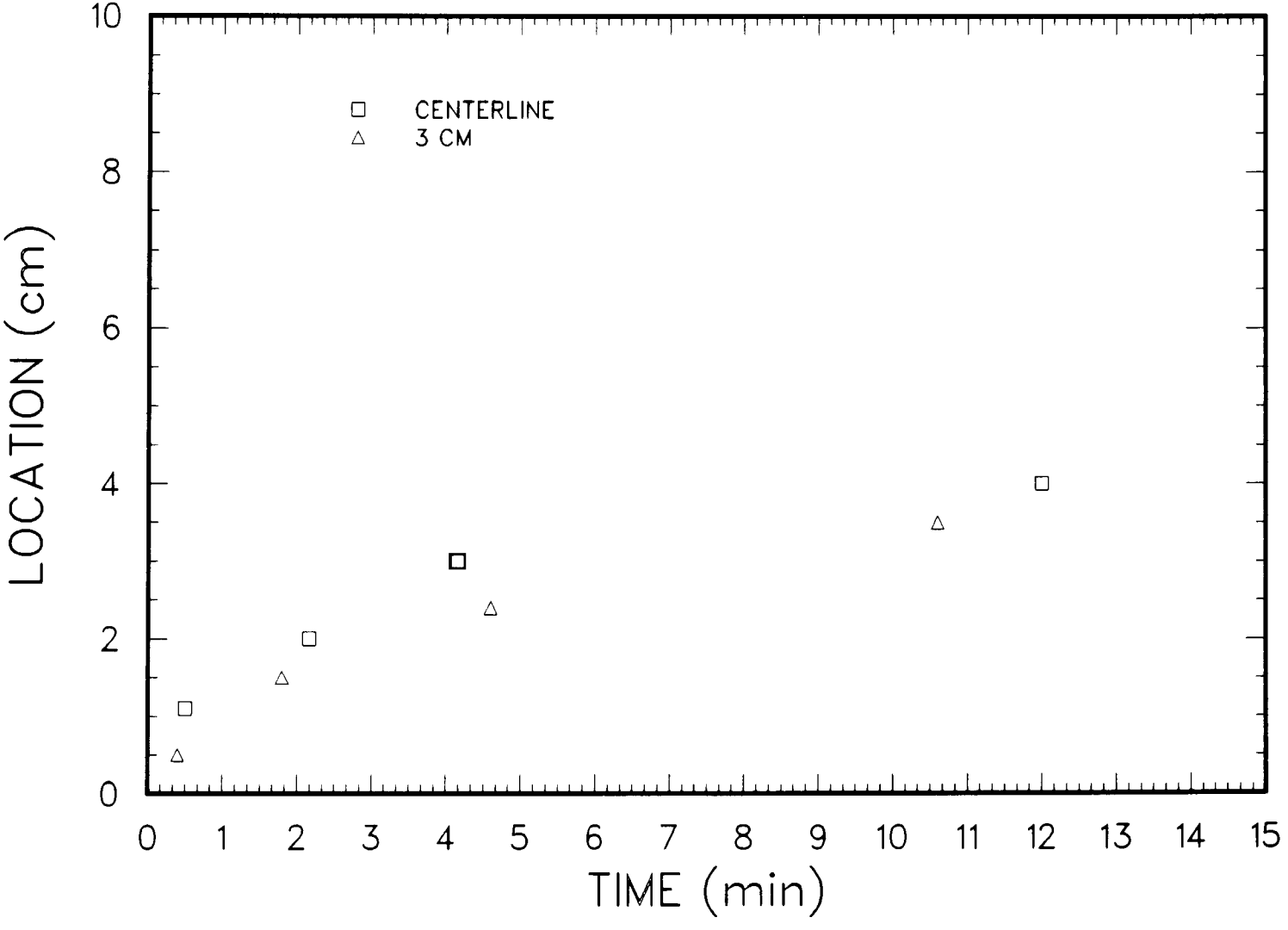

Figure 3.27. Wet-Dry Interface Location Within TURC3 Concrete Slug

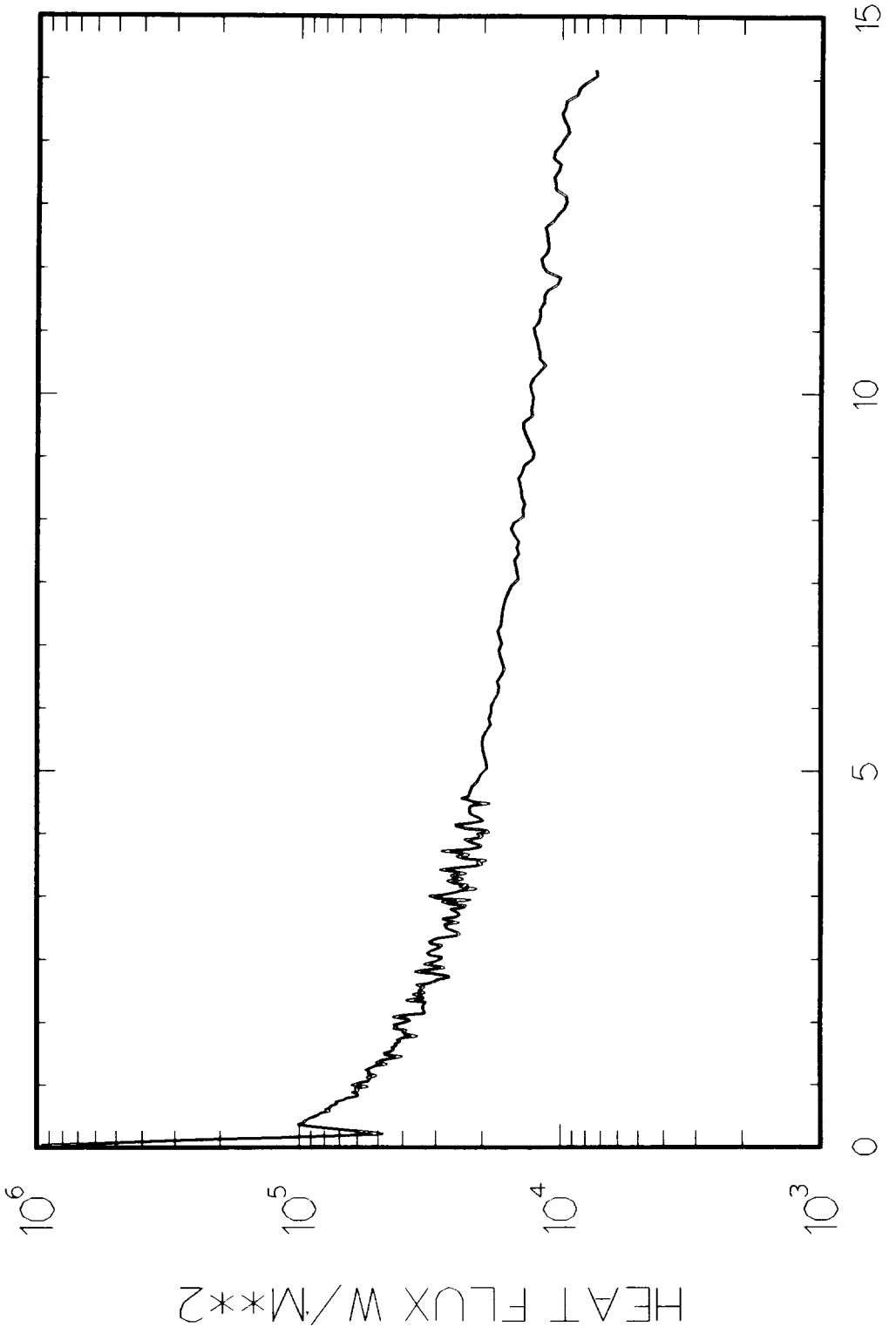

Figure 3.28. TURC3 MgO Heat Flux at z = 0 cm

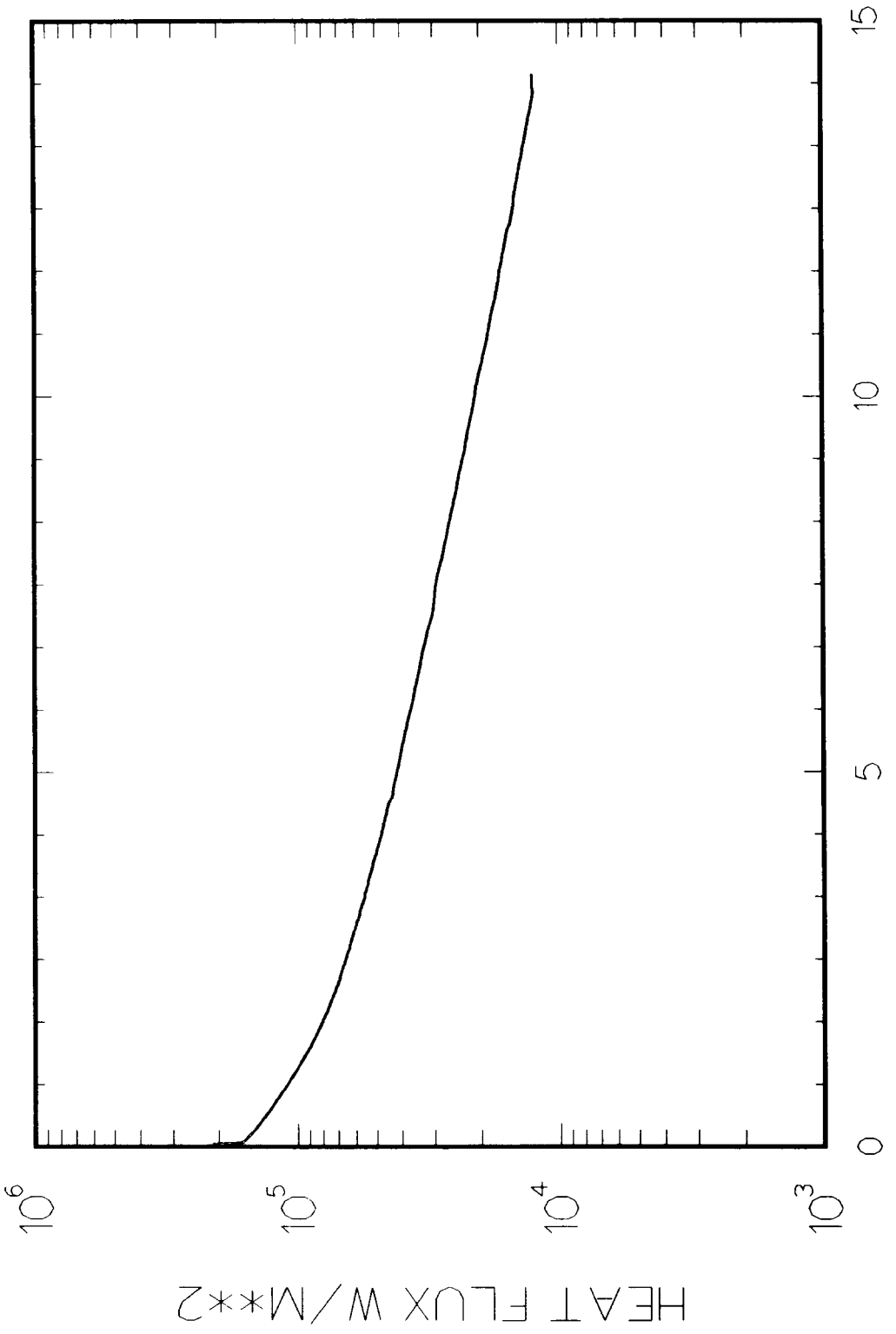

Figure 3.29. TURC3 MgO Heat Flux at z = 5.2 cm

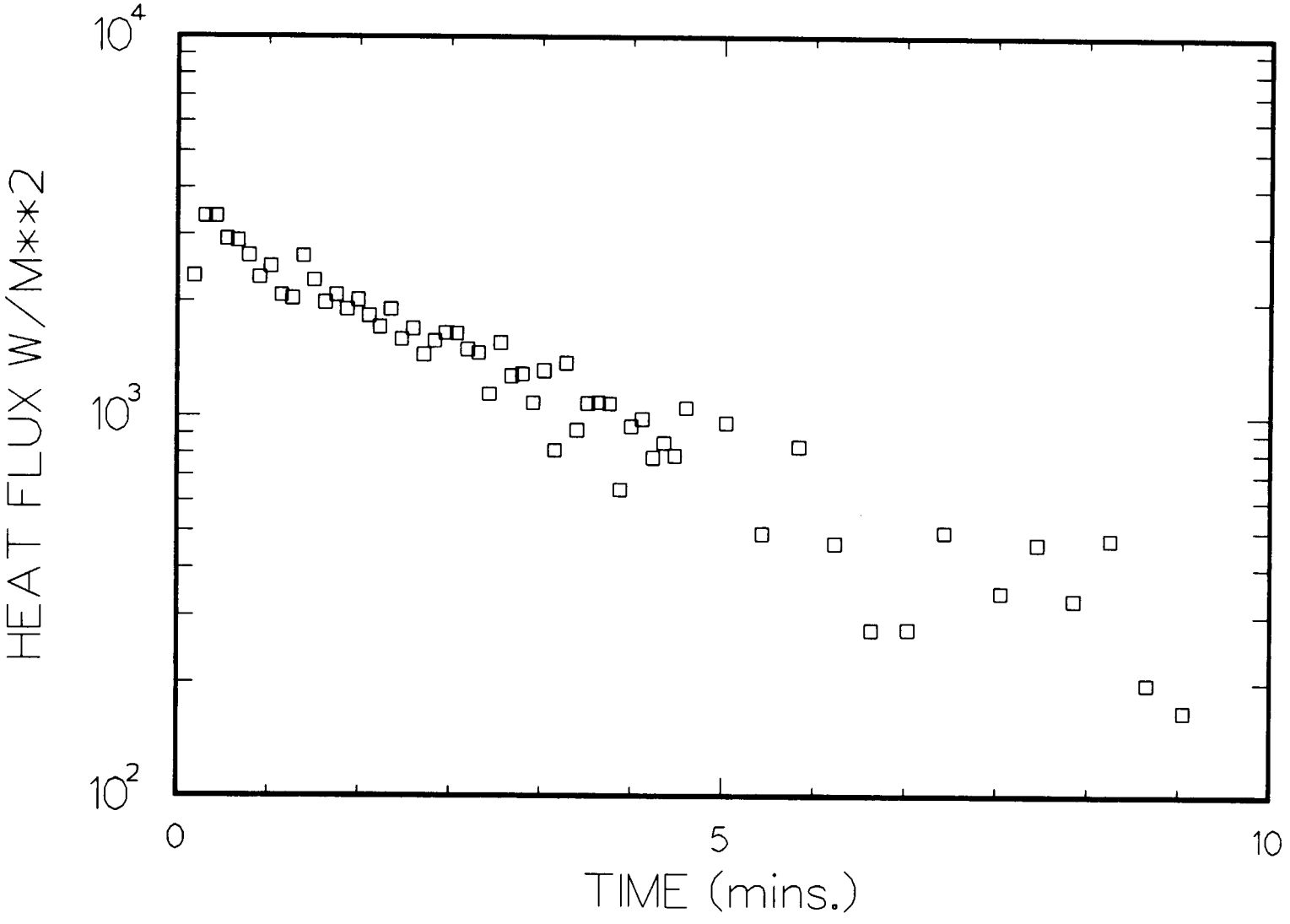

Figure 3.30. TURC3 Melt Pool Upward Heat Flux at the Portcullis

3.2.2.3 TURC3 Gas Composition and Flow Rate

As described in Section 2.4.2, discrete grab gas samples of evolving gases were taken throughout the test. The compositions of the thirteen gas samples are listed in Table 3.7. The time indicated in Table 3.7 is the time from initiation of melt teem. The results for sample number 1 indicate that the portcullis was either open or only recently closed due to the large amount of N_2 and O_2 present. (Note the relatively low quantities of N_2 and O_2 in subsequent samples.) As described in Section 3.2.1.3, measurements of water vapor content within the sampled gas were unsuccessful; hence quantitative equilibrium calculations are not possible.

As with TURC2, it is apparent from the gas sample composition that water vapor and CO_2 released from the decomposing concrete were reduced to combustible H_2 and CO. Shown in Figure 3.31, is the logarithm moles ratio of CO to CO_2. A comparison to the TURC2 data shows both experiments exhibited considerable reduction of CO_2 to CO at early times, but the TURC3 data showed a greater reduction of CO_2. This is most likely due to the Zr metal component within the TURC3 melt. This is a clear indication of the role of melt pool composition when evaluating combustible gas containment loads from a core-concrete interaction.

An argon seed gas was injected at a known rate of ~4.0×10^{-3} kg/sec in order to evaluate the gas flow rates from the experiment. As in TURC2, gas flow rates were inferred from the gas composition data by examining the mass fraction of the Ar constituent. Shown in Figure 3.32 are the flow rates as determined from the 13 gas samples. A comparison with TURC2 data shows similar trends, but indicates higher flow rates. The carbon mass flow rate is shown in Figure 3.33.

3.2.2.4 Aerosol Data for TURC3

Upon retrieval and disassembly of the aerosol sampling instruments from the TURC3 test, the following observations were made.

(1) The view windows of the opacity meter were clear and unobsecured. Purge gas flow was established 20 seconds before portcullis closure.

(2) The impactor samples did not appear to be overloaded. This was borne out by the weights of collected material. The dilution appeared to have been adequate in preventing overloading.

(3) The aerosol collected by the impactors and the filters was dark, almost black, in appearance as it was in the TURC2 test.

Table 3.7

TURC3 Gas Composition

Sample No.	Time (secs)	VOLUME PERCENT %					
		H_2	N_2	O_2	Ar	CO	CO_2
1	10.0	13.807	69.972	16.413	0.808	-	-
2	20.0	44.728	6.235	0.864	2.190	36.549	9.434
3	25.0	49.103	7.310	0.741	5.463	33.538	3.845
4	30.0	40.552	7.331	0.905	7.963	39.407	3.842
5	35.0	39.199	6.930	0.683	11.951	39.734	1.503
6	40.0	39.007	5.576	0.533	16.065	37.199	1.820
7	45.0	32.445	5.099	0.443	20.980	32.663	8.370
8	50.0	30.436	4.345	0.368	27.586	30.317	6.948
9	50.0	27.414	5.528	0.467	35.338	20.618	10.635
10	70.0	23.090	5.442	0.571	40.286	15.353	15.258
11	80.0	20.188	5.483	0.553	45.501	12.069	16.106
12	90.0	13.068	5.807	0.508	51.485	9.308	19.725
13	100.0	10.913	8.574	0.774	52.868	8.412	18.459

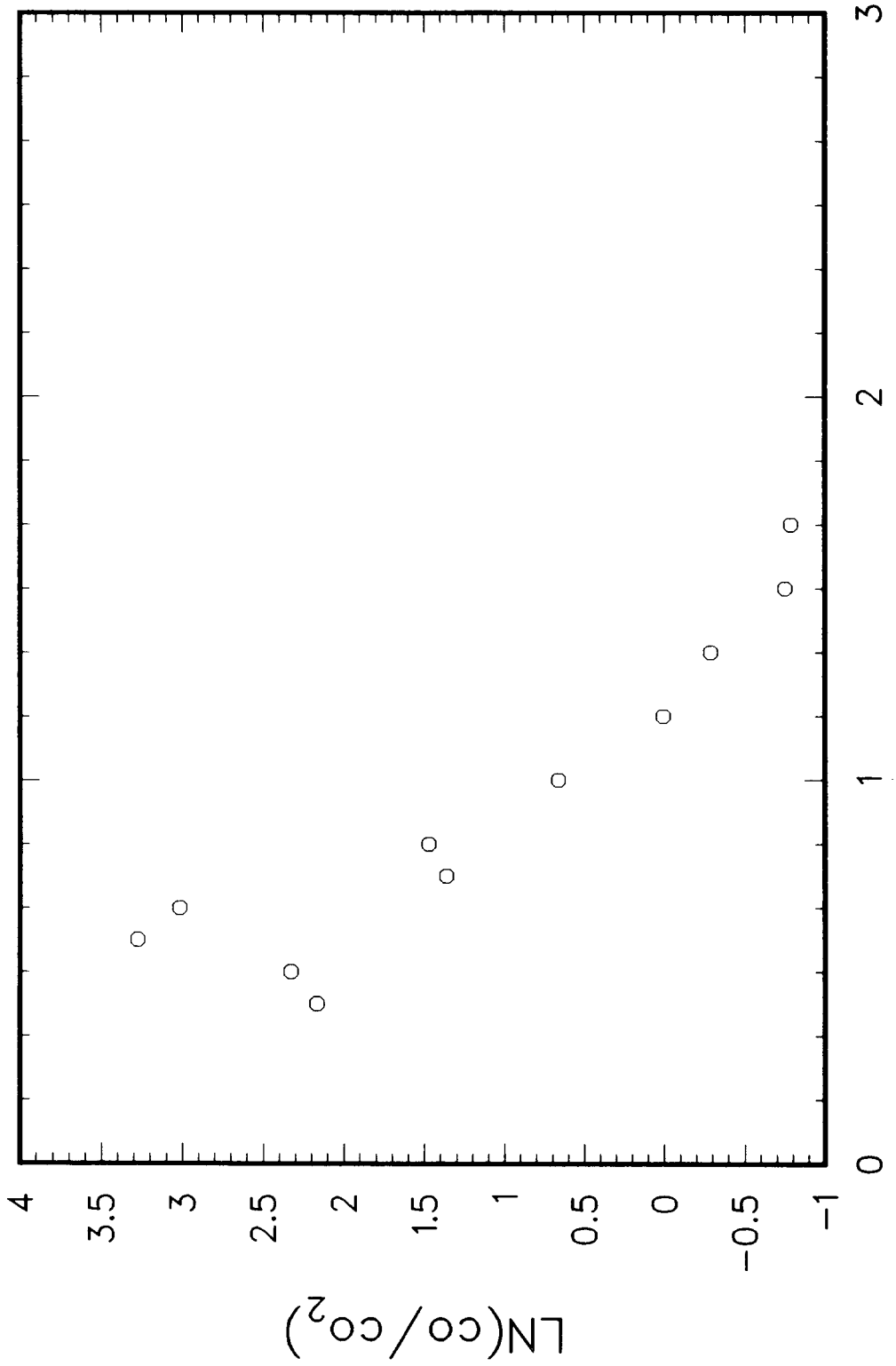

Figure 3.31. TURC3 Gas Sample Ratio of CO/CO_2

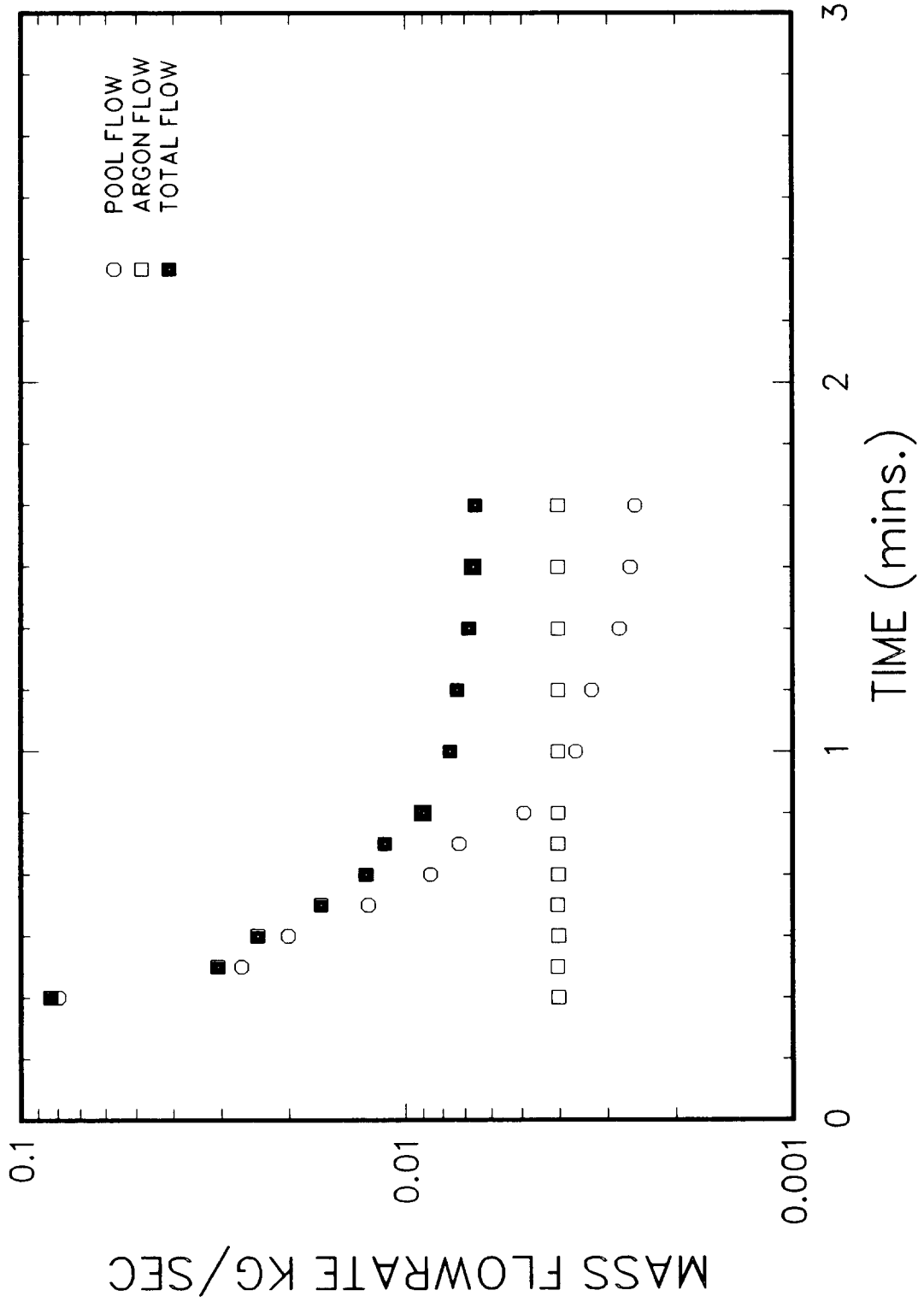

Figure 3.32. TURC3 Gas Flow Rates

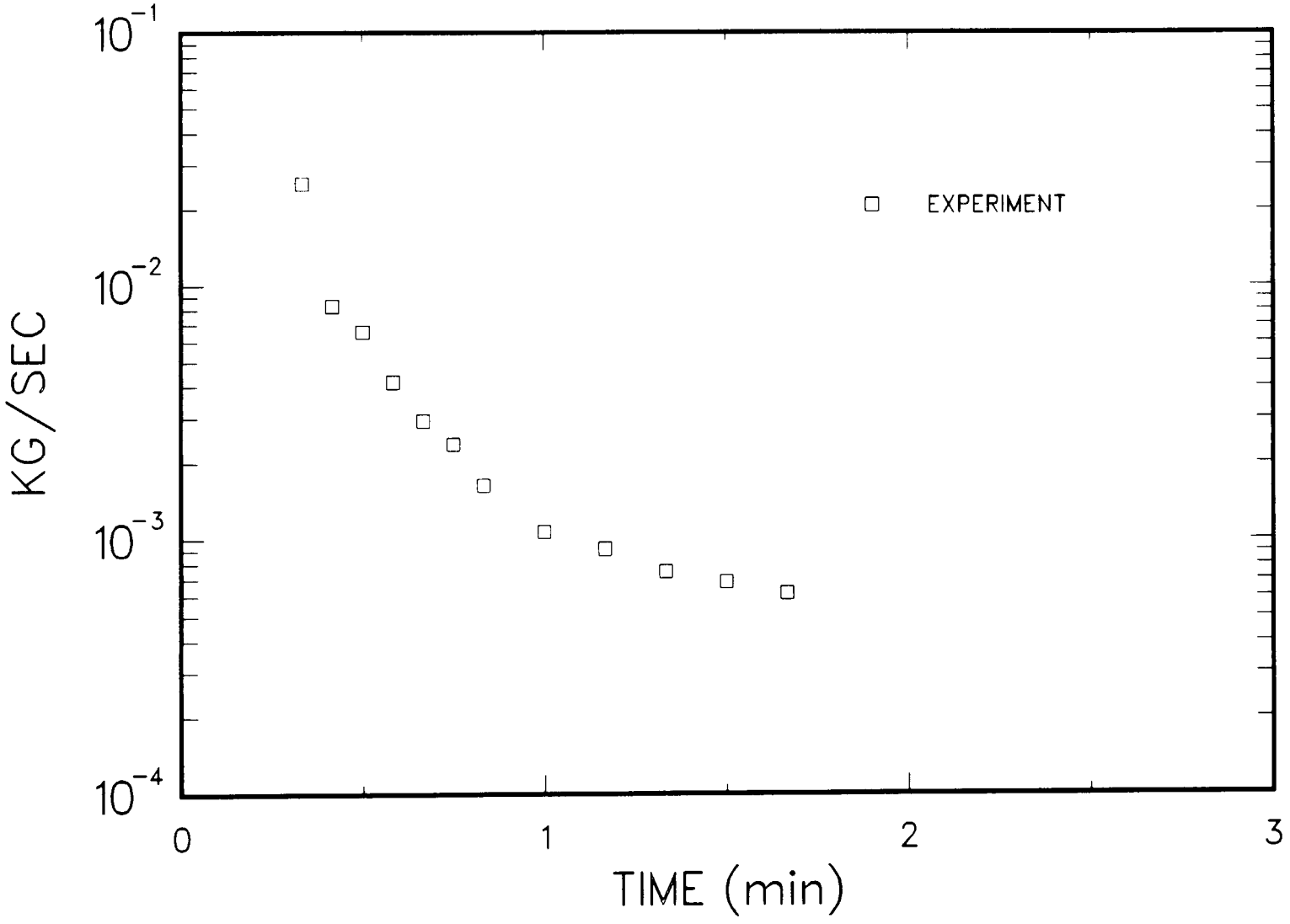

Figure 3.33. TURC3 Carbon Flow Rate

Filter Data: The locations of the filter samples on TURC3 are the same as on TURC2. The measured aerosol concentrations and sample times are given in Table 3.8. The zero time is taken as the time of portcullis closure, 15 seconds after the initiation of the teem. Concentrations and flows are given at STP.

Opacity Monitor: The trace from the opacity monitor is given in Figure 3.34 along with the aerosol concentration measurements from the filters. The opacity trace gives percent opacity as a function of time. The data correlate reasonably well although there seems to be a time lag of approximately 10 seconds in the initial data. No explanation of this has been given. Further analysis and correlation of measured aerosol concentration with opacity have not been performed.

The opacity monitor indicates an initially high aerosol concentration which drops to a very low level about 25 seconds after portcullis closure and rises again to a high concentration at about 40 seconds.

Impactor samples: The locations of the impactors was the same as in the TURC2 test. The dilution appeared to have prevented overloading. Figure 3.35 is the size distribution obtained by averaging the distributions of impactors 1 and 2 which sampled from 0 to 20 seconds after portcullis closure. This distribution is representative of the distributions measured by the other impactor samples and is similar to that measured in TURC2. The distribution is predominantly unimodal with the mass mean aerodynamic diameter located between 1 and 2 μm and a geometric standard deviation of about 2.0. Table 3.9 contains the gross impactor data for the impactors run on the TURC3 test. Sample time, mass collected, flow rate, aerosol concentration, and dilution rate are given.

Chemical Analysis: The same dopants used in TURC2 were used in TURC3 (listed in Table 2.2). Qualitative XRF analysis was performed on two selected filter samples from TURC3 (sample B; 10 to 20 seconds and sample F; 120 to 150 seconds). Table 3.10 contains the results of this analysis for selected elements. These results are qualitative and are not an exhaustive analysis of the elements present.

Qualitative PIXE analysis has also been performed on selected aerosol filter samples from TURC3. They are sample A (0 to 10 seconds), sample C (20 to 40 seconds), sample D (40 to 60 seconds), sample E (60 to 90 seconds), sample H (330 to 360 seconds), and sample A taken from the interaction chamber (0 to 20 seconds). The results from the PIXE analysis concur with the XRF results that Te, I, and Cs are the major aerosol constituents. Tellurium appears to be significantly released even after five minutes. Manganese was also detected as a significant component of the aerosol, perhaps more so than would be suggested by XRF analysis. Uranium was detected at trace levels as was Ni

Table 3.8

Aerosol Filter Data for TURC3

Sample	Sample Time* (sec)	Collected Mass (mg)	Sample Flow Rate (SLPM)	Aerosol Concentration at STP (g/m^3)
Exhaust Line				
A	0-10+	28.0	6.9	24.3
B	10-20**	15.7	6.9	13.7
C	20-40+	15.6	6.9	6.8
D	40-60+	19.0	6.9	8.3
E	60-90+	35.5	6.9	10.3
F	120-150**	33.0	6.9	9.6
G	240-270	28.5	6.9	8.3
H	330-360+	18.3	6.9	5.3
I	420-450	11.7	6.9	3.4
Interaction Chamber				
	0-20+	34.0	2.0	51.0
	0-20	38.9	2.0	58.4

*Time after portcullis closure

**Analyzed by XRF

+Analyzed by PIXE

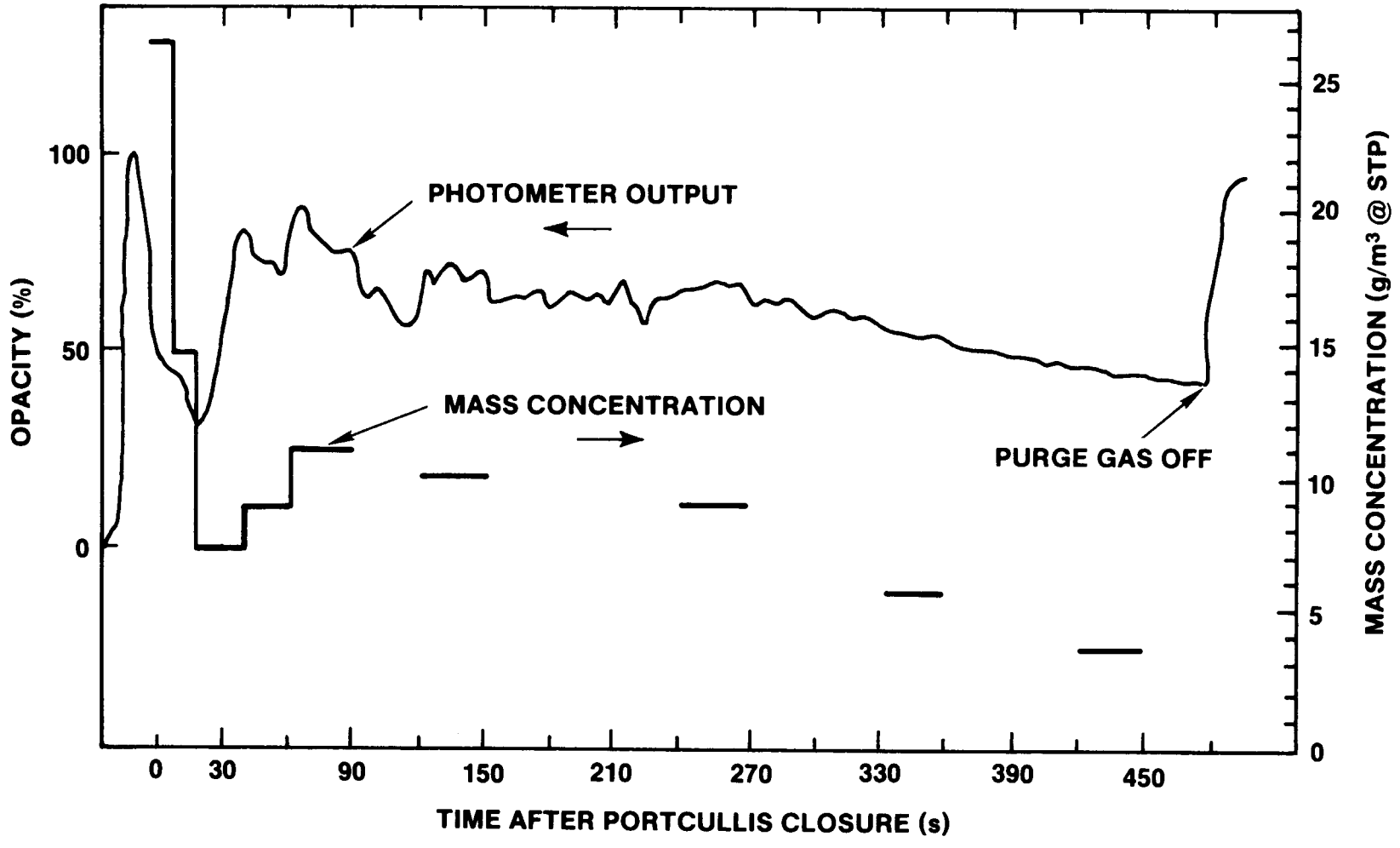

COMPARISON OF FILTER MASS CONCENTRATION MEASUREMENTS
WITH PHOTOMETER MEASURED OPACITY IN TURC 3 TEST

Figure 3.34. TURC3 Opacity Monitor Output

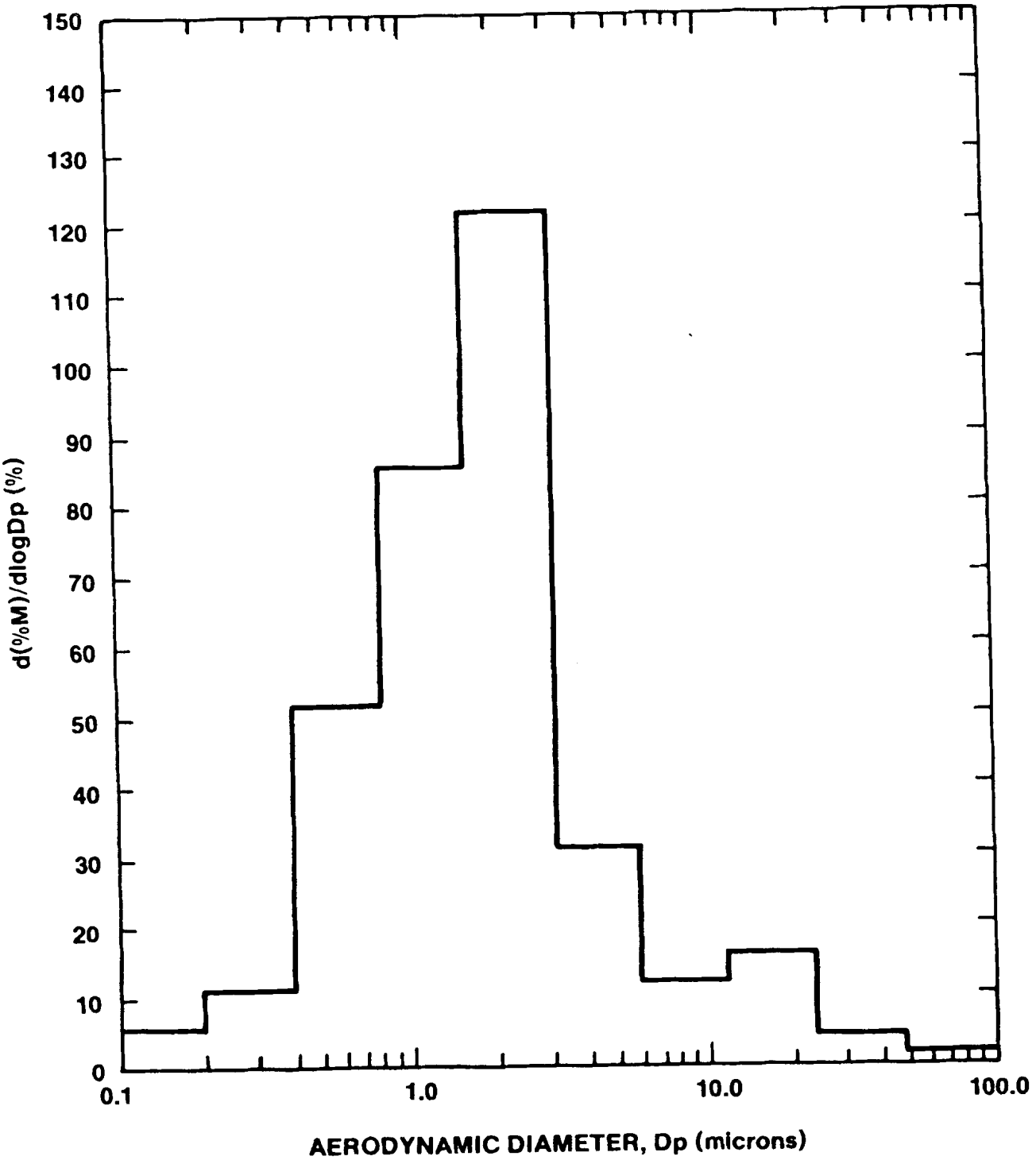

Figure 3.35. Measured Aerosol Size Distribution from TURC3. Combined Data from Impactors 1 and 2

Table 3.9

Aerosol Impactor Data for TURC3

Sample Time* (sec)	Impactor (-)	Collected Mass (mg)	Sample Flow Rate (SLPM)	Combined Aerosol Concentration** (g/m^3)
0-20	1	20.6	6.2	22.4
0-20	2	28.0	9.3	
20-40	3	21.7	6.4	21.1
20-40	4	24.0	9.1	
60-90	5	15.2	6.5	11.2
60-90	6	21.0	8.9	
240-270	7	13.0	6.2	9.9
240-270	8	19.3	9.4	

*Time after portcullis closure

**Dilution ratio of 2.38:1 is applied

Table 3.10

XRF Analysis of TURC3 Aerosol Samples

	Qualitative Analysis Sample	
Element	B (10 to 20 sec)	F (120 to 150 sec)
Cs	M	M
I	M	M
Te	M	M
Ti	S	S
K	S	S
Mg	S	S
Mn	S	S
Sb	S	S

Levels: M = Major Constituent
S = Minor Constituent

Examined for but not detected were
Ba, Ce, La, Ni, Mo, and Ca

and Mo. Tungsten was detected as a very minor aerosol constituent. This is in accord with the lack of tungsten parts found in the TURC3 test and is an interesting contrast to the tungsten release noted in TURC2.

3.2.2.5 TURC3 Posttest Melt Pool Composition and Melting Point

As with the TURC2 debris, general representative samples of the TURC3 melt pool debris were removed for elemental composition analysis by XRF and melting point determination by the cone slumping method. The XRF and melting point data are listed in Tables 3.11 and 3.12, respectively.

It is fairly clear from the qualitative XRF data that decomposed concrete constituents were introduced into the bulk debris material. This is felt to be the reason, once again, for the depression in the melting point of the debris. One must exercise care in extending these data beyond the simple fact that relatively small quantities of concrete constituents (and/or fission product species) have a significant impact on the melting point of UO_2 laden debris.

Table 3.11

TURC XRF Elemental Analysis

Element	Pretest* Material	Melt Pool Outer Radius at Concrete Interface (Green Deposit)	Less than 1 cm above Melt-Concrete Interface at Radial Centerline	Melt Pool Outer Radius 3-4 cm above Concrete Interface	Center of Melt Pool
U	M	T	M	M	M
Ti	–	–	–	–	–
Mn	–	S	–	S	–
Fe	–	–	S	–	S
Zr	M	–	M	M	M
I	–	M	–	–	–
Cs	–	M	–	S	–
Al	–	–	S	–	S
Si	–	–	S	–	S
Ca	–	–	S	–	S
Ba	–	–	S	S	S
K	–	–	–	–	–
Mo	–	–	–	–	–
W	–	–	–	–	–

NOTE: M: Major Component, S: Small Component, T: Trace,
–: Not Detected

* $UO_2/ZrO_2/Zr$, No Fission Product Mocks

Table 3.12

TURC3 Melt Pool Melting Point

Material Description	Melting Point
Original Material*	2575 • 10 K
Melt-Concrete Interface Radial Centerline	2275 - 2295 K
Melt-Concrete Interface Outer Radius (green deposit included)	2235 • 10 K
Melt Pool Center	2492 - 2523 K

*UO_2 (64 w/o)/ZrO_2 (27 w/o)/Zr (9 w/o), no fission product mocks

4. EXPERIMENT ANALYSIS

4.1 Introduction

4.1.1 Purpose and Background

This section presents an analysis of the results of the TURC2 and TURC3 experiments. An analysis of the experimental results is performed using a heat balance model that has been written primarily for analysis of these, and other similar, experiments of 1-D concrete ablation with refractory sidewalls.

4.1.2 Method of Analysis

The model consists of a collection of modules that predict the various heat losses. The major heat loss mechanisms are: losses to the ablating concrete, wall losses, radiative losses from the top of the pool, and losses to the gases escaping from the concrete.

4.2 Description of Heat Balance Model

A detailed description of the model including all of the various equations and numerical methods of solution appears in the TURC1 document[9] and will not be repeated in this report. Briefly summarized, the model that is used in making the heat balance calculations for the TURC experiments is a three region model. The three different regions are: the pool/melt region, a wall region, and a concrete region.

The pool region includes conservation equations that solve for both chemical species distributions and the temperature distribution. The equations are one-dimensional, yielding vertical distributions as a function of time and boundary conditions.

The wall region represents the refractory MgO wall that surrounds the pool melt. A two-dimensional (R/Z) conservation equation for the temperature distribution is solved in this region.

The concrete region includes both a wet and dry zone. The wet zone is that area where liquid water exists and the dry zone is that region where no liquid water exists. Both zones include conservation equations for temperature and mass distributions. All of the equations in this region are one-dimensional.

The melt/concrete interactions typically involve ablation of the concrete. Moving coordinate systems that are attached to the boundaries of the various regions are used and the motion is

accounted for by advection of material and/or energy through the regions.

In performing the experiment analysis several assumptions were made in order to simplify the complexity of the calculations. The simplifying assumptions involved assumed values of thermophysical properties of the various materials and effective heat transfer coefficients between the melt pool and the MgO wall, and between the upper crust and the overlying atmosphere, and, where necessary, between the melt pool and the concrete surface.

The various thermophysical properties of the materials used in the TURC2 and TURC3 experiments appear in Table 4.1.

In modeling the heat losses from the melt pool it was found that liquid-solid contact between the melt pool and the MgO wall would lead to excessive heat fluxes when compared to the experimental data. Therefore, a heat transfer coefficient was placed in series between the UO_2 crust at the wall and the wall itself. The magnitude of the heat transfer coefficients are discussed in the text.

The heat transfer from the upper melt pool crust to the experiment crucible cavity was best characterized by a convective heat transfer coefficient of 30 W/m^2K acting in parallel with a purely radiative heat transfer coefficient with an emissivity of 0.3.

4.3 Comparison with Experiment

The analysis of the TURC2 and TURC3 experiments can be separated into two categories. In category one the model predictions can be compared directly with the data derived from the experiments. The comparison is provided so that the model and its predictions for these experiments receives some level of validation. The model predictions for category 2 are those predictions which cannot be compared to experimental data simply because there is no data.

In category one there are four main types of experimental data that can be compared with the model predictions:

(a) Thermocouple temperature histories at various depths in the concrete.

(b) The erosion front and the wet/dry front locations. Both of these front locations are derived from the thermocouple temperature histories.

Table 4.1

Thermophysical Properties of the Materials in the TURC2 and TURC3 Experiments

	Concrete	MgO Wall	Melt Pool TURC2	Melt Pool TURC3
Density (Kg/m^2)	2400	2640	8036	7663
Bound Water (%)	2.0	-	-	-
Evaporable Water (%)	2.7	-	-	-
CO_2 Content (%)	22.0	-	-	-
Specific Heat (J/KgK)	1100	1250	596	587
Melt Temperature (K)	1550	-	2657	2575
Thermal Conductivity (W/mK)			3.15(s)	3.2(s)
$K = AT + B \geq C$	A = -0.0012 B = 2.4 C = 0.12	A = -0.005 B = 8.193 C = 1.966	4.82(l)	4.9(l)

where

K is the thermal conductivity
T is temperature in Kelvin
C is the minimum thermal conductivity
(s) refers to the solid phase
(l) refers to the liquid phase

(c) The MgO wall heat flux history. The predicted heat flux from the model is compared with the inverse heat flux calculations from the previous section (3.2.1.2 and 3.2.2.2)

(d) The gaseous carbon mass flow. This is defined as the mass rate of flow of carbon in kg/sec from both CO and CO_2. The model does not predict chemical reduction of CO_2 to CO so that chemical composition comparisons are not possible. However the model does predict CO_2 release from the concrete so that the total carbon content of the decomposition gases can be compared with experimental measurements.

The results of the analysis indicate that the behavior of both experiments was similar, therefore the results of the analysis will be presented simultaneously for both experiments in order to avoid duplication of discussion, definitions, and implications. Any differences between the experiments will be pointed out directly in the discussion of results.

Comparisons of the predicted and the measured thermocouple response are shown in Figures 4.1 through 4.3 for both experiments. An inspection of the figures reveals excellent agreement between the experimental data and the model predictions for both experiments. The figures shown are for the centerline of both experiments and the 18-cm radius for the TURC2 experiment.

The 18-cm radius thermocouple response for the TURC3 experiment is not shown because it could not be matched exactly. A reasonable approximation for the TURC3 18-cm radius thermocouple response could be obtained by placing a thermal resistance equivalent to a heat transfer coefficient of 20 W/m^2K in series between the melt pool and the concrete surface. The thermal resistance would undoubtedly correspond to the greenish powder that was found separating the frozen pool and the concrete surface from the 15 cm radial location outwards to the MgO wall. The inability of the model to match the thermocouple response exactly implies that the thermal resistance of the greenish powder varied with time.

Figures 4.4 and 4.5 show the predicted erosion front locations for the TURC2 and 3 experiments. The model predicts a very small amount of surface erosion for both experiments (2 and 1 mm, respectively). That level of erosion is consistent with the thermocouple data. For both experiments the thermocouple data indicated no erosion to the nearest 5 mm. Physical inspection of the melt pool showed a small amount of concrete within the melt pool-concrete surface boundary layer. In addition, physical separation of the melt pool from the concrete revealed the concrete aggregate as a clearly discernible mosaic indicating that at least the thin top surface layer of concrete had been melted.

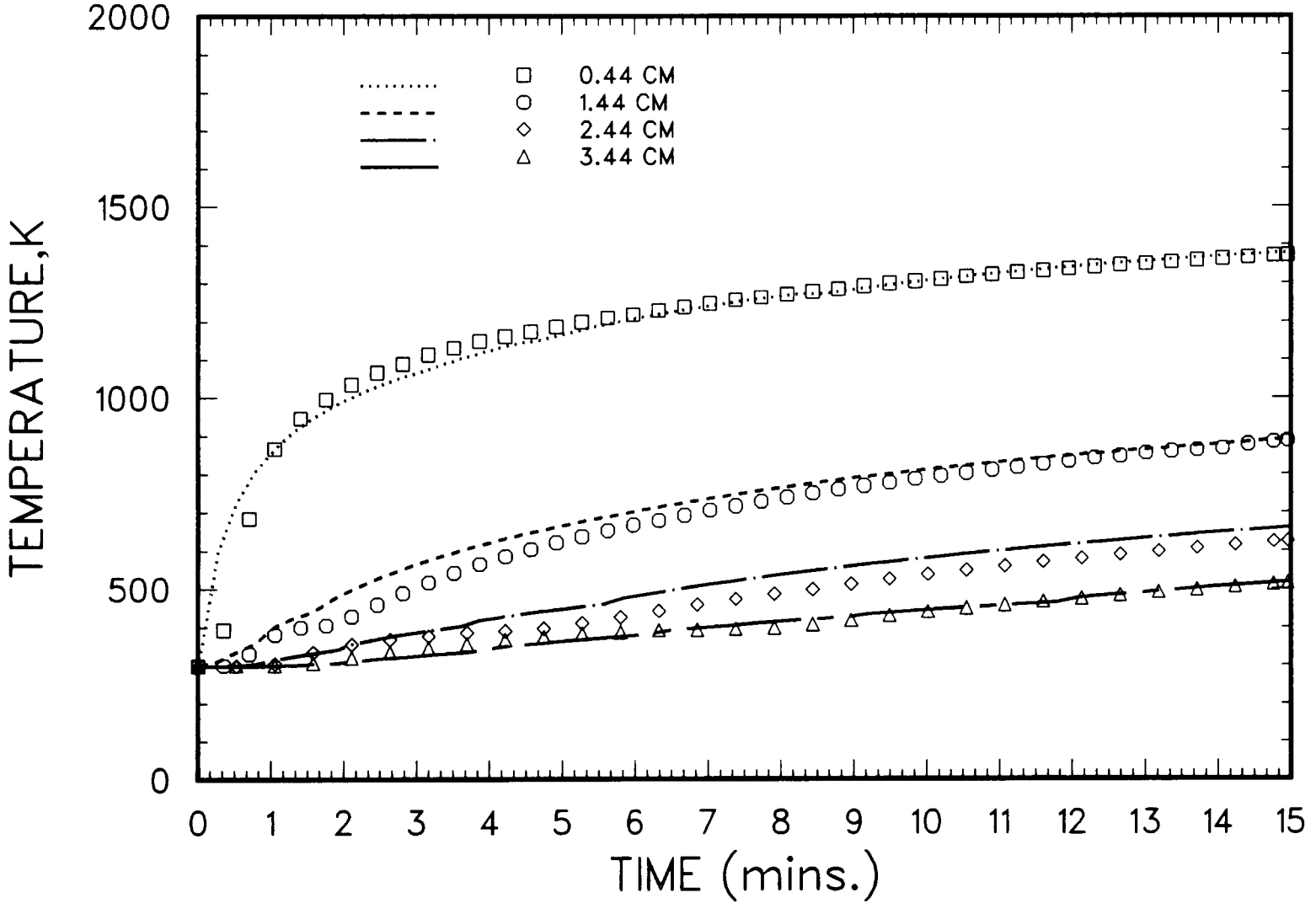

Figure 4.1. Comparison of the Predicted and Measured Thermocouple Response at the Concrete Centerline in the TURC2 Experiment

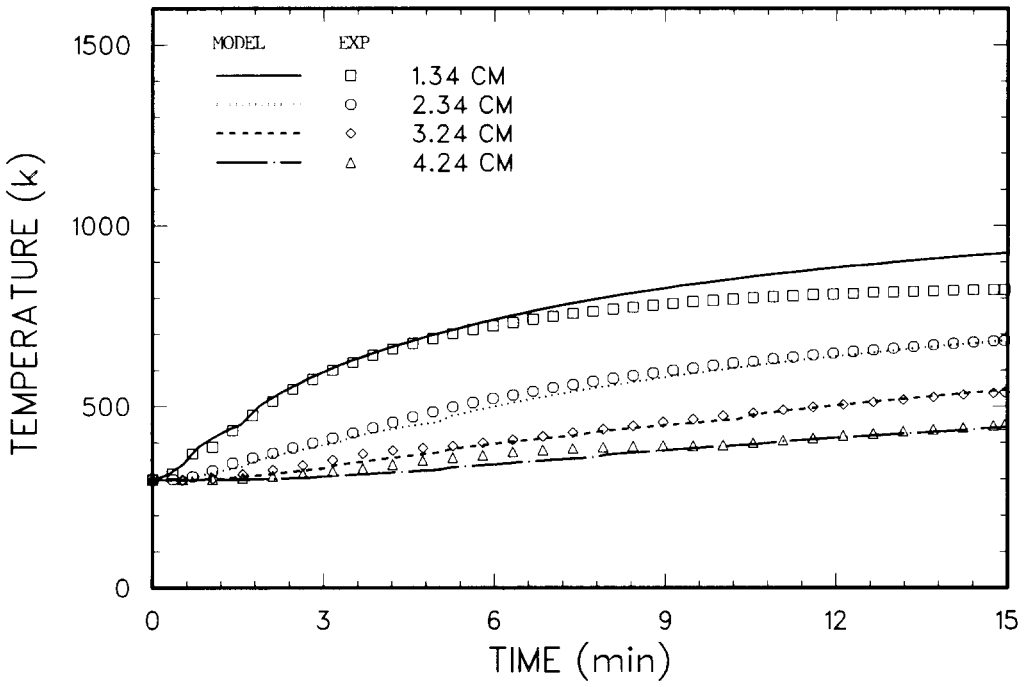

Figure 4.2. Comparison of the Predicted and Measured Thermocouple Response at the Concrete Mid Radius (18 cm) in the TURC2 Experiment

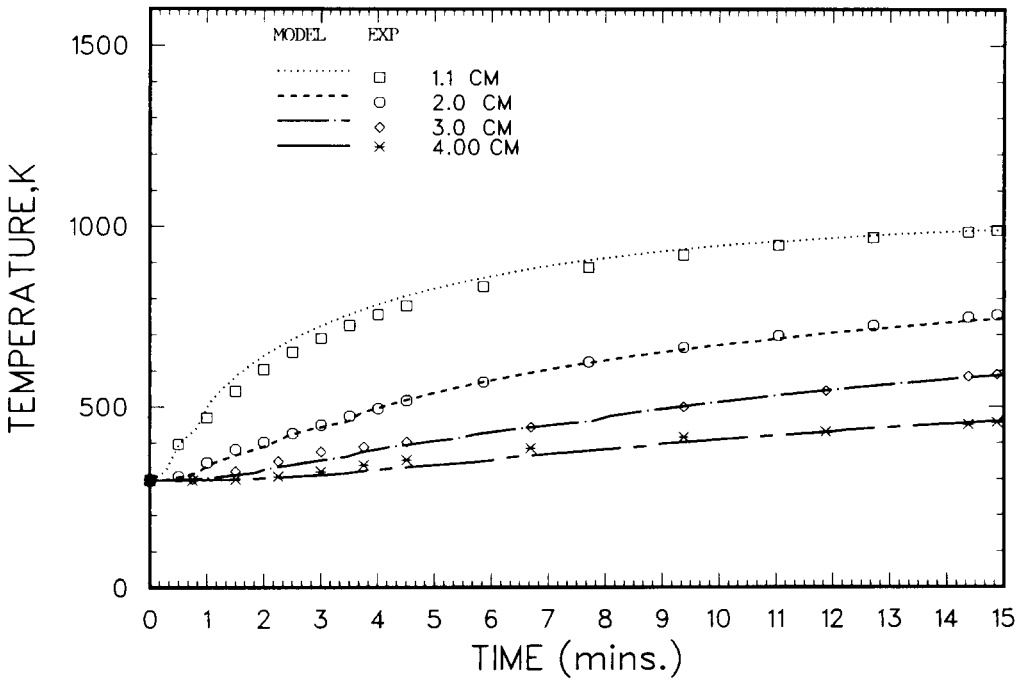

Figure 4.3. Comparison of the Predicted and Measured Thermocouple Response at the Concrete Centerline in the TURC3 Experiment

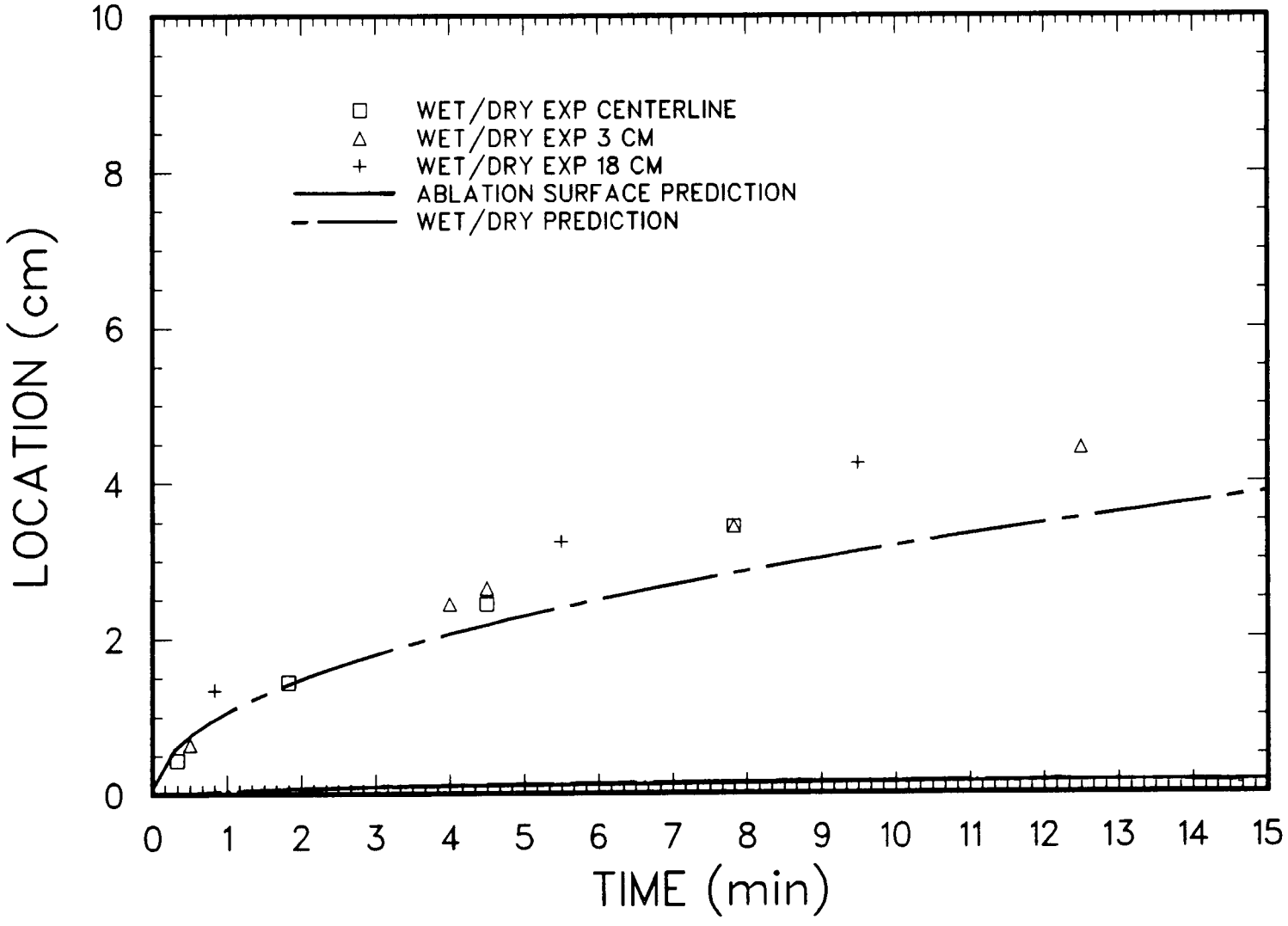

Figure 4.4. The Predicted Erosion and Wet Front Locations for the TURC2 Experiment

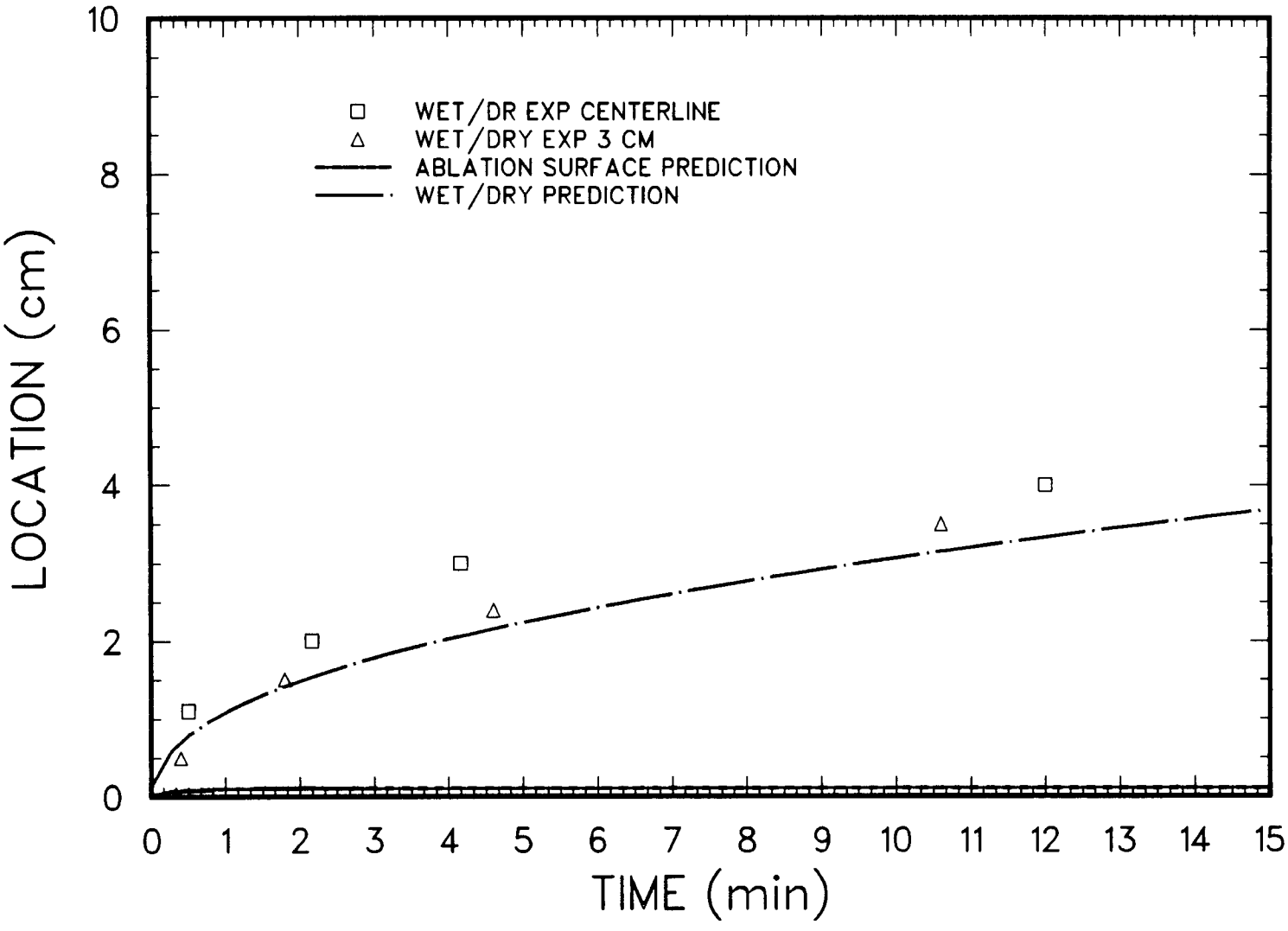

Figure 4.5. The Predicted Erosion and Wet Front Locations in the TURC3 Experiment

The change in melting temperature is an effect that is not included in the model but is known to exist both in principle and as measured (see Tables 3.6 and 3.12) data. It would seem that the depression in melt temperature, due to ablation, should keep the pool in a molten state long enough for some measurable ablation to occur. By plotting the predicted thermal history within the melt pool boundary layer for the TURC2 experiment, it is found that the lowermost 1/2 cm of the melt pool will freeze and drop to a temperature below the lowest measured boundary layer melt temperature (Table 3.6 T_{melt} ~2355) within the first 30 seconds. Thus the model predicts that it is the very rapid freezing and low boundary layer temperatures that account for the minimal ablation that is found in the experiments.

The wet front locations for both experiments are also shown in Figures 4.4 and 4.5. The wet front is defined as the planar locations that separates the regions of concrete which do and do not contain evaporable (liquid) water. In the model the wet front is a point in its one-dimensional space. Physically the wet front exists as a zone of variable thickness where the liquid water is evaporating. The location of the wet front can be derived from the experimental thermocouple traces by selecting the point where the initial plateau in temperature rise changes slope and begins rising a second time. Those wet front locations, corresponding to the various thermocouple positions, are shown as the experimental data points in Figures 4.3 and 4.4. There appears to be a small discrepancy between the model and the experimental data. The discrepancy may be attributed to differences in assumed versus real thermophysical and water content properties of the concrete. Another possibility is that liquid water migration occurs at a greater rate than the model currently predicts.

Figures 4.6 and 4.7 are plots of the predicted versus measured MgO annulus wall heat fluxes as a function of time. Quite good agreement is shown for both experiments. In order to obtain this agreement a significant thermal resistance had to be placed in series between the UO_2 crust growing along the wall and the wall itself. The thermal resistance in both of the experimental predictions was best characterized as a purely radiative phenomena with a net emissivity/absorptivity of 0.09. Such a low value of emissivity/absorptivity indicates that the radiation most likely had to diffuse through a layered or powdery structure rather than across a single clean air gap. The slight discrepancy at later times could easily be accounted for by changing thermophysical properties and changes in the gap thermal resistance as a function of time. Recall that the posttest analysis in both experiments revealed a gap, thin crusts, and powder adhering to the MgO sidewalls.

Figures 4.8 and 4.9 are plots of the gaseous carbon mass flow predictions versus experimental data for the TURC2 and TURC3 experiments. Reasonably good agreement is found for the TURC2

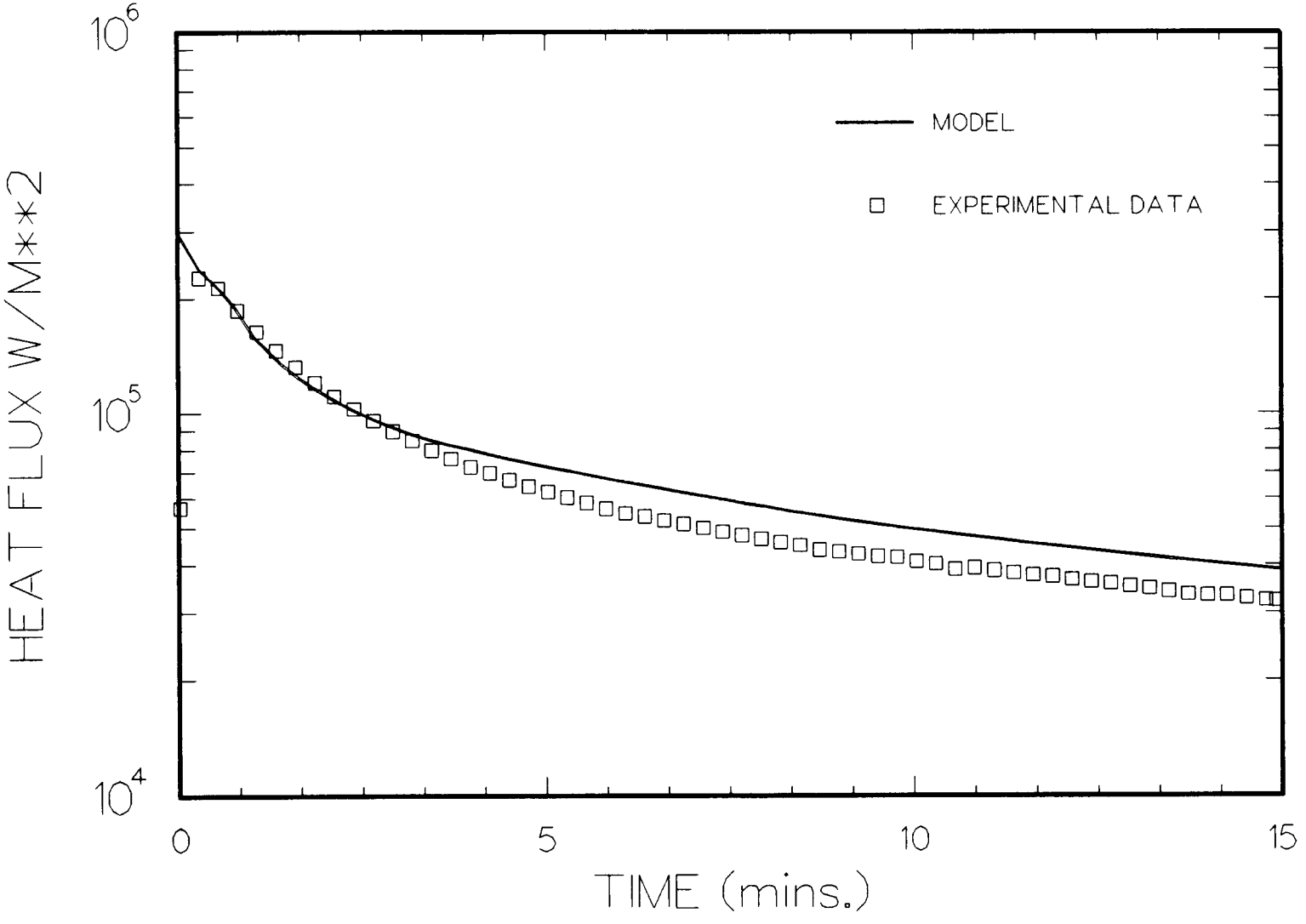

Figure 4.6. Comparison of Predicted and Inferred MgO Wall Heat Flux in the TURC2 Experiment

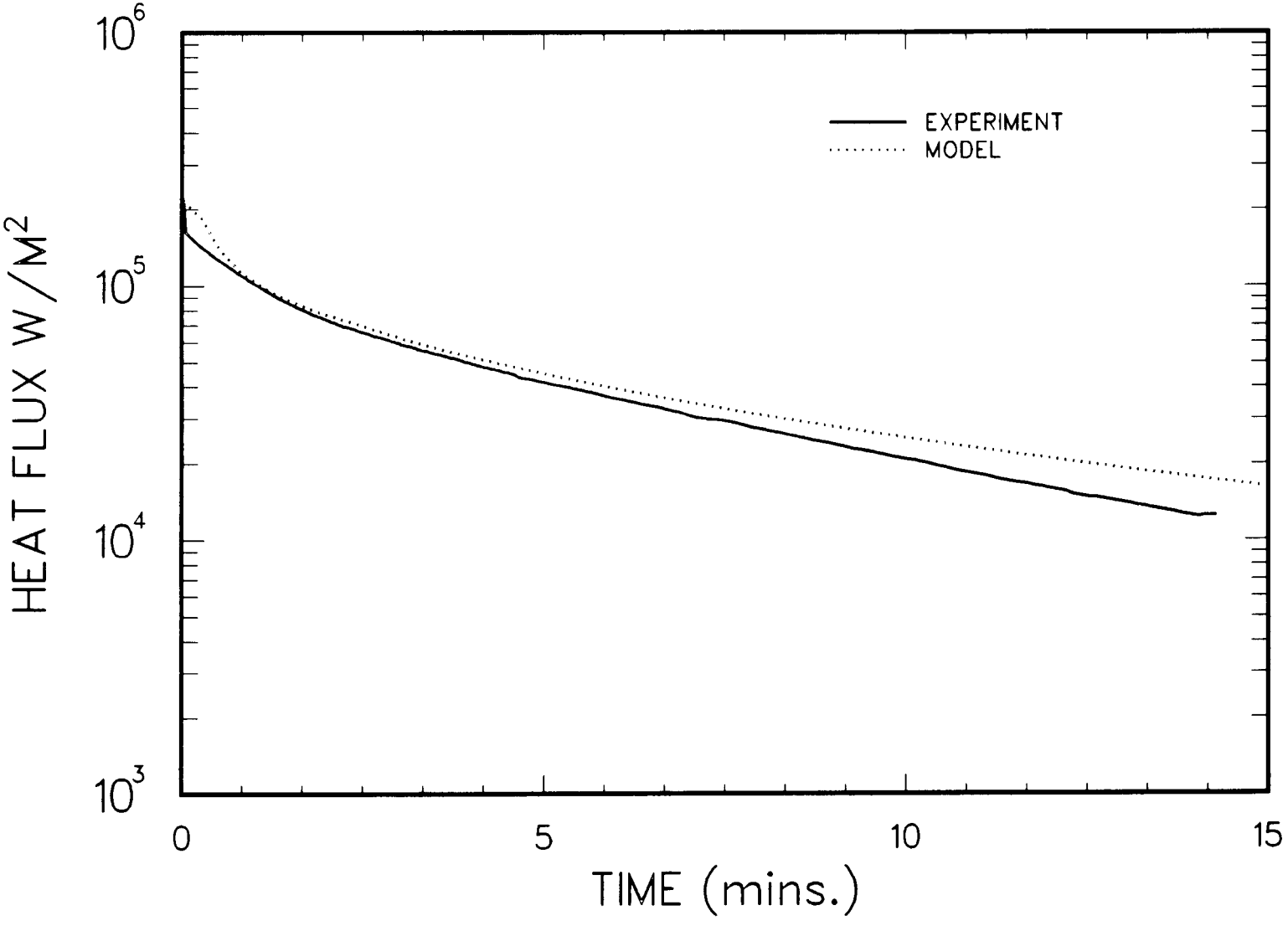

Figure 4.7. Comparison of Predicted and Inferred MgO Wall Heat Flux in the TURC3 Experiment

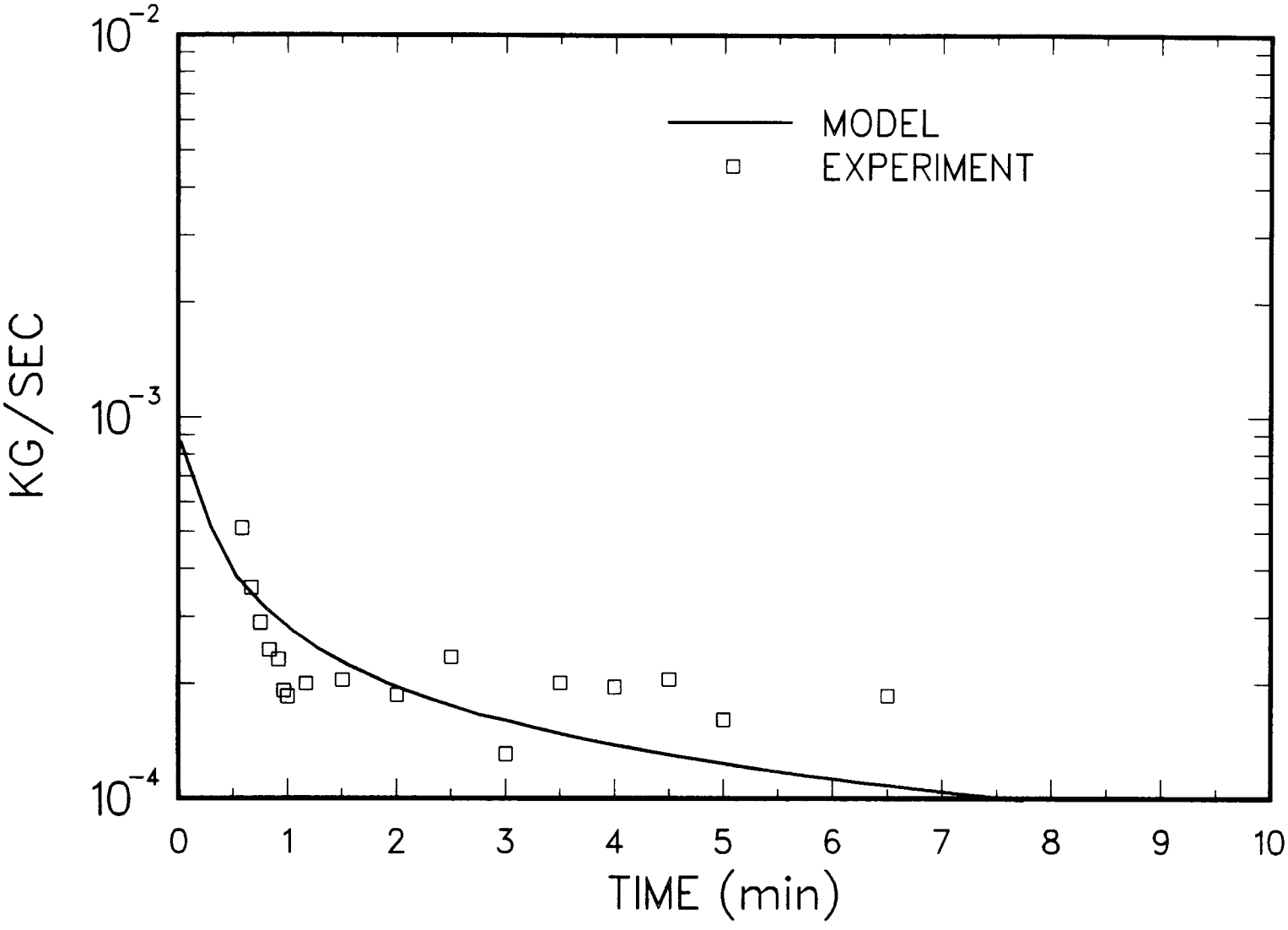

Figure 4.8. Comparison of Predicted and Experimental Data for the Gaseous Carbon Mass Flow in the TURC2 Experiment

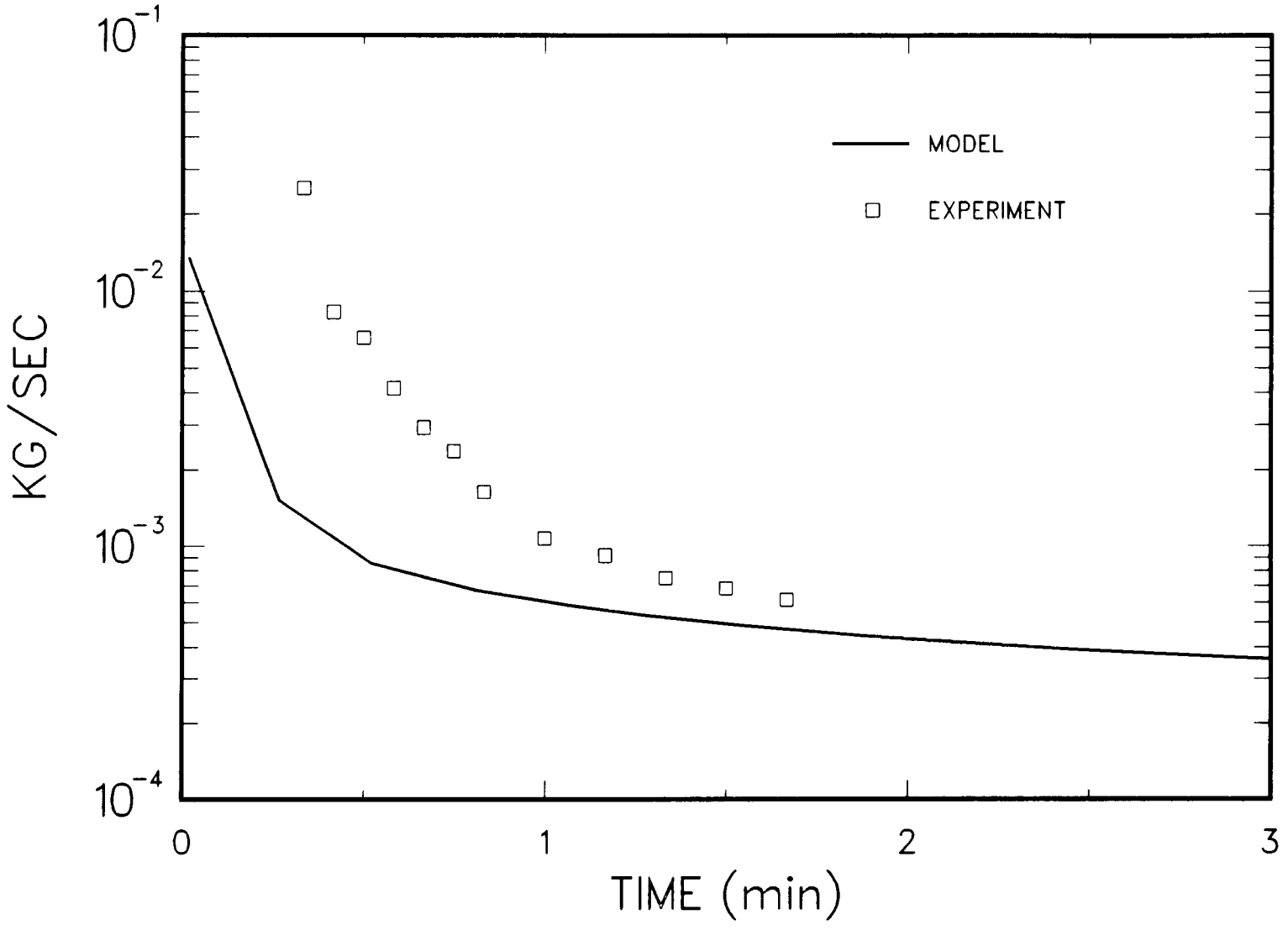

Figure 4.9. Comparison of Predicted and Experimental Data for the Gaseous Carbon Mass Flow in the TURC3 Experiment

experiment as shown in Figure 4.8. However a significant discrepancy between the experimental data and the model prediction is found for the TURC3 experiment as shown in Figure 4.9. The reason for the large discrepancy is not clear. If the experimental data for gaseous carbon mass flow is integrated numerically over the time scales where data was taken, the results of the integration yield a total of 56 grams of carbon in 6.5 minutes for the TURC2 experiment and 814 grams of carbon in 1-1/2 minutes for the TURC3 experiment. The density of carbon in limestone-common sand concrete is 141 kg/m^3. Thus the expected carbonate gas release zone is 3 mm in TURC2 and 4.5 cm in TURC3. In order for the limestone aggregate to release CO_2 gas it must reach a temperature of approximately 1200 K. By examining the thermocouple traces for the TURC3 experiment (Figures 3.20, 3.21, and 3.22) it is quite clear that the large quantity of carbon measured in the TURC3 experiment did not come from the concrete. Whether the large carbon source is due to an error in instrumentation or the presence of some organic material in the crucible cannot be determined.

The previous set of figures (4.1 through 4.9) provides some level of validation of the model that was used to analyze these experiments. In addition to the predictions that can be compared to the experimental data the model also provides a significant amount of information that cannot be compared to experimental data.

Figures 4.10 and 4.11 are plots of the total heat losses for the TURC2 and TURC3 experiments. Total heat loss is expressed in kilowatts for each of the four different heat loss mechanisms. As can be seen from the figures all of the predicted heat losses are of the same order of magnitude at very early times. Figures 4.12 and 4.13 are the heat fluxes associated with the same heat loss mechanisms.

Figures 4.14 and 4.15 are plots of the effective heat transfer coefficient between the bulk pool and the concrete surface. Figure 4.15 is valid for the centerline of the crucible only. At distances closer to the sidewalls in the TURC3 experiment a significant heat transfer resistance must be added in series with the heat transfer coefficient shown in order to match the thermocouple traces.

Figures 4.16 and 4.17 are plots of the predicted ablation rate for the TURC2 and TURC3 experiments. The maximum predicted rate of ablation is approximately 6 cm/hr which lasted for a short time. The temporal decrease in melting rate was due to crust buildup which inhibited efficient heat transfer to the surface. In the TURC2 experiment the ablation is delayed for about 20 seconds. During this time the concrete interface temperature is below its melting point due to the combined effects of transient conduction and heat absorbtion due to CO_2 and H_2O gas generation. The delay in ablation is much shorter (<1 sec)

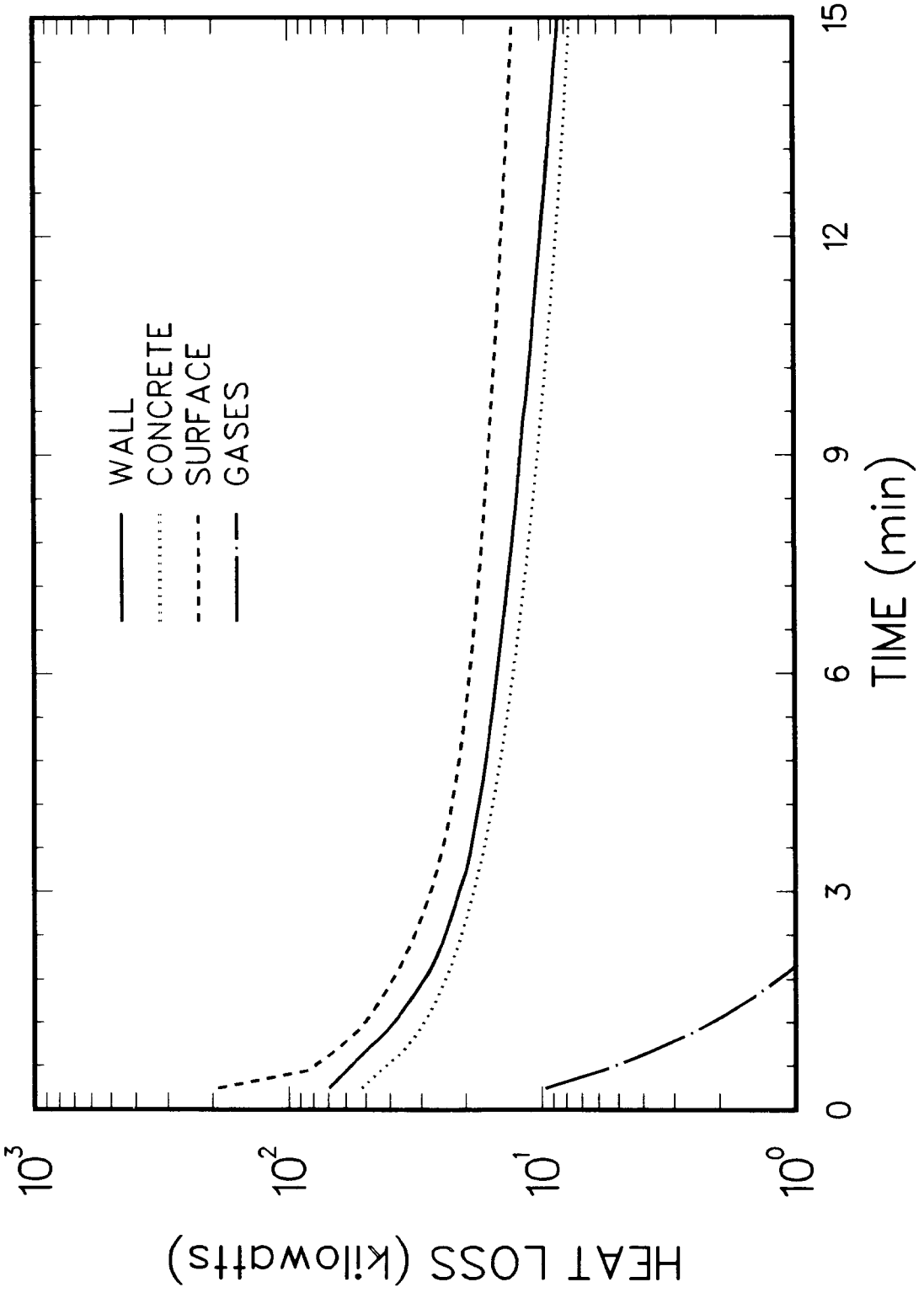

Figure 4.10. The Predicted Total Heat Losses in the TURC2 Experiment

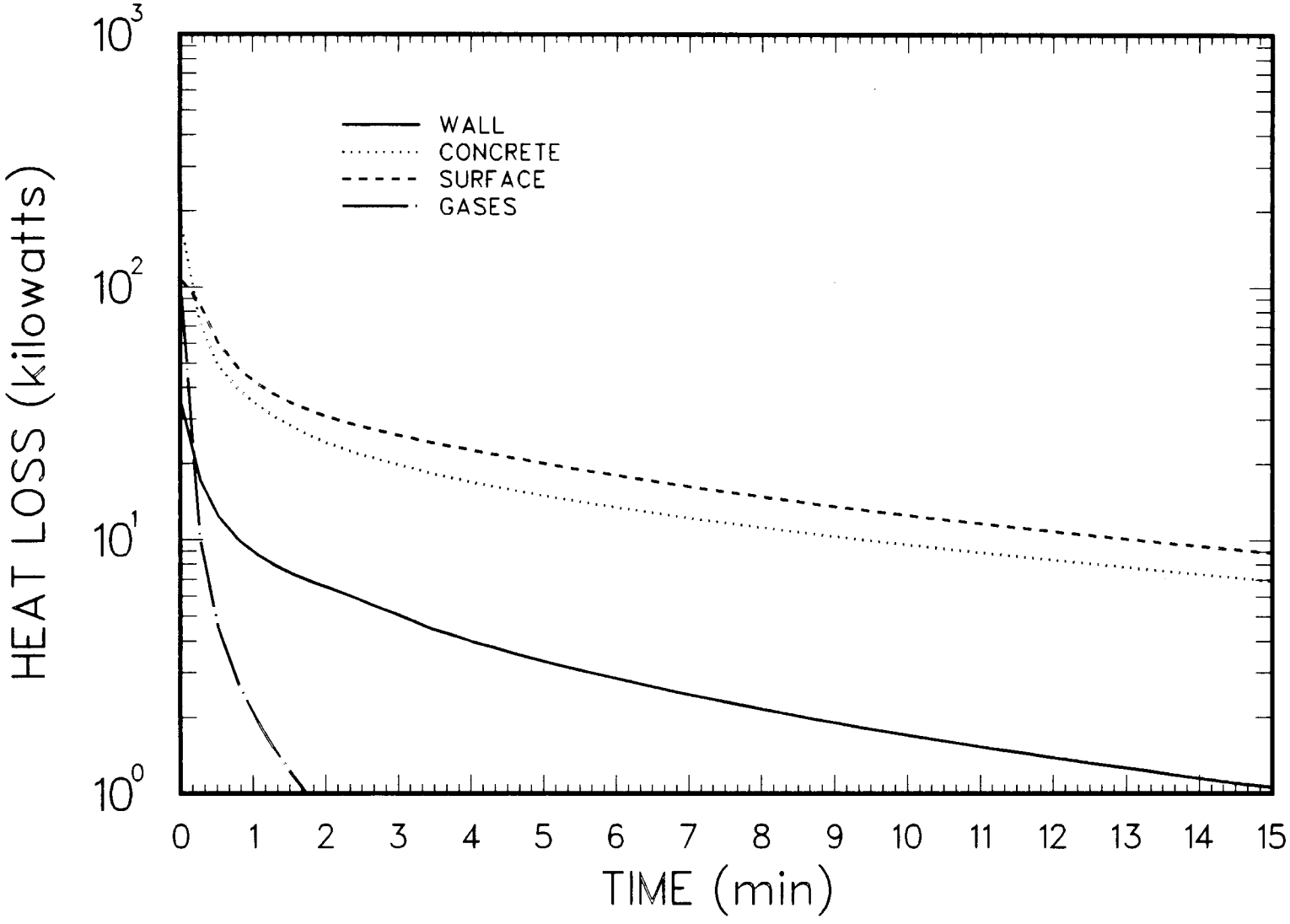

Figure 4.11. The Predicted Total Heat Losses in the TURC3 Experiment

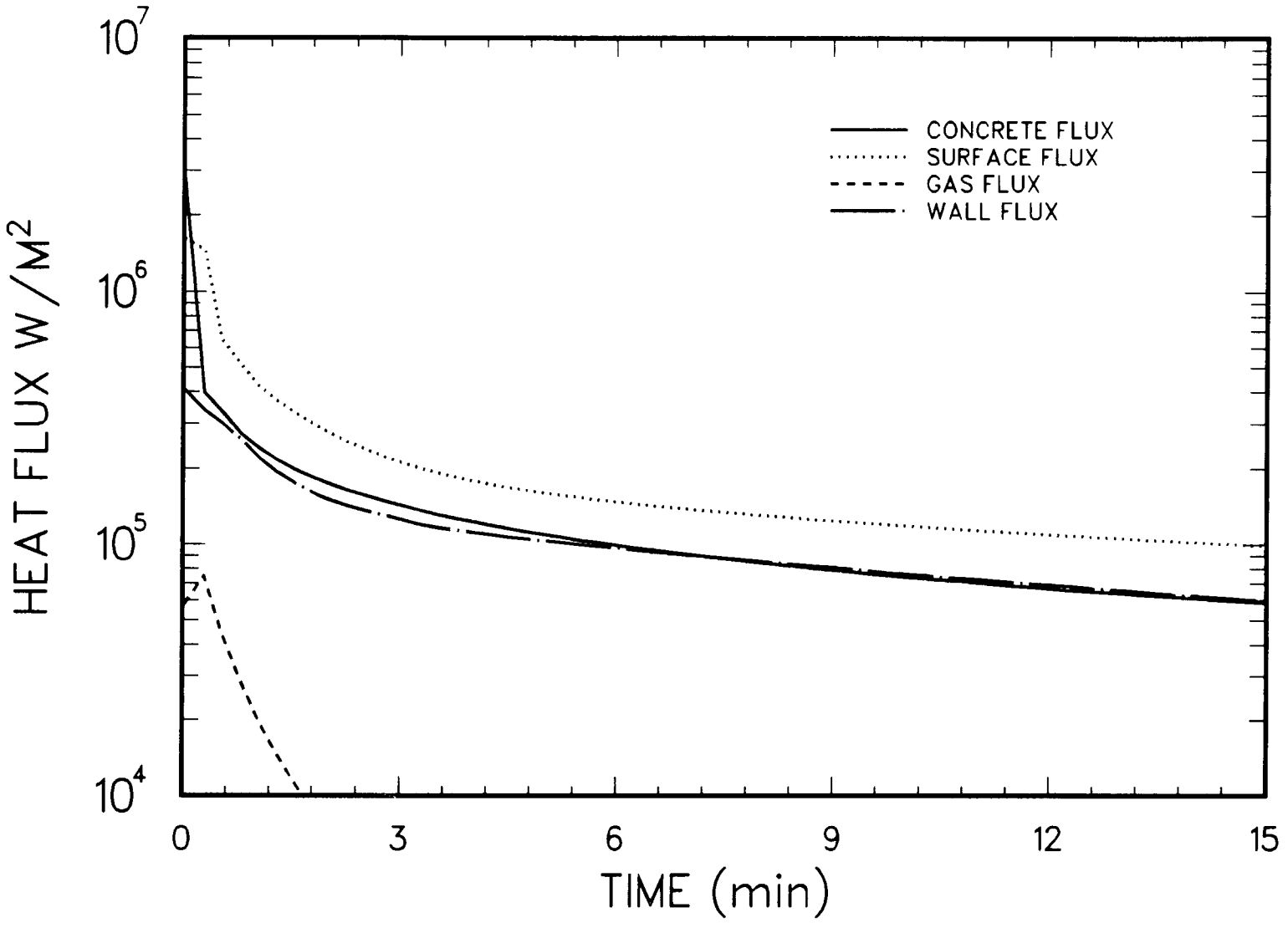

Figure 4.12. The Predicted Heat Fluxes in the TURC2 Experiment

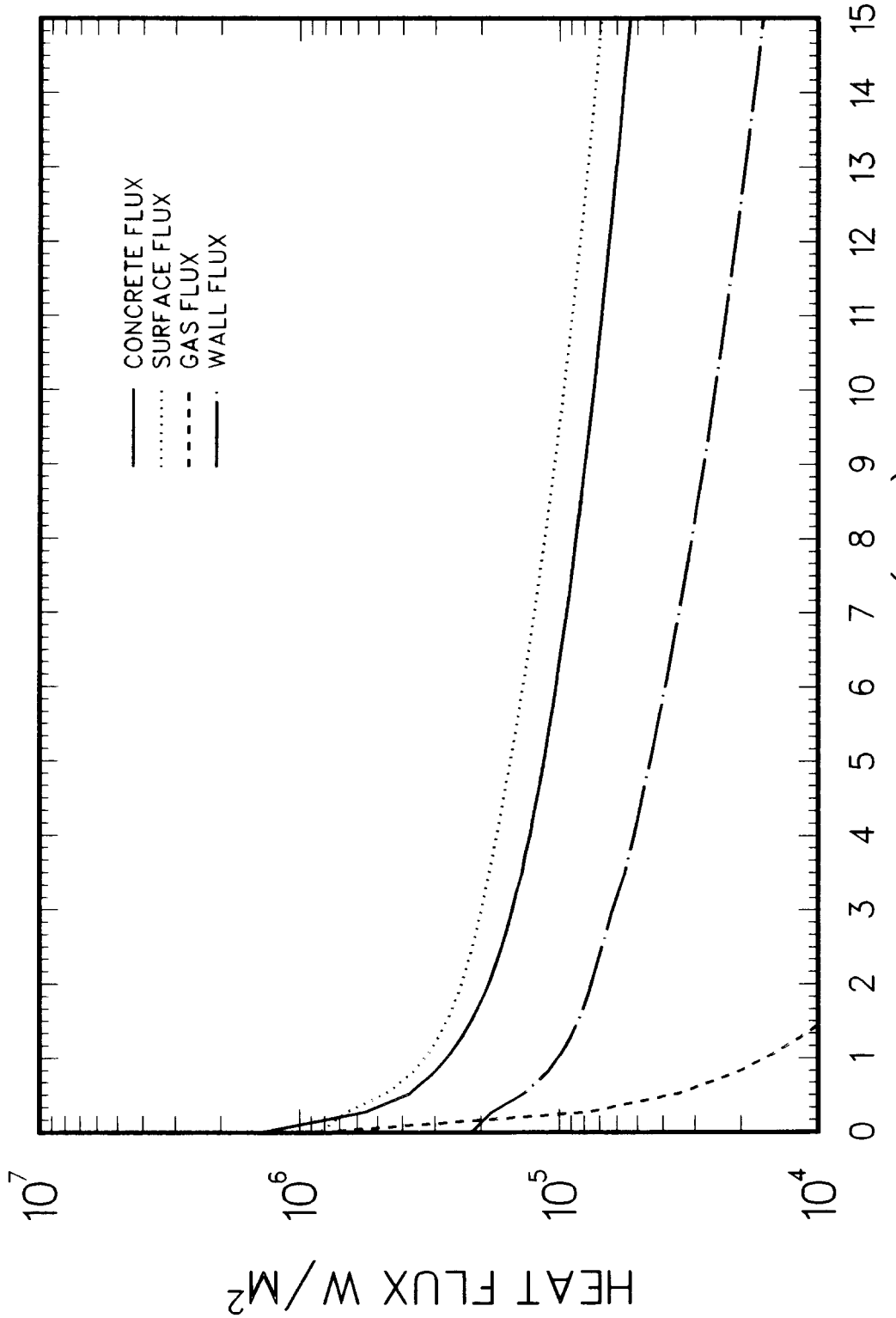

Figure 4.13. The Predicted Heat Fluxes in the TURC3 Experiment

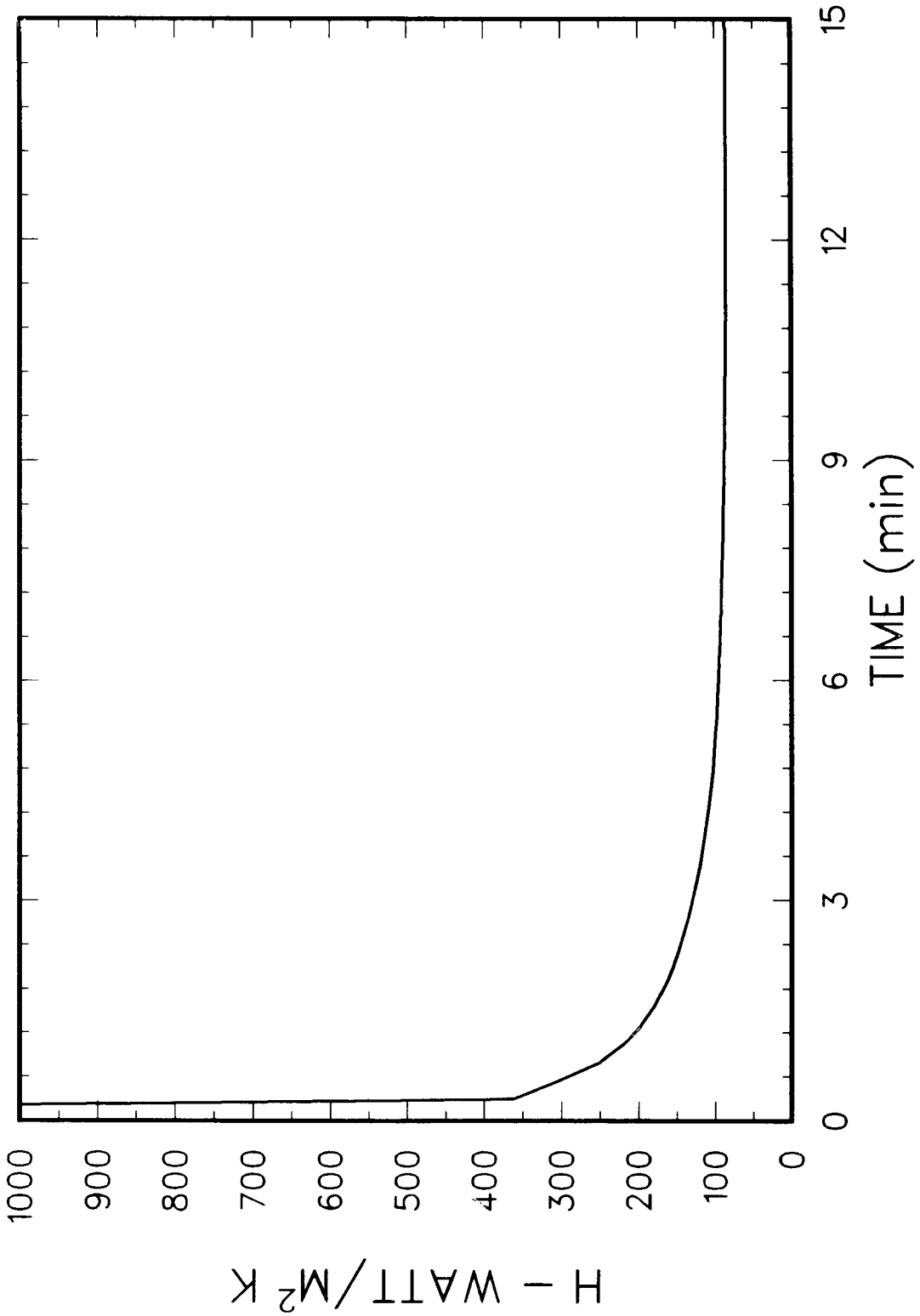

Figure 4.14. The Predicted Effective Bulk Pool to Concrete Surface Heat Transfer Coefficient at the Concrete Centerline in the TURC2 Experiment

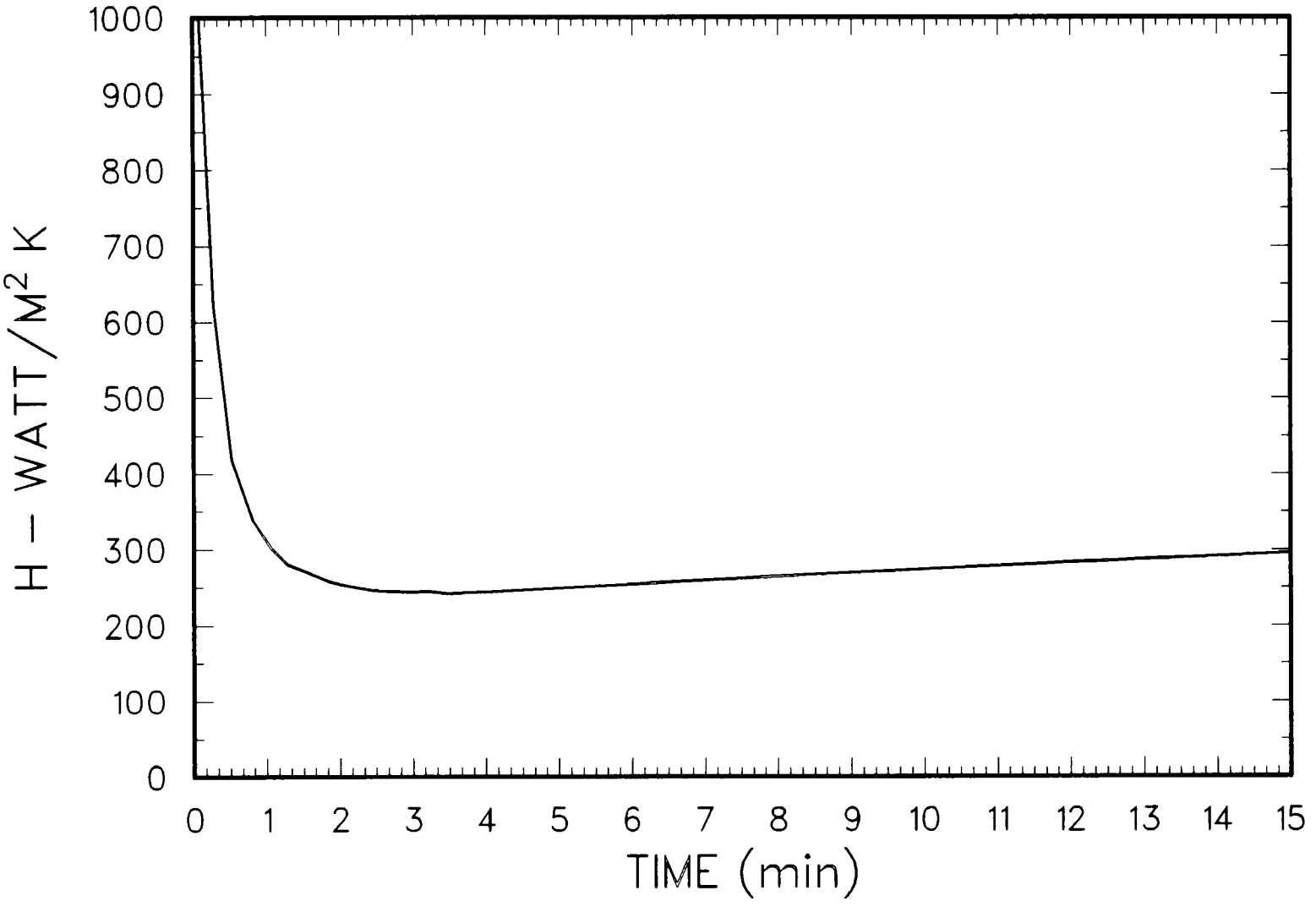

Figure 4.15. The Predicted Effective Bulk Pool to Concrete Surface Heat Transfer Coefficient at the Concrete Centerline in the TURC3 Experiment

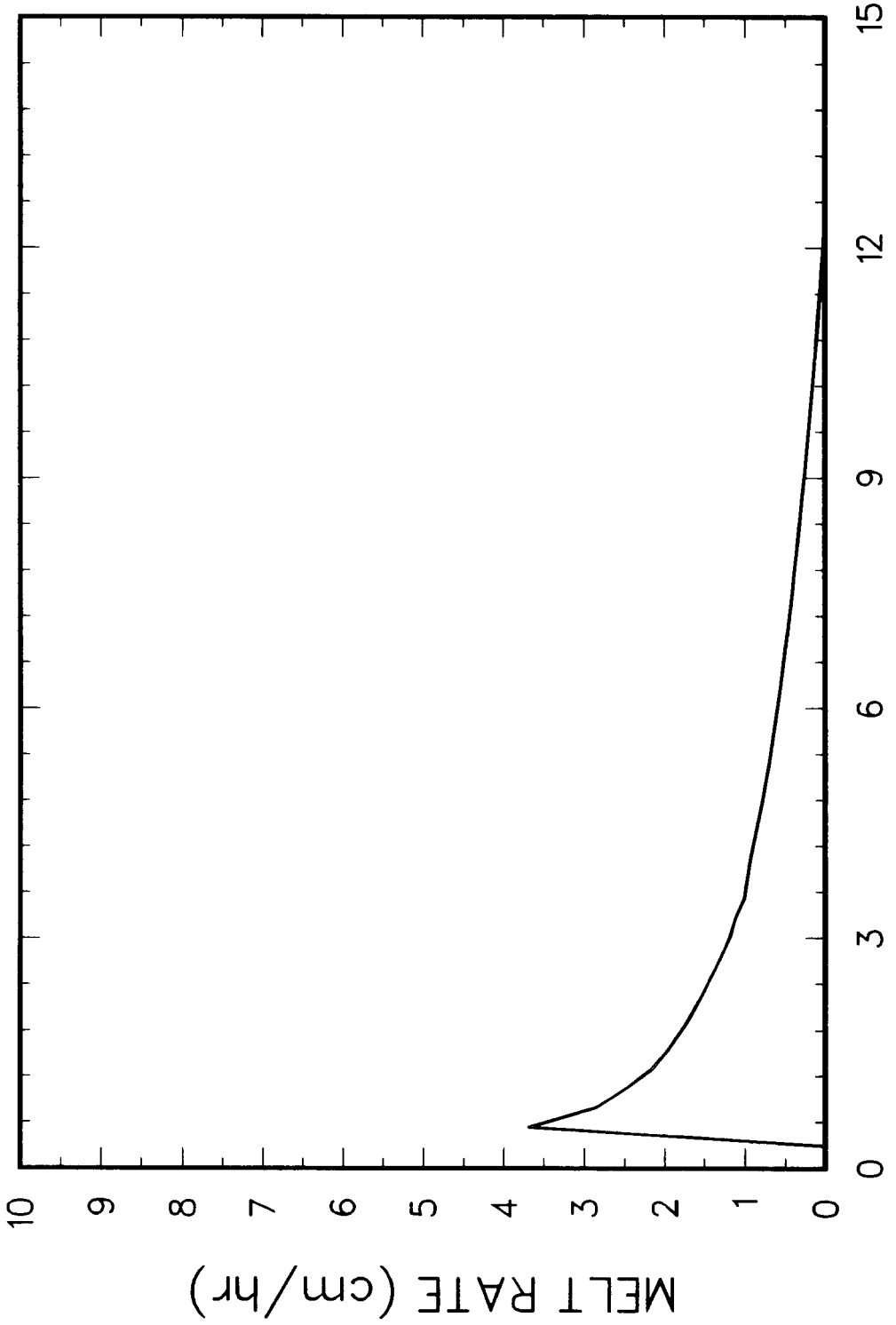

Figure 4.16. The Predicted Ablation Rate in the TURC2 Experiment

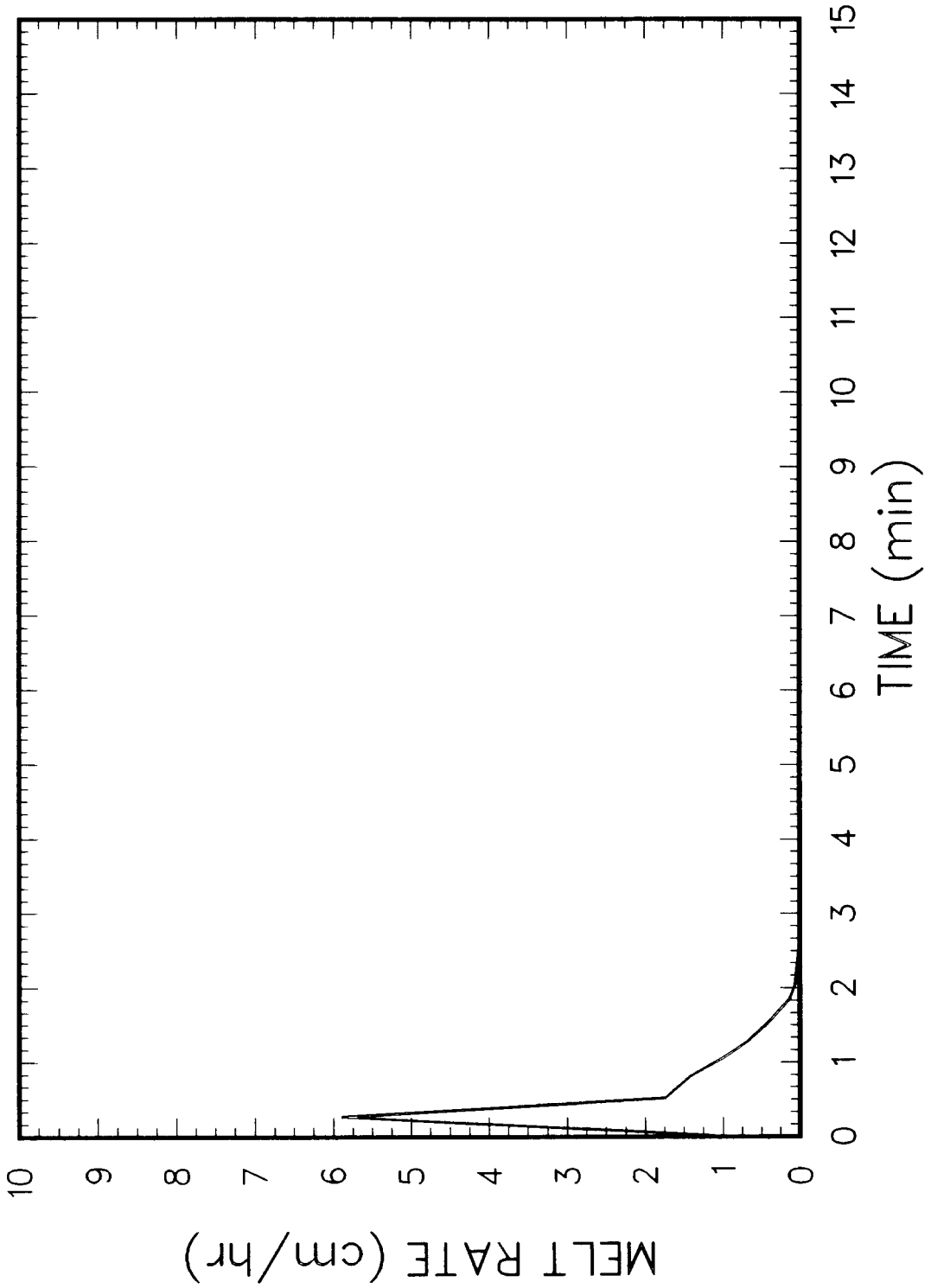

Figure 4.17. The Predicted Ablation Rate in the TURC3 Experiment

in the TURC3 test because the zirconium metal generates a significant amount of heat at the concrete interface when reacting with the evolved gases. The heat generation due to chemical reaction in the TURC3 test offsets the heat absorbed by gas generation and thus allows the temperature of the concrete interface to reach its melt point in a much shorter time.

Figures 4.18 and 4.19 are plots of the predicted melt pool temperature as a function of time. The initial plateaus correspond to the freezing of the melt pool. TURC2 took significantly longer to freeze because of its larger melt mass. The predictions shown here are for temperatures in the central region of the melt pool. Significant thermal gradients do exist in the melt pool while it is freezing (the solidified UO_2 would be at a significantly lower temperature). The fraction of the melt pool mass that is frozen is shown in Figures 4.20 and 4.21. These correspond quite well with the temperature plateaus in Figures 4.18 and 4.19.

As explained earlier, a significant heat transfer resistance was predicted to exist between the UO_2 crust growing on the wall and the wall itself. Figures 4.22 and 4.23 are plots of the predicted surface temperatures of the gap separating the wall UO_2 crust and the MgO wall. As can be seen, in both experiments a very large temperature difference is predicted, most often exceeding 1000 K.

Figures 4.24 and 4.25 are the predicted gas velocities and mass fluxes entering the melt pool for the TURC2 and TURC3 experiments. At early times the superficial gas velocity was a fraction of a meter per second. Apparently this is not a high enough gas velocity to keep any crust that forms in a disrupted state. If it were, a measurable amount of ablation should have occurred.

In summary the model has produced predictions that agree with the experimental data. The model predicts minimal erosion with rapid crusting. Significant thermal resistances were predicted to exist radially outward from the centerline of the concrete slug in the TURC3 experiment and up the MgO sidewalls in both the TURC2 and TURC3 experiments.

4.4 Analysis of Aerosol Data from TURC2 and TURC3

These experiments have yielded experimentally determined aerosol mass source rates, aerosol size distributions and elemental release rates for elements of interest (Table 4.4).

The aerosol mass source rates are calculated by multiplying the measured aerosol concentrations by the exhaust gas flow rates. Delay times for the released aerosol to flow from the melt surface to the sampling point have been taken into account by calculating the time to flow through the intervening volume.

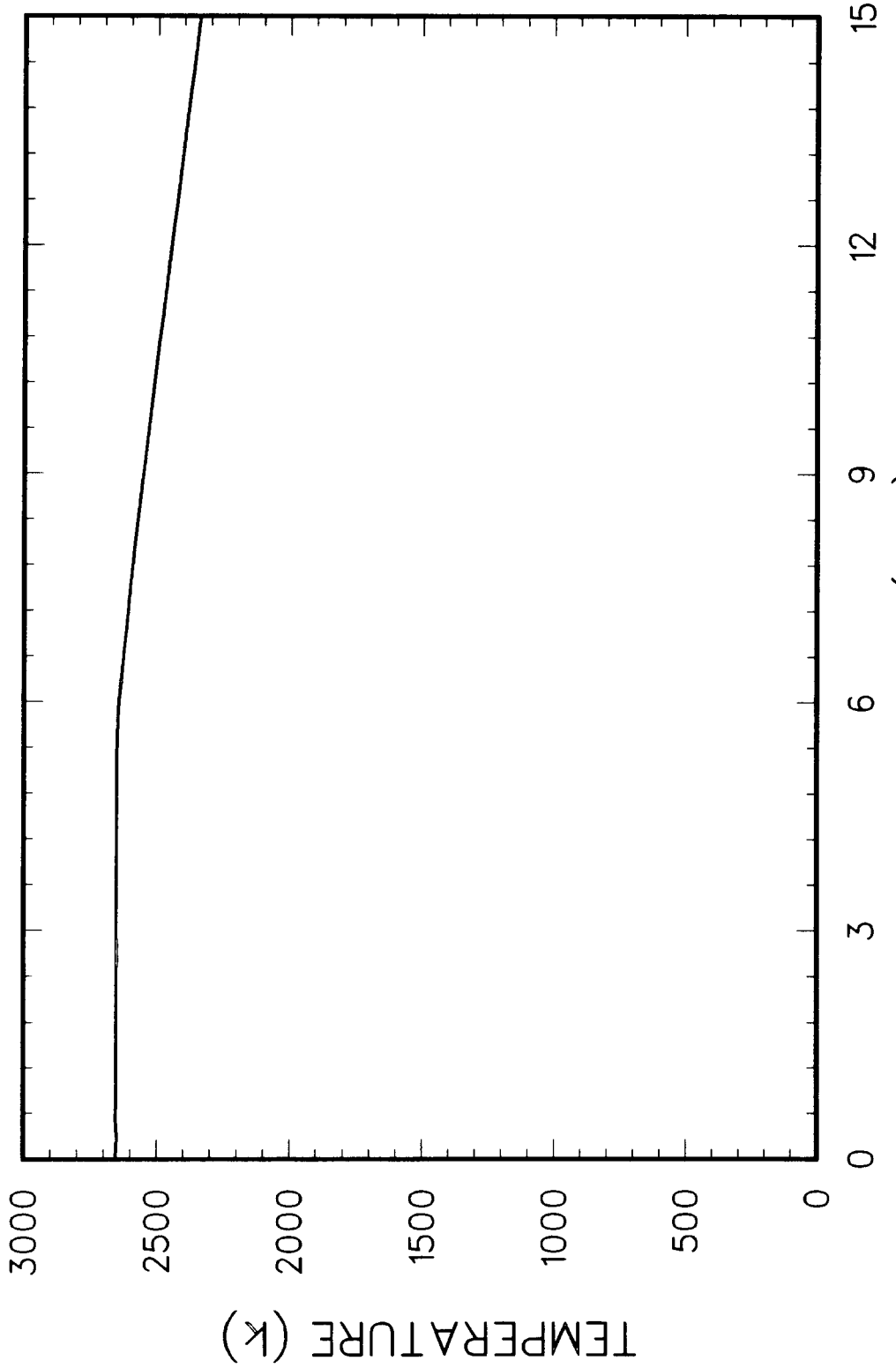

Figure 4.18. The Predicted Bulk Pool Temperature in the TURC2 Experiment

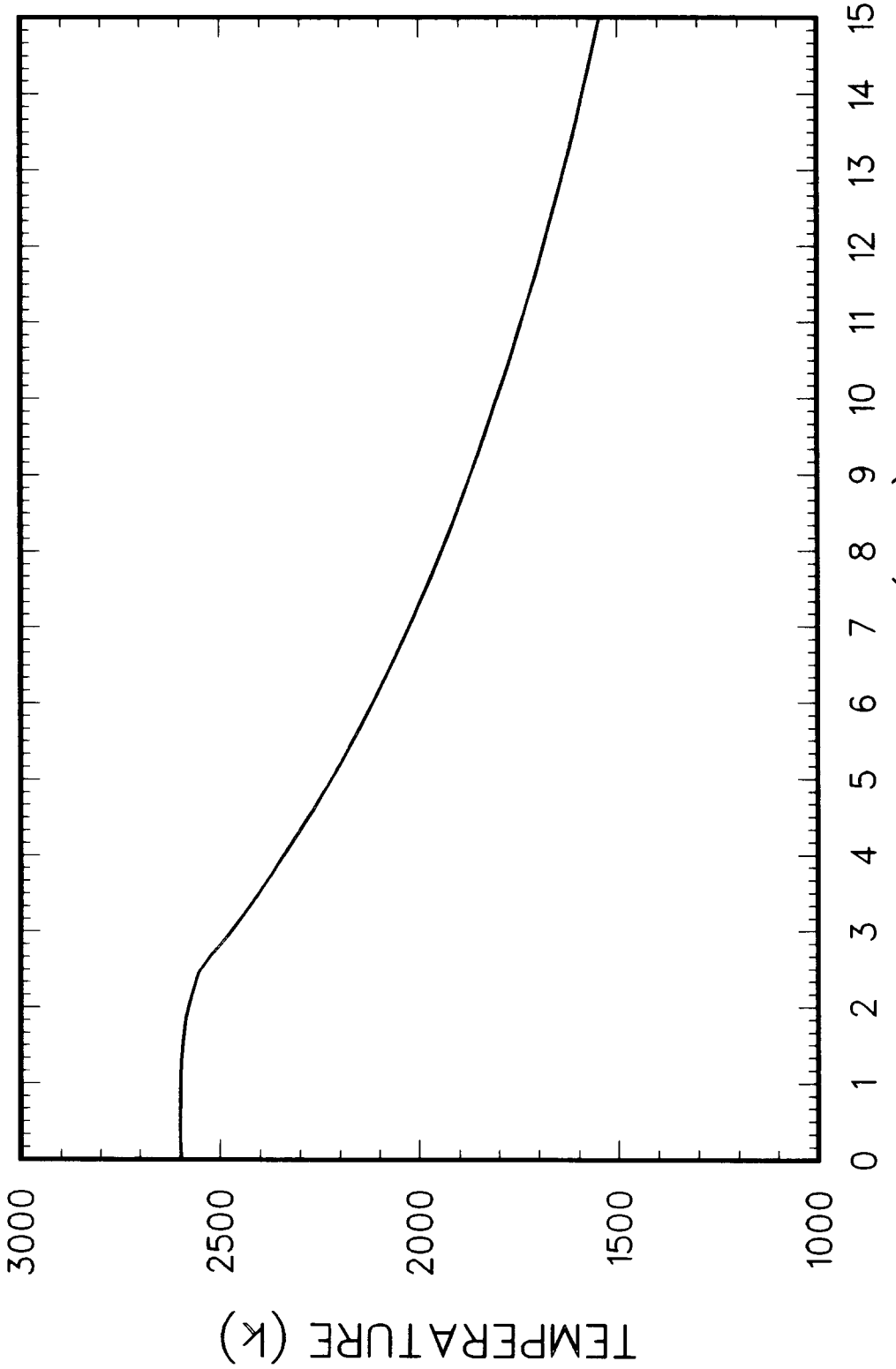

Figure 4.19. The Predicted Bulk Pool Temperature in the TURC3 Experiment

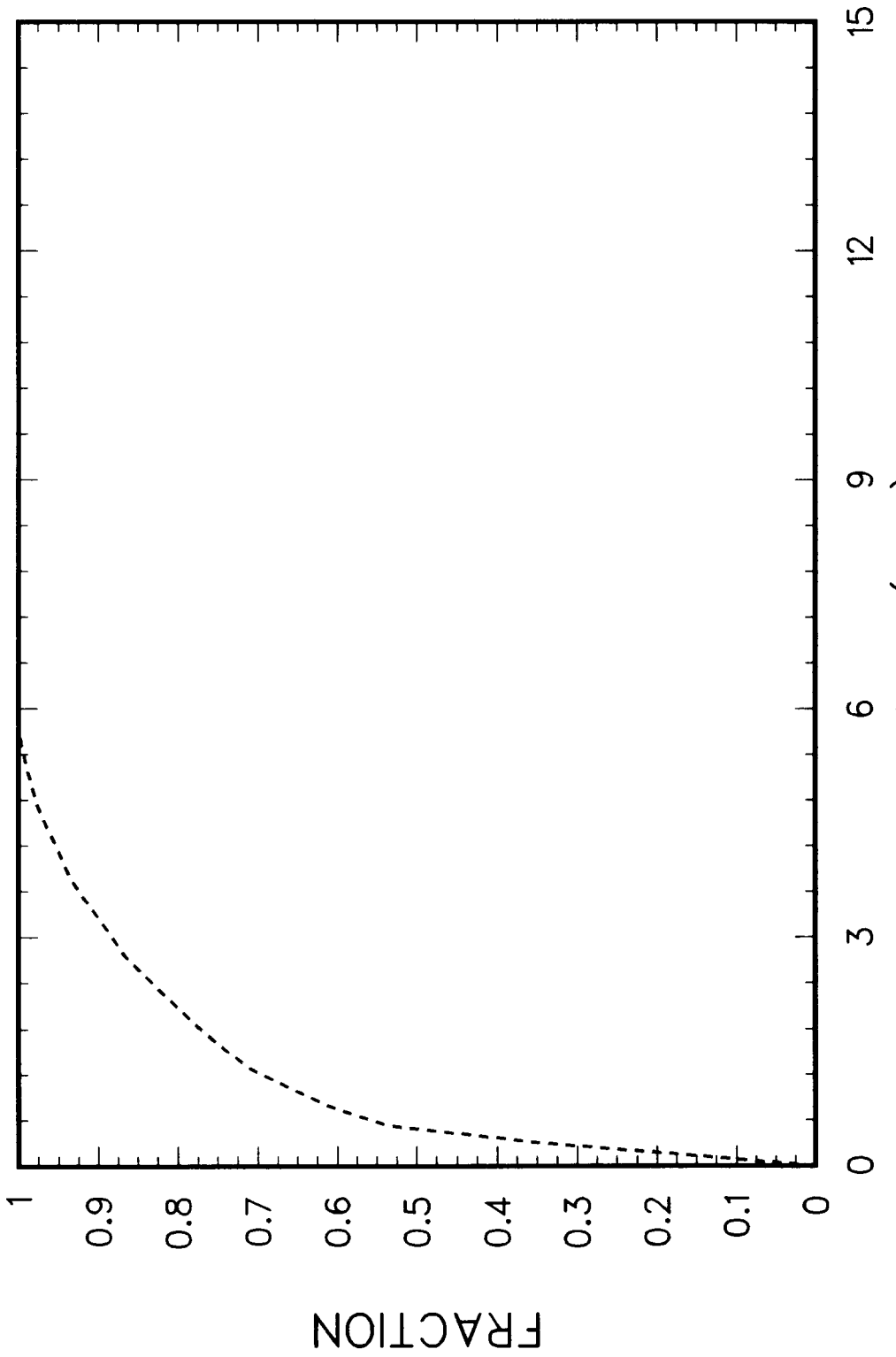

Figure 4.20. The Predicted Fraction of Frozen Material in the Melt Pool for the TURC2 Experiment

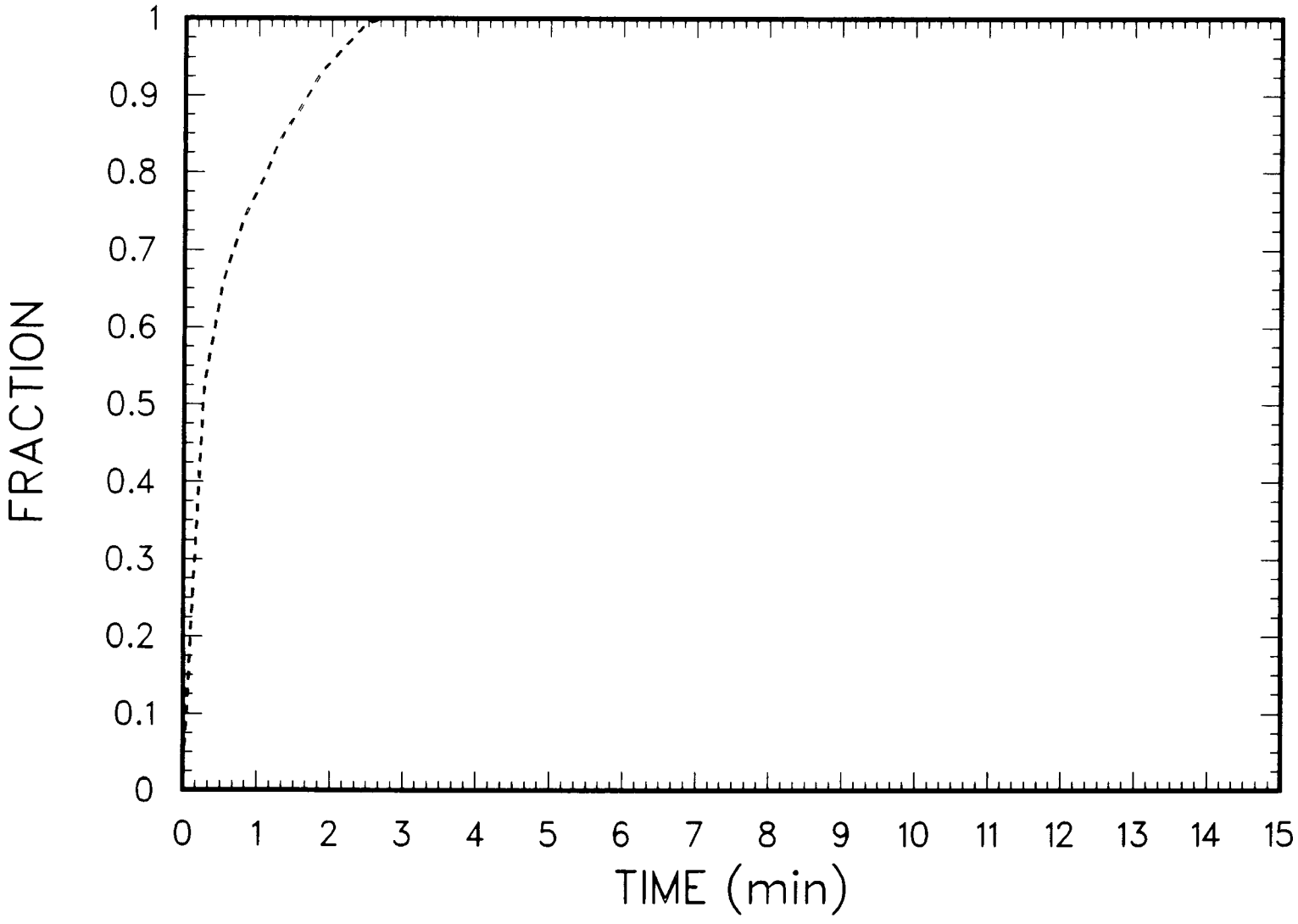

Figure 4.21. The Predicted Fraction of Frozen Material in the Melt Pool from the TURC3 Experiment

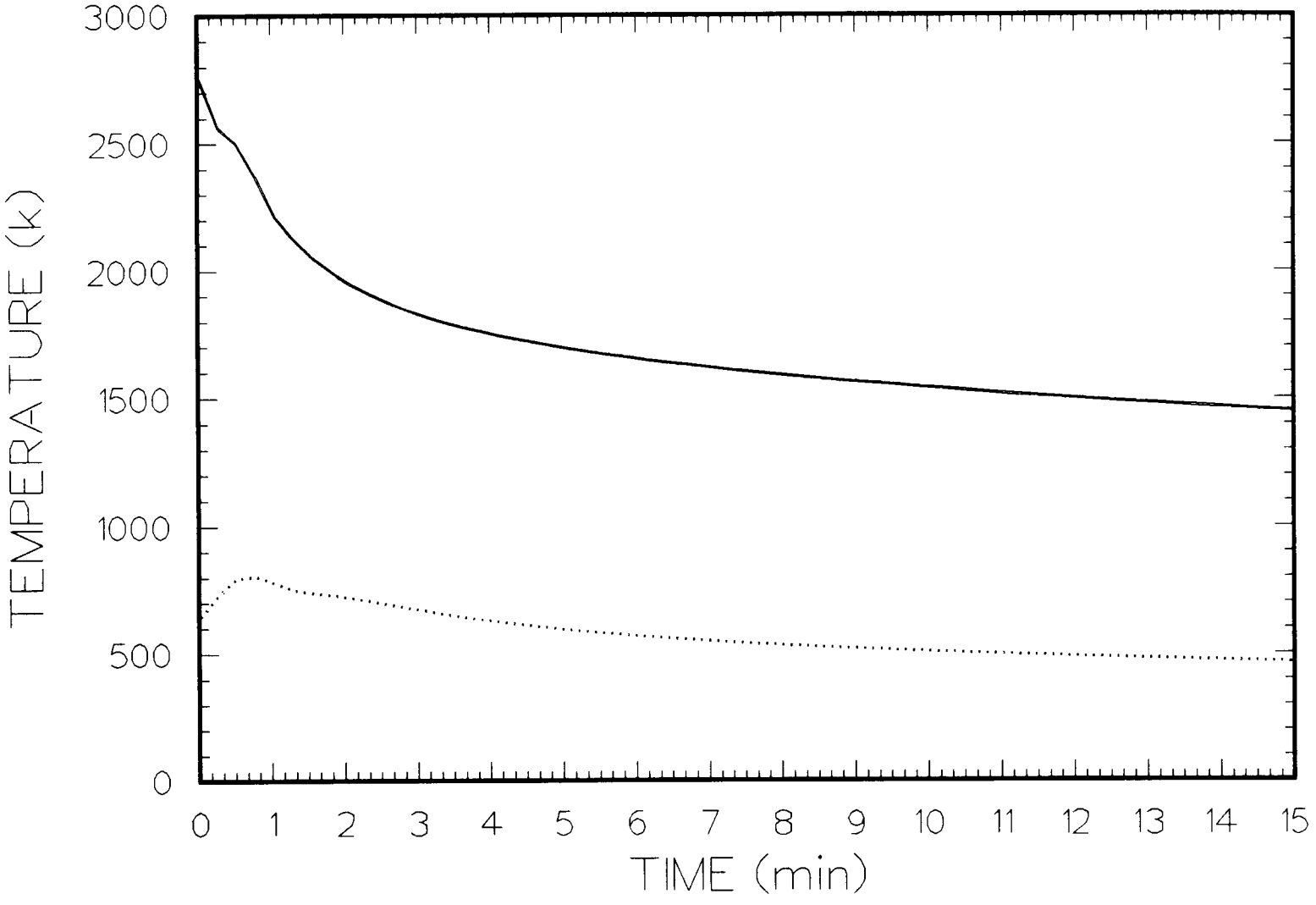

Figure 4.22. The Predicted Wall Gas Gap Temperatures in the TURC2 Experiment

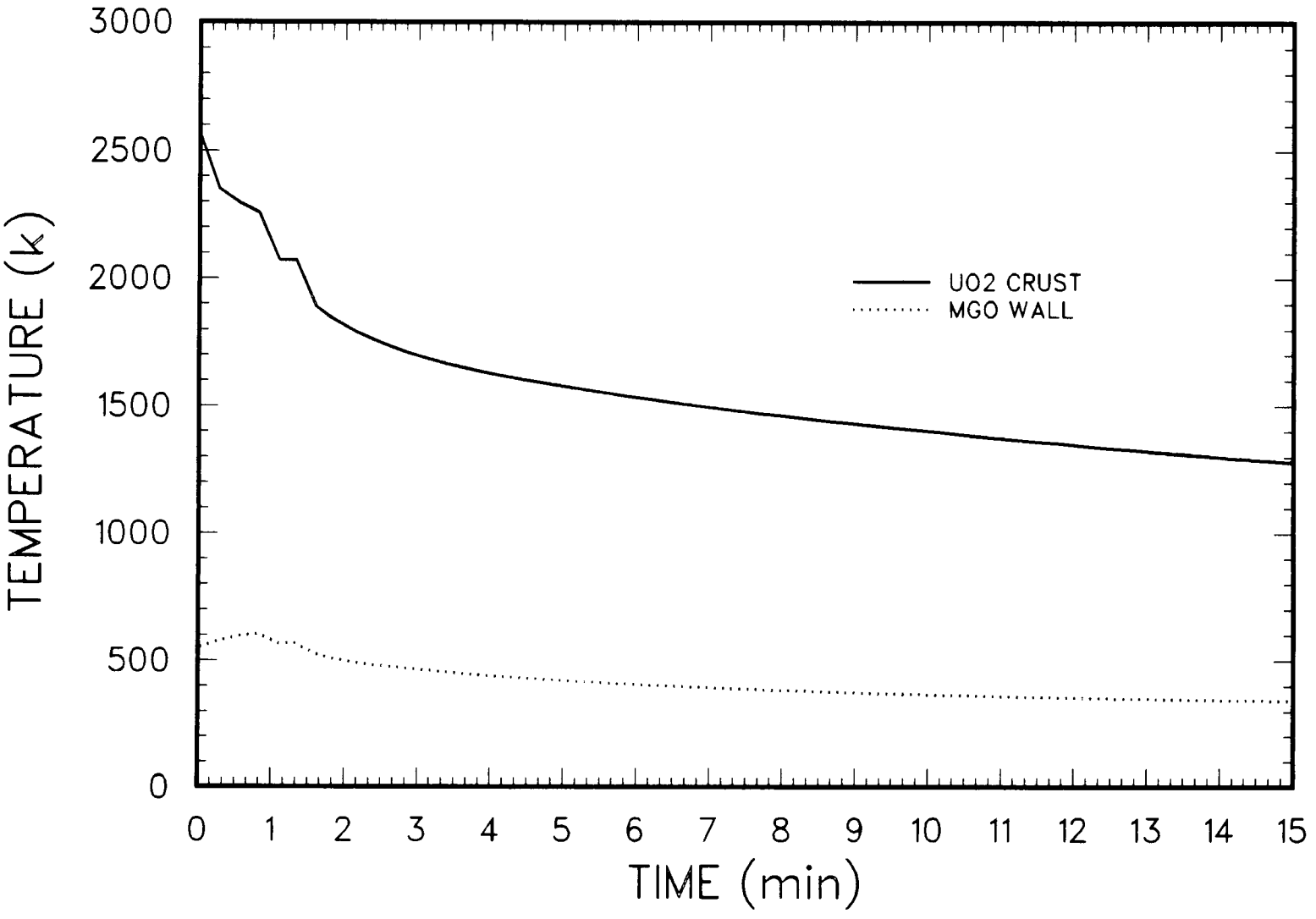

Figure 4.23. The Predicted Wall Gas Gap Temperatures in the TURC3 Experiment

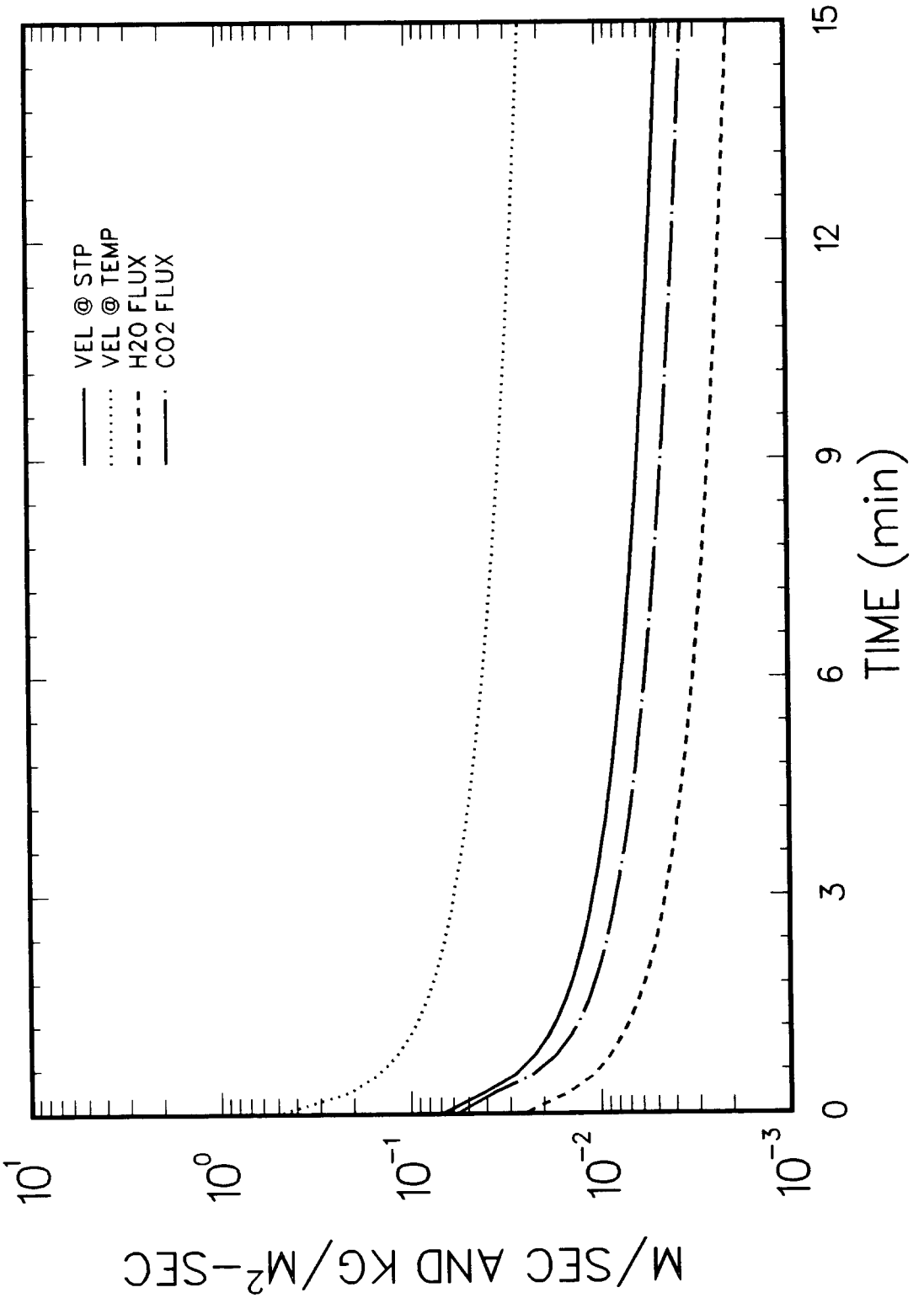

Figure 4.24. The Predicted Gas Velocities and Mass Fluxes in the TURC2 Experiment

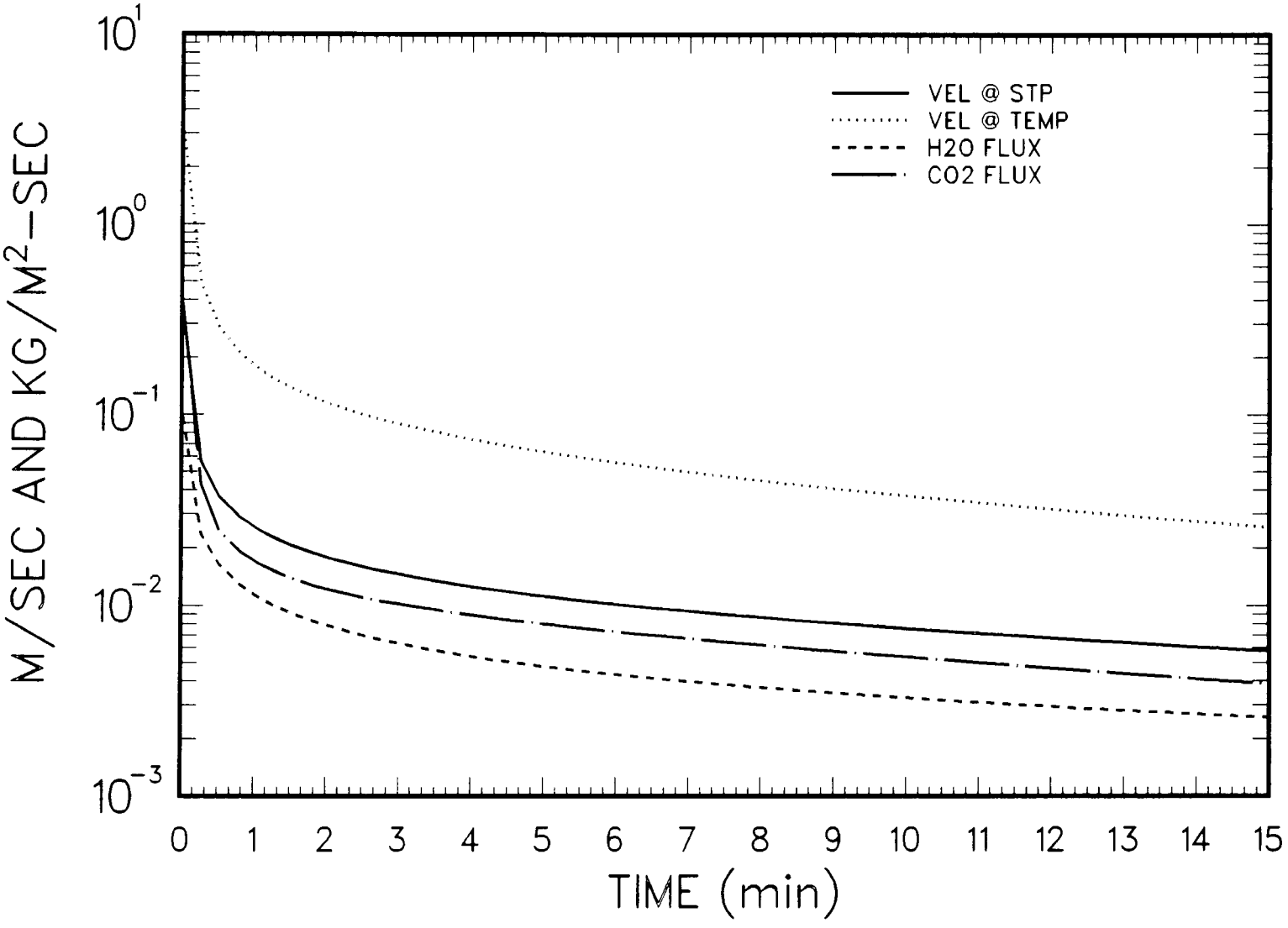

Figure 4.25. The Predicted Gas Velocities and Mass Fluxes in the TURC3 Experiment

Particle losses have been estimated for inertial deposition diffusive deposition, thermophoretic deposition, and particle settling. The source term at the sampling point and sampling times have been adjusted for estimated loss and delay time.

The flow delay time calculation assumes incompressible flow, negligible pressure drop along the flow paths, uniform conditions within a volume element, and that steady state treatment applies. The following backward calculation scheme is employed.

$$Q_{i-1,j} = \frac{P_{i,j}\ T_{i-1,j}}{P_{i-1,j}\ T_{i,j}}\ Q_{i,j}$$

where

$Q_{i,j}$ is the actual volumetric flow rate through the i^{th} volume element at the time j.

$P_{i,j}$ is the pressure in the i^{th} element at time j

$T_{i,j}$ is the temperature in the i^{th} element at time j.

and

$$\Delta t_{i,j} = V_i/Q_{i,j}$$

where

$\Delta t_{i,j}$ is the transit time or delay time for flow through the i^{th} element at time j.

V_i is the volume of the i^{th} element.

and

$$\Delta t_{tot,j} = \sum_i \Delta t_{i,j}$$

where

$\Delta t_{tot,j}$ is the total delay time at time j.

The calculated exhaust flows are used in this calculation. The element volumes are the crucible at 0.1004 m^3, the exit pipe at 0.0016 m^3, the melt trap at 0.0049 m^3, and the exhaust line at 0.0058 m^3 (Figures 2.15 and 2.16).

Transport losses of particles through the exhaust lines are presented as transport efficiencies. Transport efficiencies are defined as the fraction of material transported through the system. Transport efficiencies are functions of particle size and loss mechanism. Efficiencies are calculated at each time for each loss mechanism in each cell. The total transport efficiency

at a given time is the product of the transport efficiencies for each loss mechanism in each cell.

$$\eta_{TOT}(D_p,\ t_j) = \prod_i \left[\prod_k \eta_{ki}(D_p, t_j)\right]$$

where

$\eta_{TOT}(D_p,\ t_j)$ is the total transport efficiency as a function of particle size, D_p, at time t_j.

$\eta_{ki}(D_p, t_j)$ is the transport efficiency for the k^{th} mechanism in the i^{th} cell as a function of particle size, D_p, at time t_j.

The integral transport efficiency at time t_j is defined as

$$\eta_{INT_j} = \frac{\int m(D_p)\ \eta_{TOT}\ (D_p, t_j)\ dD_p}{\int m(D_p)\ dD_p}$$

where

$m(D_p)$ is the mass distribution of aerosol.

The relation between measured aerosol mass source rate $\dot{m}_{mj}$, at the sampling point at time j, and the actual aerosol mass source rate, $\dot{m}_j$, is

$$\dot{m}_{mj} = \dot{m}_j \cdot \eta_{INTj} .$$

In calculating the integral transport efficiency, we have assumed a single mode lognormal aerosol distribution with a geometric mass mean aerodynamic diameter, DGM, of one micrometer and a geometric standard deviation, σ_g, of two. The distribution is expressed as

$$\frac{dM}{dD_p} = \frac{MT}{D_p\sqrt{2\pi}\ \ln\sigma_g} \exp\left[\frac{-\left(\ln\left(DGM/D_p\right)\right)^2}{2\left(\ln\sigma_g\right)^2}\right]$$

where

dM is the differential mass of aerosol contained in the interval D_p to $D_p + dD_p$ and

MT is the total aerosol mass in the distribution

This distribution is an adequate representation of the measured size distributions in TURC2 and TURC3.

Transport efficiencies are calculated for laminar or turbulent tube flow. The mechanisms are gravitational settling, diffusion, thermophoresis, inertial deposition in bends, and, for turbulent flow, turbulent inertial deposition.

The settling velocity is calculated by the well-known expression[20]

$$h_{set} = \frac{\rho_p g D_p^2 C(D_p)}{18\mu}$$

where

h_{set} is the settling velocity

g is acceleration of gravity

D_p is the particle diameter

ρ_p is the particle material density

$C(D_p)$ is the slip correction

μ is the gas absolute viscosity

The settling velocities for the assumed distribution are calculated for each cell at each time to give an estimate for settling losses. It is adjusted appropriately to reflect that deposition from this mechanism is in the downward direction only.

In the case of turbulent flow in a horizontal tube, settling loss is assumed to occur from a well-mixed volume through the boundary layer. Efficiency is expressed as

$$\eta\ (D_p) = \left[- \frac{dL\ h_{set}}{Q} \right]$$

where

d is pipe diameter,

L is pipe length, and

Q is volumetric flow.

In the laminar flow case a different approach is used. The radial velocity profile is ignored in this estimate and settling from the entire cross section of the horizontal tube is assumed. A particle must settle to the lower half of the pipe to be lost.

A strictly geometric argument is used in this estimation. The distance a particle settles during the transit time through the tubes, divided by the tube diameter, d, is the parameter of interest. If s/d is greater than or equal to one, no particles are transported and efficiency is zero. The expression of transport efficiency for gravitional settling in laminar tube flow is

$$\eta(D_p) = \frac{2}{\pi}\left[\arccos\ (s/d) - (s/d)\left(1 - (s/d)^2\right)^{1/2}\right]$$

Gravitational deposition is calculated for horizontal tubes only.

The deposition velocity for particle diffusion loss to the walls is calculated from

$$h_{diff} = \frac{Sh \cdot D}{d}$$

where

h_{diff} is deposition velocity from diffusion

Sh is the Sherwood number

D is the particle diffusion coefficient

d is the tube diameter

The expression for Sherwood number is[21]

$$Sh = 3.66 + \frac{0.0668\ (d/L)\ Re\ Sc}{1 + 0.04\left[(d/L)\ Re\ Sc\right]^{2/3}}$$

for laminar flow and

$$Sh = 0.0118\ Re^{7/8}\ Sc^{1/3}$$

for turbulent flow[20]

where

Sh = Sherwood Number = $\left(\frac{hd}{D}\right)$

Re = Reynolds Number = $(4Q/\pi\nu d)$

Sc = Schmidt Number = (ν/D)

d = tube diameter

L = tube length

ν = kinematic gas viscosity

D = particle diffusion coefficient

Q = volumetric flow

The particle diffusion coefficient is calculated from

$$D = kTB$$

$$B = \frac{C(D_p)}{3\pi\mu\ D_p}$$

$$C(D_p) = 1 + \frac{2\lambda}{D_p}\left[1.257 + 0.4\ \exp\left[-\frac{0.55}{\lambda}\ D_p\right]\right.$$

$$\lambda = \nu\left[\frac{\pi m}{2kT}\right]^{1/2}$$

where

k is Boltzmann's constant

B is particle dynamic mobility

C is the slip correction

μ is the absolute gas viscosity

D_p is particle diameter

λ is gas mean free path

m is the molecular weight of the gas

The transport efficiency is calculated from

$$\eta = \exp\left[\frac{-\pi dL\ h_{diff}}{Q}\right]$$

This expression for the laminar flow case gives very good agreement with the solution of Gormley and Kennedy.[22] For diffusion loss in laminar tube flow

$$\xi = \frac{\pi dL}{Q}$$

$$\eta = 1 - 2.56\ \xi^{2/3} + 1.2\ \xi + 0.177\ \xi^{4/3}$$

for $\xi < 0.02$

$$\eta = 0.819\ \exp(-3.657\ \xi) + 0.097\ \exp(-22.3\xi) + 0.032\ \exp(-57\xi)$$

for $\xi > 0.02$

Thermophoresis is the transport of a particle by a temperature gradient. A particle in a gas which has a temperature gradient will move down the gradient with a thermophoretic velocity, h_{th}. This would cause deposition of particles in a hot gas to a cool wall.

This thermophoretic velocity is constant for particles much larger than the gas molecule mean free path. This is for continuum regime particles and is expressed as[20]

$$h_{th,c} = \frac{2(k_g/k_p)\ k_g\ \nabla T}{5P\ (1 + 2k_g/k_p)}$$

where

$h_{th,c}$ is the thermophoretic deposition velocity,

k_g is the conductivity of the gas,

k_p is the conductivity of the particle material,

P is the pressure, and

∇T is the temperature gradient in the gas.

For particles in the free molecule regime (particle size much smaller than the gas molecule mean free path) the thermophoretic velocity is also constant but expressed as[20]

$$h_{th,fm} = \frac{3\nu\nabla T}{4(1 + \pi(0.9)/8)T}$$

where T is the gas temperature.

Defining the Knudsen number as

$$Kn = 2 \bullet \lambda/D_p$$

allows us to interpolate thermophoretic velocity in the region where particle size is on the order of the mean free path.

$h_{th} = h_{th,c}$ for Kn < 0.1

$h_{th} = h_{th,fm}$ for Kn > 10

$$h_{th} = h_{th,c} + (h_{th,fm} - h_{th,c}) \frac{\ln(10 \cdot Kn)}{\ln(100.)} \quad \text{for } 0.1 < Kn < 10$$

In the case of an agglomerate particle, the particle conductivity is not necessarily the same as the particle material conductivity. To calculate the particle effective conductivity, the simple relation for parallel resistance is used

$$k_{eff} = \left[\frac{(1-\alpha)}{k_g} + \frac{\alpha}{k_p}\right]^{-1}$$

where

k_{eff} is the effective particle conductivity

α is the solid volume fraction of the agglomerate

For a spherical agglomerate, the solid volume fraction, α, and the dynamic shape factor, χ, are related as

$$\alpha = 1/\chi^3$$

Substitution of k_{eff} into the expression for $h_{tn,c}$ gives

$$h_{th,c} = \frac{2(1-\alpha + \alpha\, k_g/k_p)\, k_g\, \nabla T}{5P\, \left(1+2(1-\alpha + \alpha\, k_g/k_p)\right)}$$

or for spherical agglomerates

$$h_{th,c} = \frac{\frac{2}{\chi^3}\left[\frac{k_g}{k_p} + \chi^3 - 1\right] k_g\, \nabla T}{5P\left[1 + \frac{2}{\chi^3}\left[\frac{k_g}{k_p} + \chi^3 - 1\right]\right]}$$

Comparison of k_g/k and k_g/k_{eff} for various values of α is given below. Generally, k_g/k_p ranges from 0.01 to 0.1.

α	χ	k_g/k_{eff}
1	1	0.01 to 0.1
0.512	1.25	0.49 to 0.54
0.296	1.50	0.71 to 0.73
0.125	2.00	0.88 to 0.89

As is seen, if half the particle volume is gas, then the value of k_g/k_{eff} is closer to 1 and the range of variation is reduced. For our calculations, we have chosen $\chi = 1.5$ (Ref. 23).

The temperature gradient, ∇T, to the wall drives the thermophoretic deposition to the wall. In our treatment of each cell as a tube, the temperature gradient may be calculated from the appropriate Nusselt number and temperature difference to the wall. The Nusselt number may be thought of as the ratio of the characteristic system dimension to the thermal boundary layer thickness. The temperature gradient is approximated by the temperature difference divided by the thermal boundary layer thickness.

$$\delta_{th} = d/Nu$$

$$\nabla T = \Delta T/\delta_{th} = \Delta T \cdot Nu/d$$

where

δ_{th} is the thermal boundary layer thickness

d is the tube diameter

Nu is the Nusselt number

∇T is the temperature gradient

ΔT is the temperature difference.

The expression for Nusselt number is[21]

$$Nu = 3.66 + \frac{0.0668(d/L)\ Re\ Pr}{1 + 0.04\ [(d/L)Re\ Pr]^{2/3}}$$

for laminar flow and

$$Nu = 0.0118\ Re^{7/8}\ Pr^{1/3}$$

for turbulent flow

where

d is the tube diameter

L is the tube length

Re is the tube Reynolds number = $4Q/\pi\nu d$

Pr is the Prandtl number = ν/α

α is the thermal diffusivity of the gas

The expressions for Nu are the same as are used for Sh in the diffusion deposition calculation. The heat-mass transfer analogy is applied.

The transport efficiency for thermophoresis is calculated from

$$\eta = \exp\left[\frac{-\pi dL}{Q} h_{th}\right]$$

The inertial losses of particles traversing a bend in the pipe is estimated in the same way for both laminar and turbulent flow.[24] The Stokes number, Stk, of a particle is the ratio of particle stopping distance to some characteristic system dimension. In the case of tube flow it is

$$Stk = \tau u/d$$

where

τ = particle relaxation time = $\dfrac{\rho_p D_p^2 \cdot C(D_p)}{18\mu}$

u = average velocity in the tube

and efficiency is estimated by

$$\eta = 1 - Stk \cdot \theta$$

where θ is the angle of the bend in radians.

Turbulent inertial deposition occurs when the turbulence in the central region of the pipe flow throws a particle into the laminar sublayer of the turbulent boundary layer. If the particle's inertia is sufficiently high, it will fully penetrate the

sublayer and be collected on the wall. Liu and Agarwal[25] give an empirical relation for the deposition velocity of this mechanism. They relate a dimensionless deposition velocity, v_t^+, to a dimensionless relaxation time, τ^+.

$$v_t^+ = 6.0 \cdot 10^{-4} \ (\tilde{v}+)^2 \quad ; \ \tau^+ < 13.$$

$$v_t^+ = 0.1 \quad ; \ \tau^+ > 13.$$

The friction velocity u* is an important parameter in the dimensionless variables

$$u* = \left[\frac{0.0395}{Re^{1/4}}\right]^{1/2} \cdot u$$

where

u = the average velocity in the tube.

$$\tau^+ = \tau(u*)^2/\nu$$

and the deposition velocity for turbulent inertial deposition, h_t, is

$$H_t = v_t^+ \ u*$$

The efficiency is calculated from

$$\eta = \exp\left[-\frac{\pi dL}{Q} \ h_t\right]$$

The lack of detailed flow and temperature data in the exhaust line does not justify an exhaustive treatment. The following assumptions are made in the loss calculations.

(1) Exhaust flow is taken from the data based on seed flow and gas analysis

(2) The gas temperature is taken as 500 K and the temperature difference to the wall as 100 K

(3) The gas composition is taken as

10% H_2
10% H_2O
25% CO
25% CO_2
25% Ar
5% N_2

by volume

(4) The aerosol size distribution is described as log-normal with geometric mass median aerodynamic diameter of one micrometer and geometric standard deviation of two.

(5) The value of gas conductivity is taken as 3000 erg/sec cm/K, and the value of k_g/k_p as 0.01, and the value of χ as 1.5 for the calculation of thermophoretic deposition.

(6) Four cells are treated. They are

cell	d(cm)	L(cm)	angles
crucible	41.0	80.0	0
line 1	7.6	40.0	0
melt trap	17.8	95.0	0
line 2	7.6	218	90°

The mass source rates are calculated by multiplying the measured aerosol concentration in the exhaust line by the volumetric gas flow through the line. This gives the measured mass source rate at the sample point averaged over the sampling interval. The mass source rate at the melt surface is calculated by applying the loss term. The time interval for the source is calculated by subtracting the delay times from the beginning and end of the sampling time interval.

The gas flow can play a very significant role in the source term calculations, in the loss calculations, and in the delay time calculations. Erroneously high values of gas flow would overestimate the mass source rate and underestimate transport losses and delay time. It is possible that the measured gas flows reported for TURC3 may be too high. If so, the mass source rate would also be too high. The TURC3 data have been reduced with the reported gas flows as well as with the argon purge gas flow alone. The selection of the argon purge gas flow as the total gas flow is because in the TURC2 experiment the total gas flow very quickly dropped to approximately the purge gas flow. Since the experimental behaviors were the same (i.e., rapid crusting) presumably the evolved gas flows would be about the same. The details of delay time and aerosol transport loss have not been included in the second calculation as it is intended to represent a range in mass source rate reflecting the uncertainty in the gas flow in the TURC3 test. Consequently it is depicted in the graphic representation of the TURC3 source term, in Figure 4.27.

Tables 4.2 and 4.3 give the source rates for TURC2 and TURC3 respectively. The times are from the initiation of the melt teem. The mass source is the mass source at the melt surface.

Table 4.2

Aerosol Mass Source Term Measured in TURC2

(Cumulative Release Measured Through Exhaust Line = 11.6 g to 12.9 g)

Time* (sec)	Mass Source Rate** (g/sec)	Aerosol Loss Estimate** %
0-5	0.40 to 0.44	10
5-10	0.26 to 0.29	10
10-15	0.132 to 0.147	10
15-35	0.065 to 0.072	10
35-103	0.051 to 0.057	10
103-165	0.032 to 0.036	10
165-225	0.012 to 0.013	10
284-350	0.003 to 0.0033	10

*Time from initiation of melt teem with source at melt-concrete interaction location

**Range arises from estimates of particle loss during transport from interaction location to sampling point. The loss estimate represents the maximum expected loss employing the method described in the text.

Uncertainty in concentration measurement is about ±13% based on comparison of filter and impactor measurements of concentration. Combined uncertainty in aerosol loss and concentration measurement are ±14%.

Table 4.3

Aerosol Mass Source Term Measured in TURC3

(Cumulative Release Measured Through Exhaust Line = 40 g to 44 g)

Time* (sec)	Mass Source Rate** (g/sec)	Aerosol Loss Estimate** %
15-23	3.4 to 3.7	10
23-31	0.72 to 0.79	10
31-46	0.189 to 0.21	10
46-62	0.076 to 0.084	10
62-88	0.056 to 0.062	10
117-145	0.041 to 0.045	10

*Time from initiation of melt teem with source at melt-concrete interaction location

**Range arises from estimates of particle loss during transport from interaction location to sampling point. The loss estimate represents the maximum expected loss employing the method described in the text.

Uncertainty in concentration measurement is about ±38% based on comparison of filter and impactor measurements of concentration. This source term is based on the gas flows given in the text and does not reflect the uncertainty that these high flows may be erroneous or caused by organic material in the crucible. Combined uncertainty in aerosol loss and concentration measurement are ±38%.

The mass source rates are given as a range, the lower being calculated without particle loss and the higher reflecting the estimated particle loss. Based on the above assumptions and treatment, the estimated losses are 10% of the particle mass.

The mass source rates are calculated from the filter samples. An estimate of the uncertainty in the measured concentrations was obtained by comparison of the concentrations measured by the filters and those indicated by impactor samples. The uncertainty in concentration measurement in TURC2 is ±13% and in TURC3 is ±38%. No estimate of the uncertainty in flow measurement has been made. Particle losses during transport to the sampling point are reflected in the range of source term given in the tables and are estimated to be as high as 10% in both tests.

Filter measurements made of the aerosol in the interaction chamber immediately upon portcullis closure give an indication of the mass source rate during the melt teem and initial melt/concrete interaction. Material such as dust, rust from the chamber walls, insulation material, and combustion products from flammable materials could contribute to the measured aerosol mass. The explosive charge used to tap the melt crucible may have caused this material to become airborne. The estimates of the initial source terms are 9 g/sec for TURC2 and 27 g/sec for TURC3. As stated above, these estimates may be high as a result of collection of extraneous material in the filter samples.

Figures 4.26 and 4.27 are graphic representations of the aerosol source terms measured in TURC2 and TURC3, respectively. The range reflected in the histograms is the same as in the tables. Also presented is the molar flow rates of the gas evolved during the interaction.

The figures also include the initial mass source term as indicated by the interaction chamber filter samples. Also contained in Figure 4.27 is a source term calculated using the argon purge gas flow (lower curve). This is to give an idea of the range of uncertainty in the source term. It has not been corrected for delay time or aerosol transport loss.

The possibility of erroneously high gas flows in the TURC3 test must be considered. These results could accurately reflect the gas flows which could have been produced by organic material in the crucible exposed to the high temperature melt. In this case the gas flows and source term measured in the test are actual although not arising only from melt concrete interaction. The chamber concentrations of aerosol were higher in the TURC3 test than in the TURC2 test suggesting a higher source term in the TURC3 test. The chamber derived source term for TURC3 dovetails into the exhaust line source term measurement as seen in Figure 4.27. The presence of organic material in the crucible would also explain the high carbon evolution indicated in the

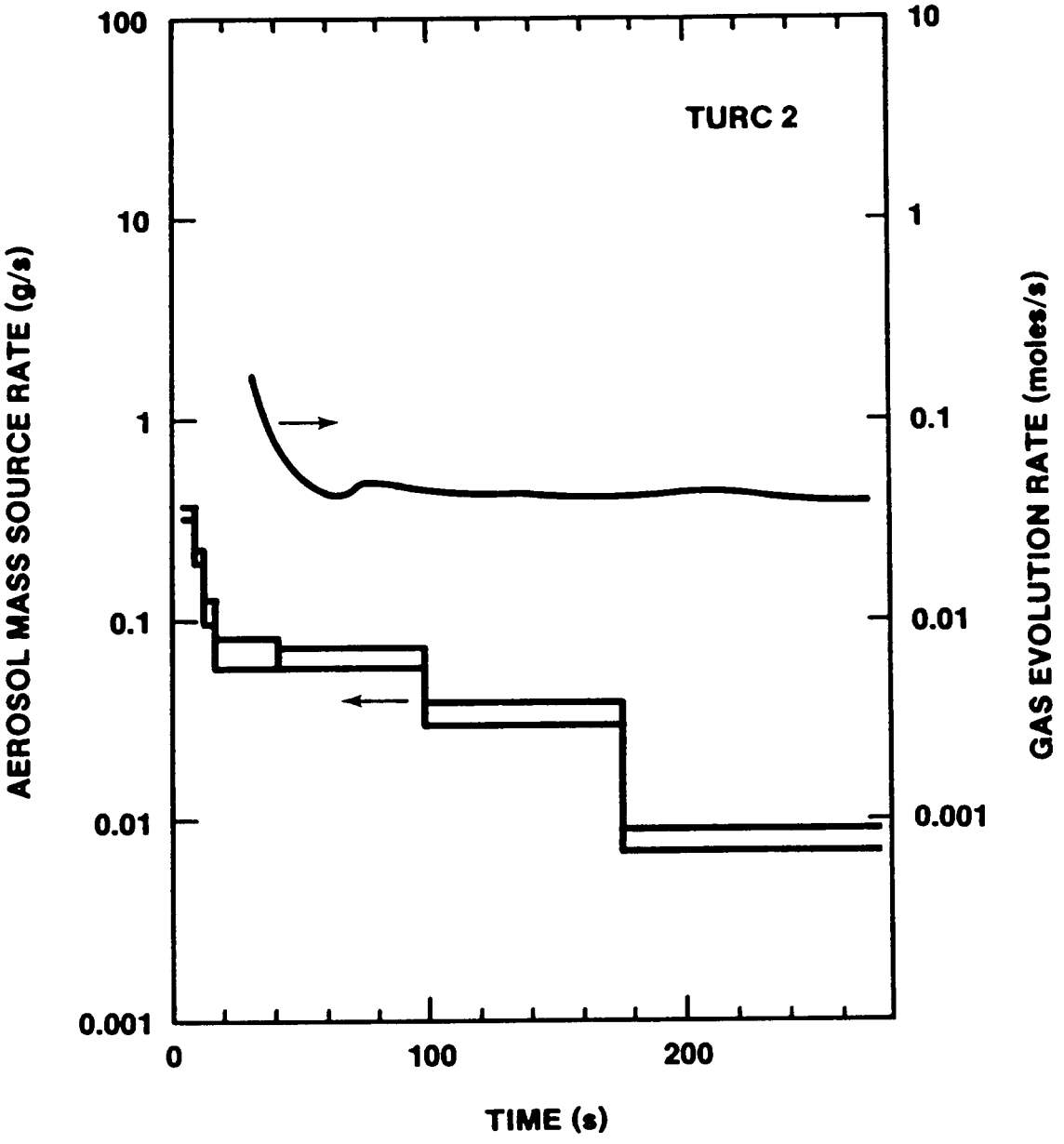

Figure 4.26. Experimental Source Term for TURC2

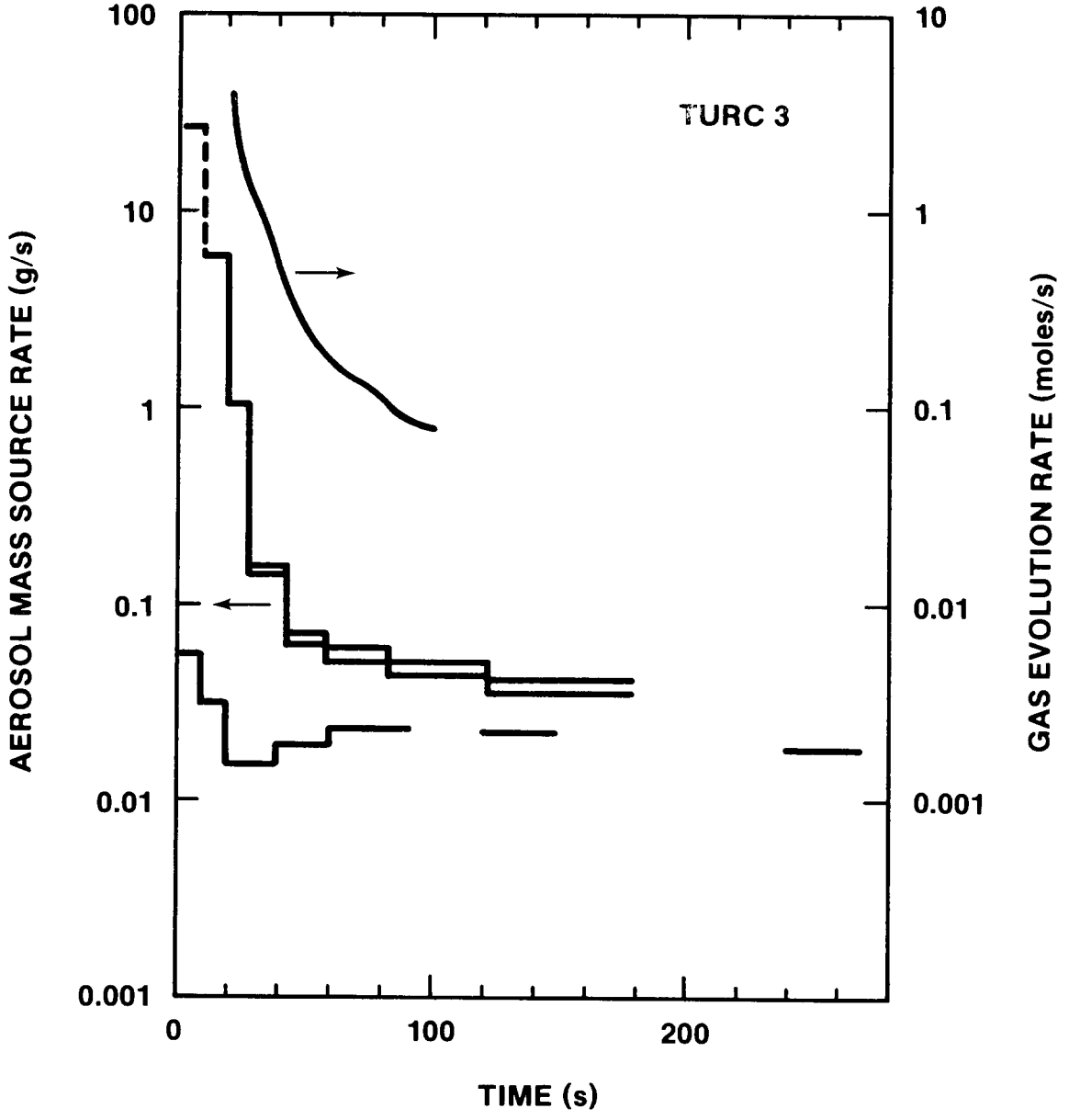

Figure 4.27. Experimental Source Term for TURC3

data. However one must keep in mind the caveats concerning the aerosol measurements made in the chamber.

On the other hand, the gas flow measurements could be in error. This uncertainty exists and is not easily quantified. The lower source term curve in Figure 4.27 is an attempt to show how this uncertainty in gas flow effects the uncertainty in source term. It is calculated using only the 4 g/sec argon purge gas flow as the exhaust flow with the measured exhaust line concentrations. The only concession to delay time is to shift the curve back the 15 seconds from initiation of melt teem to portcullis closure. No aerosol transport losses have been calculated.

The aerosol size distributions have been presented in the data section. The aerosol measured in both tests is characterized by a unimodal distribution with a mass mean aerodynamic diameter of about 1 to 2 μm and a geometric standard deviation of about 2.0.

Table 4.4 gives the mass source rate of release for Mo, Te, and U at two times for TURC2. These are based on the aerosol mass source term calculations and the XRF analysis of filter samples from the test. The ranges given reflect only the particle loss estimates and not measurement uncertainty. The ±14% uncertainty in source measurement is applicable to the results reported in Table 4.4.

Table 4.4

Elemental Mass Source Rate from TURC2

	Elemental Source Rate (mg/sec)	
	A	E
Element	(0 to 5 sec)	(35 to 103 sec)
Mo	6.7 to 7.4	3.3 to 3.7
Te	32 to 35	3.7 to 4.1
U	10 to 11	2.5 to 2.8

Range reflects uncertainty in particle loss during transport.

5. SUMMARY

Two experiments, TURC2, a UO_2/ZrO_2-concrete interaction experiment, and TURC3, a $UO_2/ZrO_2/Zr$-concrete interaction experiment, are reported here.

The TURC2 experiment consisted of 147.2 kg of molten UO_2/ZrO_2 teemed upon limestone common sand concrete. The melt was not internally heated, thus the melt pool cooled naturally. TURC3 was physically similar to TURC2 except the molten debris consisted of 46.45 Kg of $UO_2/ZrO_2/Zr$.

Recorded data for both tests consisted of the thermal response of the crucible, sampling of evolved gases and the collection of aerosol material.

No significant concrete erosion was observed in either experiment (< 5 mm). Experimental data and additional analysis indicates the formation of a stable crust at the melt pool-concrete interface, which in turn inhibited heat transfer to the concrete. Transient heat conduction into the concrete was observed, resulting in the decomposition of the concrete.

Analysis of the gases released from the TURC2 experiment during concrete decomposition suggests CO_2 and H_2O were reduced to CO and H_2, respectively. This is significant in light of the fact the current models within the CORCON code[9,13] do not allow oxidic melts to reduce released gases. The TURC3 gas analysis showed similar evidence of CO_2 and H_2O reduction, with higher molar fractions of CO production than TURC2. These data suggest the importance of the bulk melt pool composition on the production rates of combustible gases.

Both the TURC2 gas composition data and the thermal response of the interaction crucible indicate the released gases from the concrete did not disrupt the melt-concrete interface crust. The data suggests the gases flowed along the melt-concrete interface and up the sidewalls or flowed up through the melt in solidified channels. This observation demonstrates another important role of stable crust formation, namely prohibiting gases to purge a liquid melt pool at its saturation temperature. Therefore a major aerosol production mechanism is impeded and fission production transport by this mechanism from the melt will be decreased.

Aerosol measurements showed aerosol concentrations of 62.1-0.55 g/m^3 for TURC2 and 24.3-3.4 g/m^3 for TURC3. The measure aerosol size distribution for both experiments showed an unimodal

distribution with a mass mean aerodynamic diameter of approximately 1-2 μm. The estimate mass source rate after portcullis closure varied from 0.32 g/sec to 3.8 mg/sec for TURC2 and 5.3 g/sec to 39 mg/sec for TURC3 (based on the reported gas flows). Release rates for Mo, Te, and U were determined for the TURC2 experiment. Mo release was observed to be released at 6.3-3.7 mg/sec, while Te release was 29.8-4.1 mg/sec. U release followed the same trend and magnitude of Mo with release rates of 8.3-2.8 mg/sec. Table 4.3 contains these release figures.

A thermal analysis of the TURC2 and TURC3 experiments has been performed. The results of this analysis suggest the following sequence of events. Upon contact of the melt material with the concrete approximately 1-2 mm of ablation occurred. During this same period rapid crust growth was occurring. The rate of crust growth and boundary layer temperature depression exceeded the rate at which the mixture melt point (UO_2/ZrO_2-concrete) was depressed so that only limited ablation occurred. Thermal resistances were predicted to exist between the solidifying pool and the MgO sidewall in both experiments. A significant thermal resistance from the concrete mid radius outward was predicted to exist in the TURC3 experiment. Thus significant 2-D effects within the concrete slug were present in the TURC3 tests.

REFERENCES

1. USNRC, Reactor Safety Study: An Assessment of Accident Risks in US Commercial Nuclear Power Plants, WASH 1400, NUREG 75/04, October 1975.

2. D. A. Powers and F. E. Arellano, Large-Scale Transient Tests of the Interaction of Molten Steel with Concrete, SAND81-1753, Sandia National Laboratories, Albuquerque, NM, Jan. 1982.

3. D. A. Powers, Sustained Molten Steel/Concrete Interactions Tests, SAND77-1423, Sandia National Laboratories, Albuquerque, NM, June 1978.

4. D. A. Powers, D. A. Dahlgren, J. F. Muir and W. F. Murfin, Exploratory Study of Molten Core Material/Concrete Interaction, July 1975-March 1977, SAND77-2042, Sandia National Laboratories, Albuquerque, NM, Feb. 1978.

5. D. A. Powers and F. E. Arellano, Direct Observation of Melt Behavior During High Temperature Melt/Concrete Interactions, NUREG/CR-2283, SAND81-1754, Sandia National Laboratories, Albuquerque, NM, Jan. 1982.

6. V. K. Dhir, I. Catton, and D. Cho, "Heat Transfer from a Liquid Pool to a Decomposing Solid Surface," Proc. Third PAHR Information Exchange, Argonne National Laboratory, 141 (1977a) ANL-78-10.

7. V. Dhir, I. Catton, and J. Castle, "Role of Taylor Instability on Sublimation of a Horizontal Slab of Dry Ice," ASME Winter Annual Mtg., 76-WA/HT-87 (1976).

8. IDCOR. Technical Report 15.3, Core-Concrete Interactions, Sept. 1983, Atomic Industrial Forum Inc., 7101 Wisconsin Ave., Bethesda, MD 20814.

9. J. E. Gronager, A. J. Suo-Attila, D. R. Bradley, J. E. Brockmann, TURC1: Large Scale Metallic Melt-Concrete Interaction Experiments and Analysis, NUREG/CR-4420, SAND85-0707,Sandia National Laboratories, Albuquerque, NM, 1985.

10. J. F. Muir, R. K. Cole, M. L. Corradini, and M. A. Ellis, CORCON-MOD1 - An Improved Model for Molten Core-Concrete Interactions, NUREG/CR-2145, SAND80-2415, Sandia National Laboratories, Albuquerque, NM, 1981a.

11. R. K. Cole et al., CORCON-MOD2: A Computer Model for Analysis of Molten Core Concrete Interactions, Sandia National Laboratories, Albuquerque, NM, NUREG/CR-3920, SAND84-1246 (1984).

12. Powers, D. A., J. E. Brockmann, and A. W. Shiver, VANESA: A Mechanistic Model of Radionuclide Release and Aerosol Generation During Core Debris Interaction with Concrete, NUREG/CR-4308, SAND85-1370, to be published.

13. E. R. Copus, Development of the Inductive Ring Susceptor Technique for Sustaining Oxide Melts, NUREG/CR-3043, SAND82-2546, Sandia National Laboratories, Albuquerque, NM, 1983.

14. ACI-211. 1-74 Recommended Practices for Normal and Heavy Concrete, American Concrete Institute, Detroit, MI.

15. Beck, J. V., "Criteria for Comparison of Methods of Solution of the Inverse Heat Conduction Problem," Nuclear Engineering and Design 53, North-Holland Publishing Company, 1979.

16. W. W. Tarbell, D. R. Bradley, F. E. Arellano, Sustain Concrete Attack by Low Temperature, Fragmented Core Debris, NUREG/CR-3024SAND82-2476, Sandia National Laboratories, Albuquerque, NM, to be published, Jan. 1984.

17. Siegle,R., Howell, J., Thermal Radiation Heat Transfer, McGraw Hill Book Company, New York, 1981, 2nd Edition.

18. S. M. Lang et al., "High Temperature Reactions of Uranium Dioxide with Various Metal Oxides," NBS-568, February 20, 1956.

19. K. Balberman et al., "The Oxides of Uranium, Part II, The Binary System UO_2-CaO, J. Chem. Soc. 1352-1356, 1951.

20. S. K. Friedlander, Smoke, Dust, and Haze, John Wiley and Sons, Inc., New York, 1977.

21. J. P. Holman, Heat Transfer, McGraw-Hill Book Co., New York, 1972.

22. P. G. Gormley and M. Kennedy, "Diffusion from a Stream Flowing Through a Cylindrical Tube," Proc. Royal Irish Academy, 52-A, pp 163-169, 1949.

23. J. E. Brockmann, "Range of Possible Dynamic and Collision Shape Factors," Appendix F in Uncertainty in Radionuclide Release Under Specific LWR Accident Conditions, R. J. Lipinski, et al, SAND84-0410, Vol II, Sandia National Laboratories, 1985.

24. Y. S. Cheng and C. S. Wang, "Motion of Particles in Bends of Circular Pipes," Atmos. Environ., Vol. 15, pp. 301-306, 1981.

25. B. Y. H. Liu and V. K. Agarwal, "Experimental Observation of Aerosol Deposition in Turbulent Flow," Aerosol Science, 5:145-155, 1974.

DISTRIBUTION:

U. S. Government Printing Office
Receiving Branch (Attn: NRC Stock)
8610 Cherry Lane
Laurel, MD 20707
400 copies for R5, R7

U. S. Nuclear Regulatory Commission (19)
Office of Nuclear Regulatory Research
Washington, DC 20555
Attn: M. Ernst
C. N. Kelber
R. T. Curtis
M. Silberberg
G. Marino
L. Chan
C. Ryder
R. W. Wright
T. Walker
R. O. Meyer
J. Mitchell
S. B. Burson (5)
T. Lee
M. Cunningham
P. Wood

U. S. Nuclear Regulatory Commission (6)
Office of Nuclear Reactor Regulation
Washington, DC 20555
Attn: L. G. Hulman
P. Easky
J. Rosenthal
B. Hardin
Z. Rosztoczy
R. Barrett

U. S. Department of Energy (2)
Albuquerque Operations Office
P. O. Box 5400
Albuquerque, NM 87185
Attn: J. R. Roeder, Director
J. A. Morley, Director
For: C. B. Quinn
R. N. Holton

U. S. Department of Energy
Office of Nuclear Safety Coordination
Washington, DC 20545
Attn: R. W. Barber

Electric Power Research Institute (3)
3412 Hillview Avenue
Palo Alto, CA 94303
Attn: R. Vogel
R. Ritzman
W. Lowonstein

Brookhaven National Laboratory (4)
Upton, NY 11973
Attn: R. A. Bari
T. Pratt
G. Greene
T. Ginsberg

Professor R. Seale
Department of Nuclear Engineering
University of Arizona
Tucson, AZ 85721

Oak Ridge National Laboratory
P. O. Box Y
Oak Ridge, TN 37830
Attn: T. Kress

K. Holtzclaw
General Electric--San Jose
Mail Code 682
175 Kurtner Avenue
San Jose, CA 95125

Argonne National Laboratory (4)
9700 S. Cass Avenue
Argonne, IL 60439
Attn: J. Rest
C. Johnson
L. Baker, Jr.
D. Cho

Cathy Anderson
Nuclear Safety Oversight Commission
1133 15th St., NW
Room 307
Washington, DC 20005

Battelle Columbus Laboratory (3)
505 King Avenue
Columbus, OH 43201
Attn: P. Cybulskis
R. Denning
J. Gieseke

J. E. Antill
Berkeley Nuclear Laboratory
Berkeley GL 139 PB
Gloucestershire
England, U. K.

W. G. Cunliffe
Bldg. 396
British Nuclear Fuels, Ltd.
Springfield Works
Salwick, Preston
Lancashire
England, U. K.

R. Deem
Power Authority State of NY
10 Columbus Circle
New York, NY 10019

Professor Agustin Alonso
E.T.S. Ingenieros Industriales
Jose Gutierrez Abascal, 2
28006 Madrid, Spain

Dr. Alfonso Perez
Departmento de Seguridad Nuclear
Junta de Energia Nuclear
Avenida Complutense, 22
Madrid - 3
Spain

R. Sherry
JAYCOR
P. O. Box 85154
San Diego, CA 92138

Los Alamos National Laboratories
P. O. Box 1663
Los Alamos, NM 87545
Attn: M. Stevenson

UCLA (2)
Nuclear Energy Laboratory
405 Hilgaard Avenue
Los Angeles, CA 90024
Attn: I. Catton
D. Okrent

University of Wisconsin
Nuclear Engineering Department
1500 Johnson Drive
Madison, WI 53706
Attn: M. L. Corradini

EG&G Idaho
Willow Creek Building, W-3
P. O. Box 1625
Idaho Falls, Idaho 83415
Attn: R. Hobbins

Battelle Pacific Northwest Laboratory
P. O. Box 999
Richland, WA 99352
Attn: M. Freshley

Wiktor Frid
Swedish State Power Board
S-162 FACH 87 VALLINGBY
Sweden

W. Stratton
2 Acoma Lane
Los Alamos, NM 87544

Gesellschaft fur Reaktorsicherheit (GRS)
Postfach 101650
Glockengrasse 2
5000 Koeln 1
Federal Republic of Germany

Kraftwerk Union
Hammerbacher Strasse 1214
Postfach 3220
D-8520 Erlangen 2
Federal Republic of Germany
Attn: Dr. M. Peehs

UKAEA
Reactor Development Division (5)
Winfrith, Dorchester
Dorset DT2 8DH
Attn: R. Potter
A. Nichols
B. Bowsher
P. Smith
T. Butland

Nucleare e della Protezione Sanitaria (DISP) (2)
Ente Nazionnle Energie Alternative (ENEA)
Viale Regina Margherita, 125
Casella Postale M. 2358
I-00100 Roma A.D., Italy
Attn: Mr. Manilia
Mr. G. Petrangeli

Dr. K. J. Brinkman
Reactor Centrum Nederland
1755 ZG Petten
THE NETHERLANDS

Dr. S. J. Niemczyk
1545 18th Street, NW
#112
Washington, DC 20036

Kernforschungszentrum Karlsruhe
Postfach 3640
75 Karlsruhe
Federal Republic of Germany
Attn: H. Rininsland

Mr. H. Bairiot, Chief
Department LWR Fuel
Belgonucleaire
Rue de Champde Mars. 25
B-1050 BRUSSELS, BELGIUM

Japan Atomic Energy Research Institute
Tokai-Mura, Naka-Gun
Ibaraki-Ken 319-11
Japan
Attn: S. Saito

Wang Lu
TVA
400 Commerce, W9C157-CK
Knoxville, TN 37902

M. Fontana
Director, IDCOR Program
ENERGEX
575 Oak Ridge Turnpike
Oak Ridge, TN 37830

Fauske and Associates, Inc. (2)
16W070 West 83rd Street
Burr Ridge, Illinois 60521
Attn: R. Henry
M. Plys

Peter Bieniarz
Risk Management Associates
2309 Dietz Farm Road, NW
Albuquerque, NM 87107

Dr. K. Soda
Manager, Chemical Engineering Safety Laboratory
Department of Nuclear Fuel Safety
Japan Atomic Energy Research Institute
Tokai-Muri, Naku-Gun, Ibaraki-Ken
319-11
Japan

K. Sato, Director
Department of Reactor Safety Research
Japan Atomic Energy Research Institute
Tokai-Mura, Naka-Gun, Ibaraki-Ken

P. Fehrenbach
Atomic Energy Canada, Ltd.
Chalk River, Ontario
Canada KOJ IJO

M. Hayns
UKAEA
Safety and Reliability Directorate
Wigshaw Lane
Culcheth
Warrington WA3 4NE
Cheshire
United Kingdom

J. R. Matthews
Aere Harwell
Didcot
Oxfordshire OX11 ORA
United Kingdom

F. Briscoe
UKAEE Culham Laboratory
Abingdon
Oxfordshire OX14 3DB
United Kingdom

H. J. Teague (3)
UKAEA
Safety and Reliability Directorate
Wigshaw Lane
Culcheth
Warrington, WA3 4NE
United Kingdom

M. Jankowski
IAEA
Division of Nuclear Reactor Safety
Wagranerstrasse 5
P. O. Box 100
A/1400 Vienna, Austria

Statens Karnkraftinspektion
L. Hammer
P. O. Box 27106
S-10252 Stockholm, Sweden

Studsvik Energiteknik AB
K. Johansson
S-611 82 Nykoping, Sweden

Atomic Energy Canada Ltd.
M. Notley
Chalk River, Ontario
Canada KOJ 1JO

Atomic Energy Canada Ltd. (2)
Pinawa, Manitoba
Canada ROE 1LO
Attn: H. Rosinger
D. Wren

Korea Adv Energy Research Inst
H. R. Jun
P. O. Box 7
Daeduk-Danji
Choong-Nam, Korea

Institute of Nuclear Energy Research
Sen-I Chang
P. O. Box 3
Lungtan
Taiwan 325, Republic of China

3141 S. A. Landenberger (5)
3151 W. L. Garner (1)
5161 J. Gronager (2)
6400 A. W. Snyder
6410 J. W. Hickman
6412 A. L. Camp
6414 D. M. Ericson, Jr.
6414 A. W. Shiver
6415 J. L. Sprung
6420 J. V. Walker
6421 P. S. Pickard
6422 D. A. Powers
6422 M. D. Allen
6422 R. Blose
6422 J. E. Brockmann (5)
6422 R. M. Elrick
6422 E. R. Copus
6422 W. W. Tarbell (5)
6423 T. R. Schmidt
6425 D. R. Bradley
6425 W. J. Camp
6425 M. Pilch
6425 A. Suo-Anttila (5)
6427 M. Berman
6440 D. A. Dahlgren
6442 W. A. Von Riesemann
6444 R. K. Cole
6444 S. W. Webb
6449 K. D. Bergeron
6449 D. C. Williams
6454 G. L. Cano
7530 T. B. Lane
7537 N. R. Keltner
8024 P. W. Dean

NRC FORM 335 (2-84) NRCM 1102, 3201, 3202

U.S. NUCLEAR REGULATORY COMMISSION

BIBLIOGRAPHIC DATA SHEET

SEE INSTRUCTIONS ON THE REVERSE

1 REPORT NUMBER (Assigned by TIDC, add Vol No., if any)

NUREG/CR-4521
SAND86-0318

2. TITLE AND SUBTITLE

TURC2 and 3: LARGE SCALE UO_2/ZrO_2 MELT-CONCRETE INTERACTION EXPERIMENTS AND ANALYSIS

3 LEAVE BLANK

4 DATE REPORT COMPLETED

MONTH	YEAR
May	1986

5 AUTHOR(S)

J. E. Gronager, A. J. Suo-Anttila, J. E. Brockmann

6 DATE REPORT ISSUED

MONTH	YEAR
June	1986

7. PERFORMING ORGANIZATION NAME AND MAILING ADDRESS (Include Zip Code)

Severe Accident Source Terms Division 6422
Sandia National Laboratories
Albuquerque, NM 87185

8 PROJECT/TASK/WORK UNIT NUMBER

9 FIN OR GRANT NUMBER

FIN No. A1218

10 SPONSORING ORGANIZATION NAME AND MAILING ADDRESS (Include Zip Code)

Containment Systems Branch
Division of Accident Evaluation
U.S. Nuclear Regulatory Commission
Washington, DC 20555

11a TYPE OF REPORT

Topical

b. PERIOD COVERED (Inclusive dates)

12 SUPPLEMENTARY NOTES

13. ABSTRACT (200 words or less)

Two large scale $UO_2/ZrO_2/Zr$ debris-concrete experiments TURC2 and TURC3 are reported here. The experiments consisted of pouring a large quantity of molten $UO_2/ZrO_2/Zr$ mixtures onto limestone-common sand concrete. The molten material was allowed to cool naturally--no internal heating was present. Data for concrete ablation, gas evolution including composition and flow rate, and aerosol generation are presented.

The experimental results indicate very rapid crusting with no detectable concrete ablation. Gas reduction of H_2O and CO_2 to H_2 and CO was found to occur even with a purely oxidic (UO_2/ZrO_2) melt. Aerosol concentrations varied from 62 g/m^3 to less than 1 g/m^3 in the experiments.

A thermal analysis of the experiments was performed. The analysis is consistent with the result that rapid crusting with minimal concrete ablation occurs in both experiments.

14 DOCUMENT ANALYSIS - a KEYWORDS/DESCRIPTORS

Aerosol Generation; Combustible Gas Production; Concrete Ablation; CORCON comparison; Melt-concrete Heat Transfer; Molten Core-concrete interaction.

b IDENTIFIERS/OPEN-ENDED TERMS

15 AVAILABILITY STATEMENT

NTIS
GPO Sales

16 SECURITY CLASSIFICATION

(This page) Unclassified

(This report) Unclassified

17 NUMBER OF PAGES

174

18 PRICE

☆ U.S. GOVERNMENT PRINTING OFFICE: 1986—676-049/41001